Diffuse X-ray scattering study of defect structure in Ni and dilute Ni alloys irradiated with high-energy ions

Hideki Yuya

①

Diffuse X-ray scattering study of defect structure in Ni and dilute Ni alloys irradiated with high-energy ions

Hideki Yuya

Contents

1. Introduction

1. Introduction

1.1 Radiation effects on reactor materials

In the irradiation of metals by particles such as fission (fusion) neutrons, ions and electrons, etc., interactions of incident particles with atoms of the irradiated material lead to reconstruction of the regular atomic ordering in the crystal lattice. These processes are accompanied by the characteristic lattice defects which affect both microstructure and macroscopic (physical, thermal, chemical and mechanical) properties of materials. The unfavorable property changes can have dramatic effects, for example, on the safety and economy of nuclear power reactor.

The principal radiation effects resulting from the interaction of particles with the lattice atoms are electronic ionization and atomic displacement. The atomic displacement can be produced by primary knock-on atoms (PKA) and subsequent cascade collisions. In 1958 Seeger sketched his concept of the many processes that take place in an energetic displacement cascade [1], as shown in Fig 1-1.

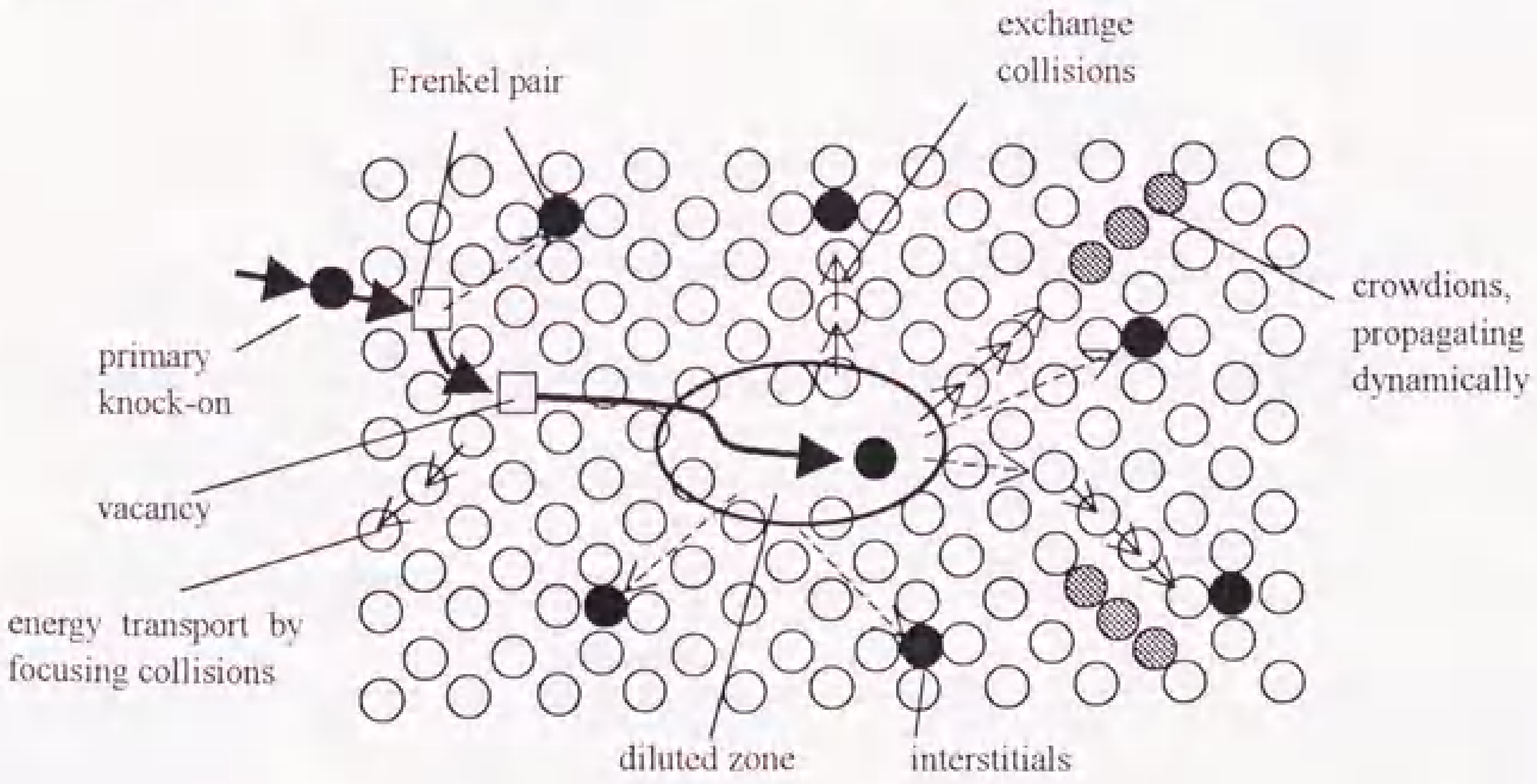

Fig. 1-1 A schematic diagram of a cascade created by a fast neutron (Seeger)

A primary feature of the cascade, first proposed by Brinkman [2], is the formation of a depleted zone, which is caused by the ejection of atoms from the cascade core. A high-energy particle normally loses a large portion of its energy by elastic collisions within a very small region. The region therein, the result of the locally rapid heating (atoms with high vibration energies in the excess of the normal state) and rapid cooling of the displaced atoms forms a thermal spike. If we add to this picture the ideas concerning this thermal spikes, and the calculation of Kinchin and Pease for the number of Frenkel pairs created in a cascade [3], a rather complete picture of displacement processes in irradiated metals would be at hand.

The details, such as precisely how many defects are created, what are their spatial configuration, and do thermal spikes even exist, have been debated for nearly forty years and still without complete resolution. The difficulties in answering these fundamental questions from the experimental side have been the atomic resolution and the time resolution that is needed to capture the dynamics of events which evolve on time scales of some picoseconds [4].

In order to simulate the effects of neutron irradiation on fission and fusion reactor materials, light- and heavy-ion irradiations have been frequently used. The formation process and the structure of defects introduced by the irradiations may differ with the different types of irradiation ions because of the different energy distribution of the PKA. For the meaningful simulation work, it is necessary to clarify the effects of PKA energy spectra on the defect formation in solids. Ion-irradiations are very useful for the research of the PKA energy dependence of the defect formation, since we can get the PKA energy of several hundred eV to about 100 keV by changing the mass and the energy of ions [5].

1.2 Current understanding of atomic displacement processes

To investigate the defect formation processes by ions, many annealing experiments after low temperature irradiation have been performed by electrical resistivity measurement. It was pointed out that the Kinchin-Pease model considerably overestimated the defects formation, although many possibilities were suggested [6]. In recent work the influence of "thermal spike" recombination has been investigated. According to this concept, many "nascent" Frenkel pairs that are created in close-pair configurations recombine as a result of residual agitation in the cascade region and thus decrease the observed defect formation.

Thus, in metals, it had been considered for a long time that atomic displacement and radiation annealing (defect annihilation during irradiation) could be caused only by elastic interaction. However, it was found by electrical resistivity measurement that the energy transferred from electron-excitations to lattice atoms caused the radiation annealing [7-9]. Typical examples of recovery curves $\Delta\rho/\Delta\rho_0$ and the temperature derivatives of the recovery curves $-d(\Delta\rho/\Delta\rho_0)/dT$ as functions of the annealing temperature T in the low-temperature region are shown in Fig.1-2 (a) and (b), respectively. The reduction of stage I recovery is seen for high-energy heavy-ion irradiation. As a parameter that characterizes a PKA energy spectrum, they employed the PKA median energy $T_{1/2}$. The PKA median energy means that half of the displaced atoms result from PKA's with energies higher than $T_{1/2}$. The amounts of the stage I recovery in Ni are plotted in Fig.1-3 as a function of $T_{1/2}$. As can be seen in this figure, for the low-energy ion-irradiation, the amount of the stage I recovery changes systematically with increasing PKA median energy. For high-energy ion-irradiation, the behavior of the stage I recovery is greatly different from that for the low-energy ion-irradiations. For I-ion irradiation, the stage I peak nearly completely disappears, and moreover, even the recovery peak around 100K disappears. Thus, the anomalous reduction of the stage I recovery for high-energy ion-irradiations is not related to the PKA median energy, and it can not be explained within the framework of the defect formation and the radiation annealing by the nuclear collisions. For high-energy heavy ions cause high-density electron excitations along their ion paths in solids. The amount of electron excitations is given by the electronic stopping power, i.e., the energy transferred from ions to electrons in the specimen per unit length of the ion path. In order to study the effect of the high-density electron excitations on the stage I recovery, they plotted the amount of the stage I recovery in Ni as a function of the electronic stopping power (Fig.1-4). This figure shows that the amount of the stage I recovery in Ni is strongly related to the electronic stopping power. However, the radiation annealing model is, in certain respects, oversimplified. In particular, the possibility of interstitial clustering, either during the thermal spike or isochronal annealing, is neglected.

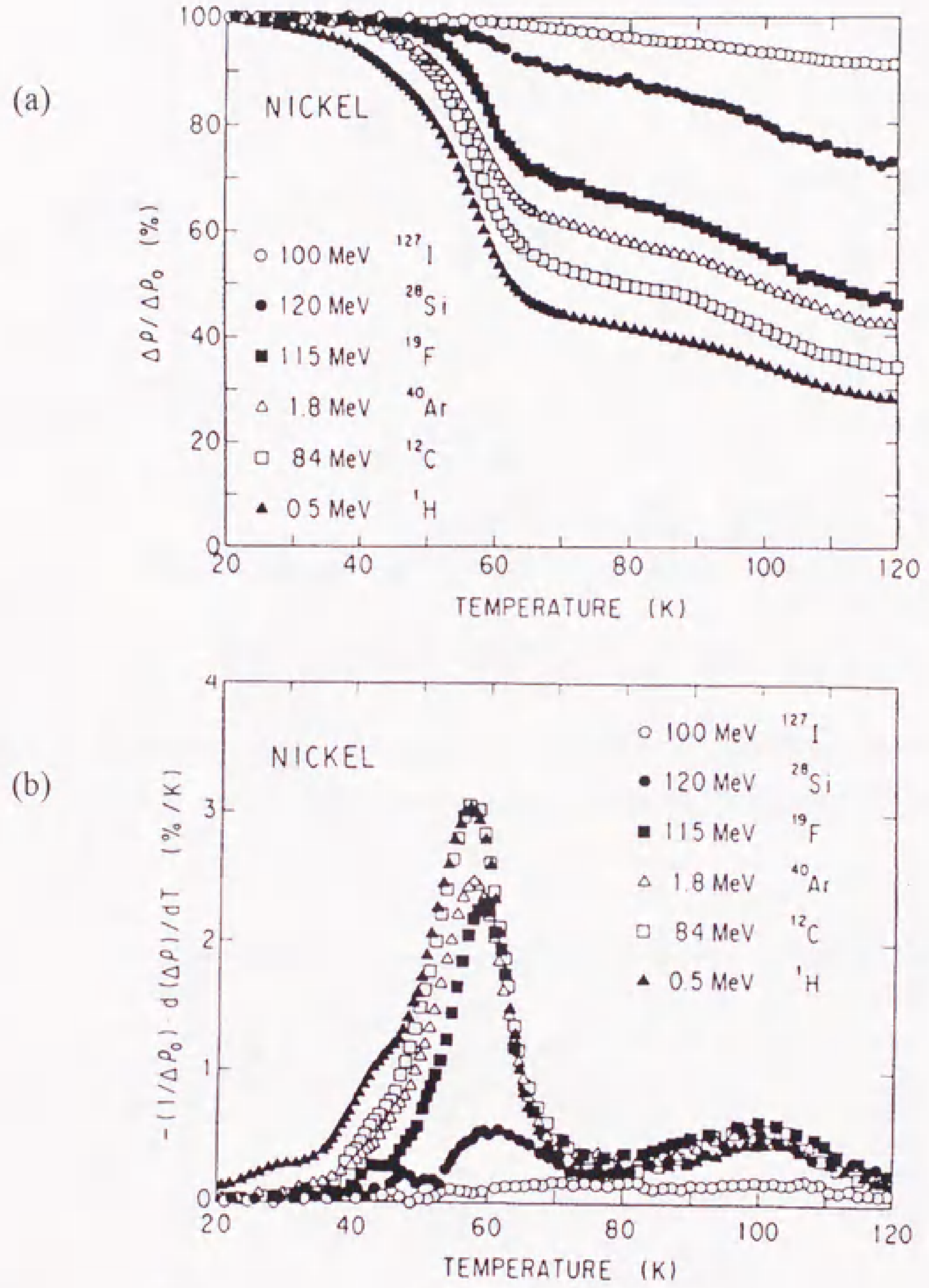

Fig.1-2 recovery curves (a) and temperature derivatives of recovery curves (b) in Ni as a function of annealing temperature.

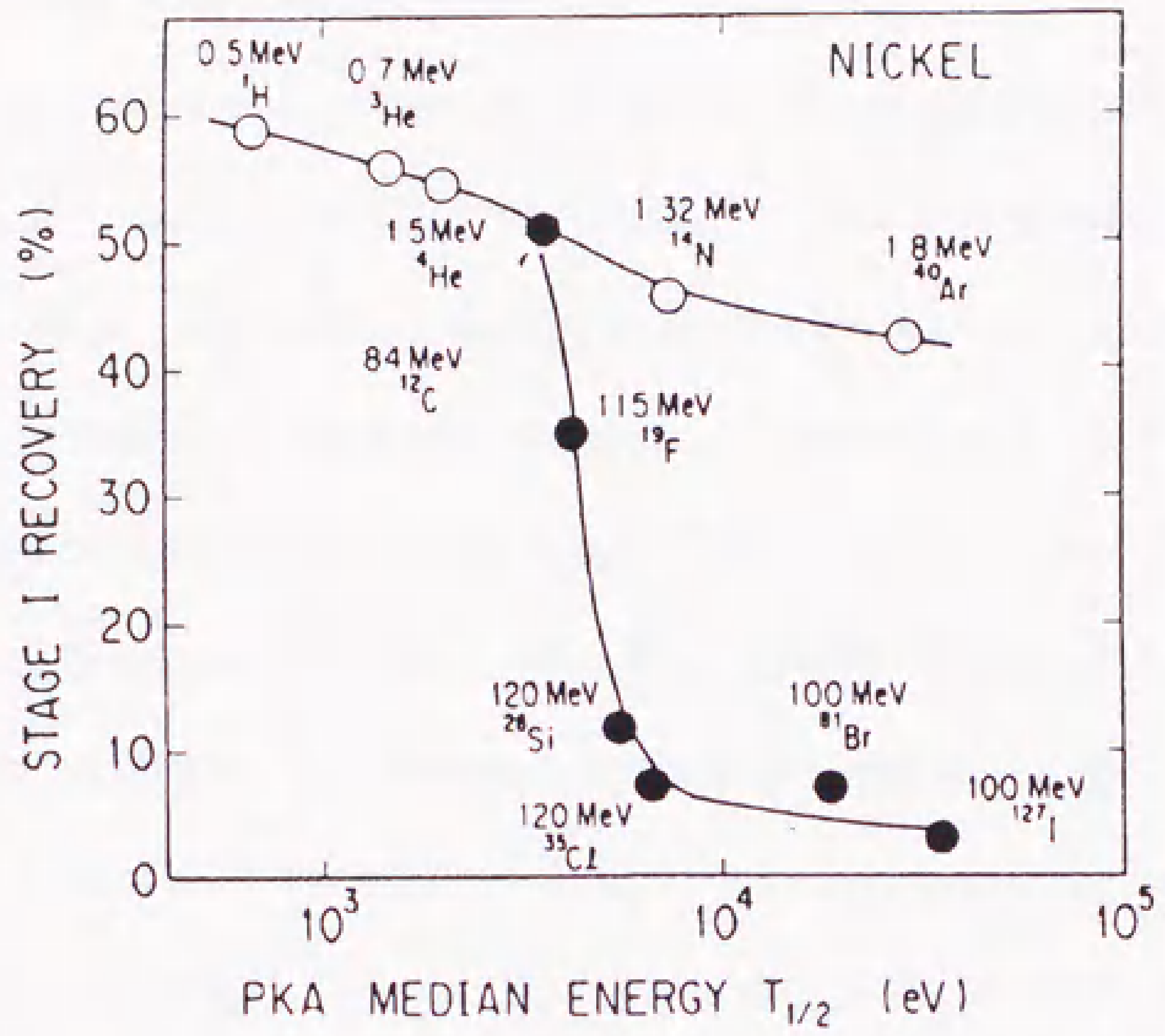

Fig. 1-3 Amount of stage I recovery in Ni for low-energy ion irradiations (open circles) and for high-energy ion irradiations (solid circle) as a function of $T_{1/2}$.

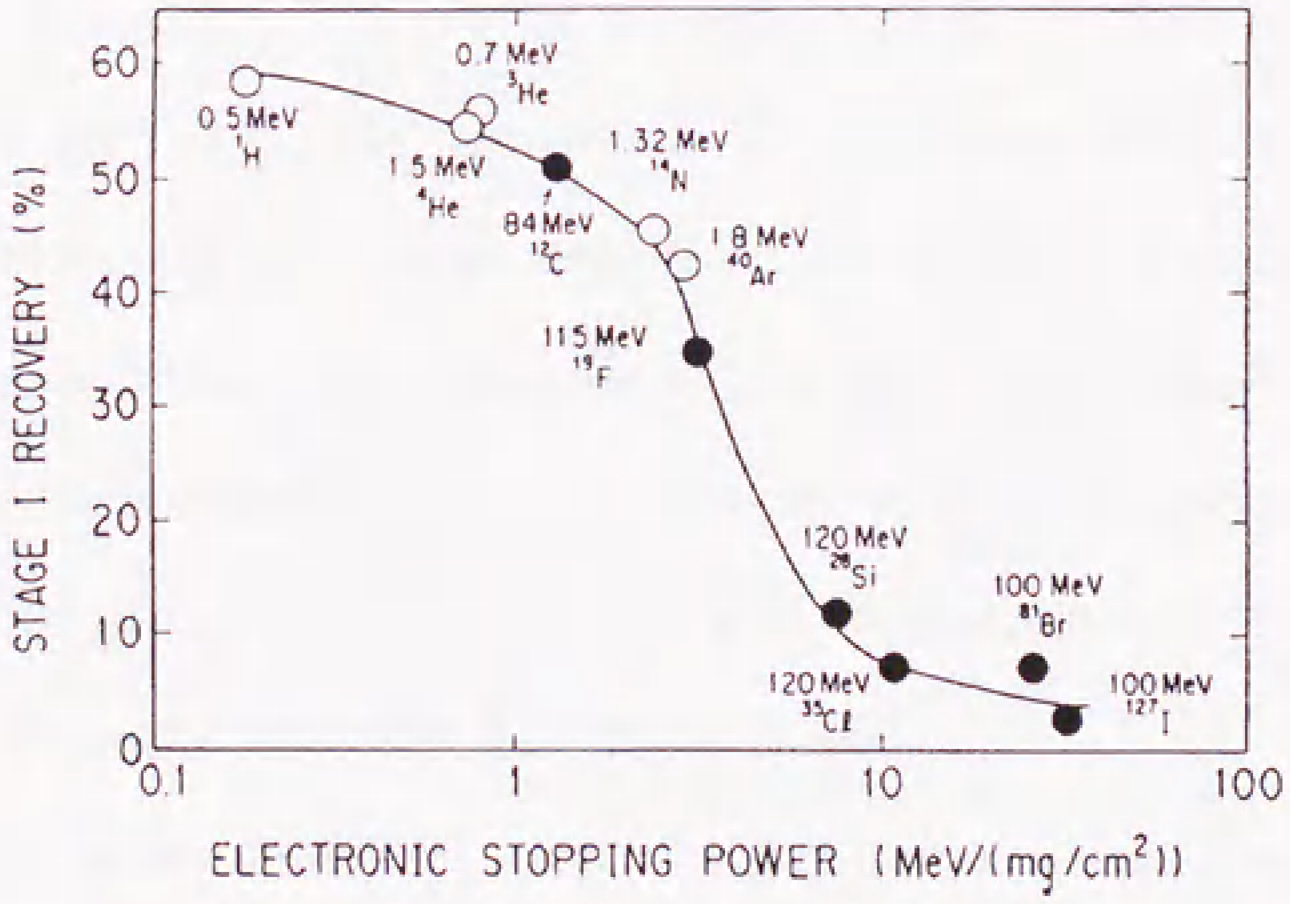

Fig. 1-4 Amount of stage I recovery in Ni for low-energy ion irradiation (open circle) and for high-energy ion irradiations (solid circles) as a function of electronic stopping power.

1.3 Diffuse X-ray scattering methods

For many irradiation conditions, the primary irradiation defects (i.e., vacancies and interstitials) condense into dislocation loops. The number density and the detailed structure of these loops are of fundamental interest for the understanding of the mechanical behavior of irradiated materials. Transmission Electron Microscope (TEM), Positron Annihilation Spectroscopy (PAS), change of electrical resistivity and Diffuse X-ray Scattering (DXS) have been mainly employed to investigate the structure of these loops. It is important to make progress in elucidating the irradiation effects by collecting characteristic knowledge obtained with each method.

Diffuse scattering of X-ray has been successfully used for the detailed investigation of smaller-sized defects [10-24] and can be used as a method to obtain average defect parameters for a distribution of larger-sized defects as well. Considerable progress has been achieved in this area during the last 20 years as discussed in a review [25]. At present, the experimental techniques are rather well developed, and with the added availability of synchrotron radiation for diffuse-scattering measurements, very detailed measurements will be made possible.

For example, diffuse X-ray scattering of pure Ni and dilute Ni alloys at several steps of an isochronal annealing after electron-irradiation at low temperature have been reported [26-30]. The experimental result for pure Ni irradiated with electrons at low temperature was reported by Bender et al. [26] as follows :

Figure 1-5 shows the typical result of X-ray scattering measurements for the samples irradiated to the highest and lowest doses ($\mathrm{Ni}_{\mathrm{IV}}$ and $\mathrm{Ni}_{\mathrm{III}}$). Figure 1-6 shows characteristic feature of the diffuse-scattering behavior during annealing at stage II. Intensity is plotted as a function of q/h on a double logarithmic scale for the sample with lowest and highest irradiation doses. At higher annealing temperatures the diffuse scattering intensity becomes larger for small values of q, and it decreases more steeply than q^{-2} for larger q values, showing the typical formation of interstitial clusters. Finally at 300K the intensity drops off as q^{-4} at larger distance from the Bragg peak, indicating the formation of large interstitial clusters.

Figure 1-7 reviews the annealing results in more detail. The resistivity annealing curve of Ni $_{\mathrm{IV}}$ is also included. The diffuse scattering intensities after annealing are normalized to those measured at 6K. The effective number of interstitials per a cluster, N, can be known from DXS intensity and resistivity. As shown in this figure, interstitials produced at low temperature irradiation begin to form clusters at > 60K. A strong increase of N is observed between 200K and 300K.

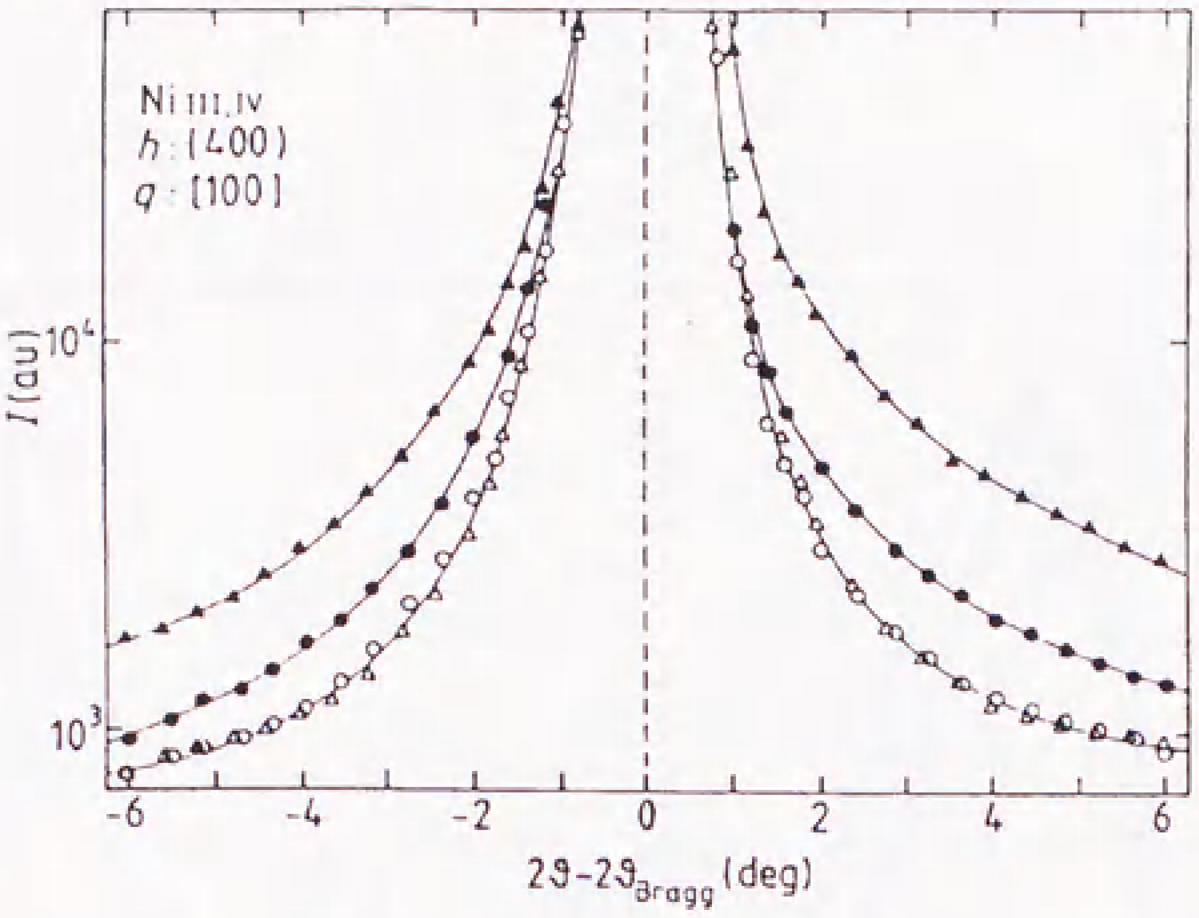

Fig.1-5 Diffuse scattering intensity measured at (400) reflections in the [100]q direction of $\mathrm{Ni}_{\mathrm{III}}$ (○and●) and $\mathrm{Ni}_{\mathrm{IV}}$ (△and▲) (open symbols show the background intensity, full symbols the measurements after irradiation)

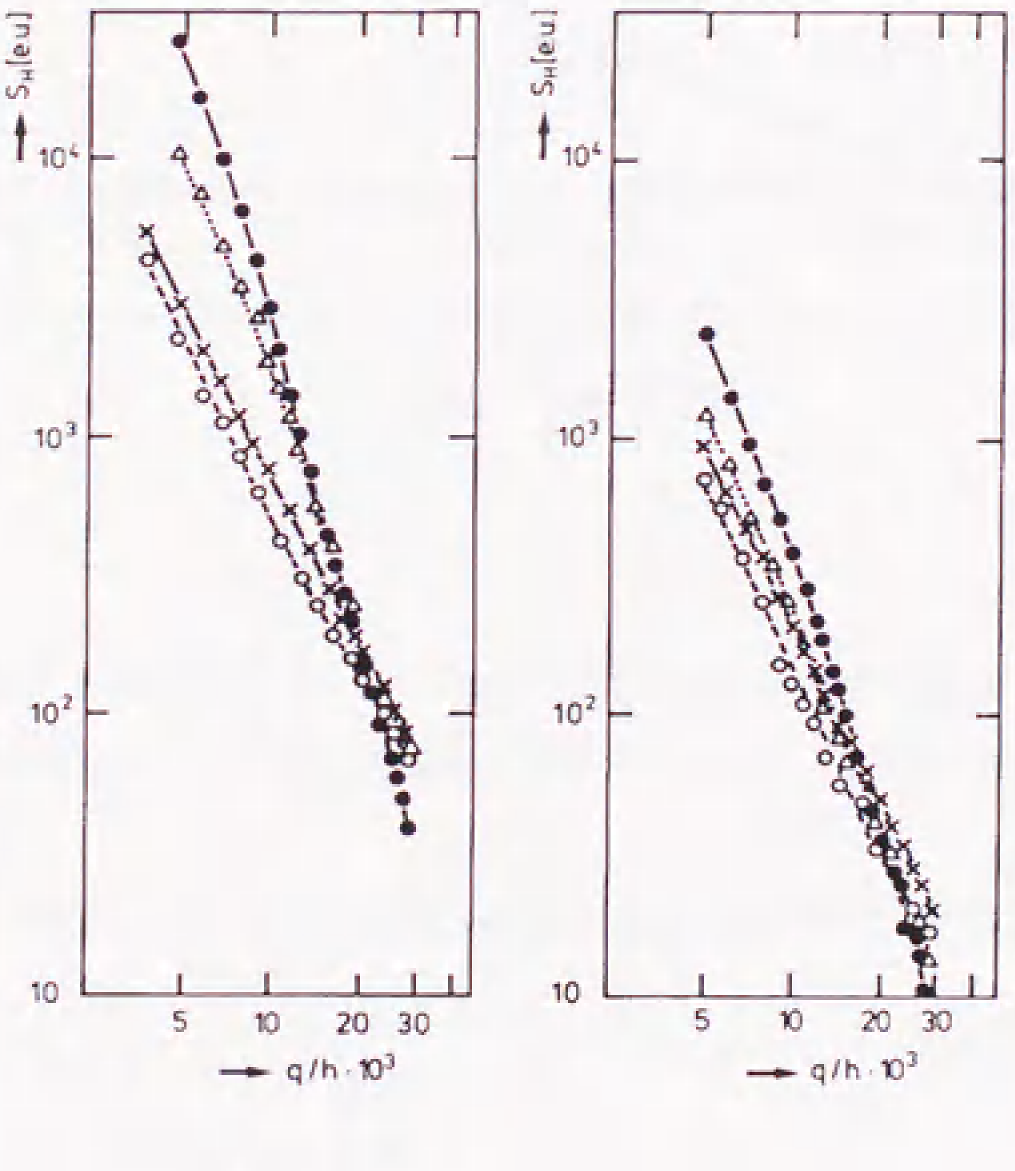

Fig.1-6 Annealing of the diffuse scattering intensity of sample Ni $_{\mathrm{III}}$ and sample Ni $_{\mathrm{IV}}$. Annealing temperature : × 6K, ○ 50K, ■ 85K, △ 200K, ● 300K.

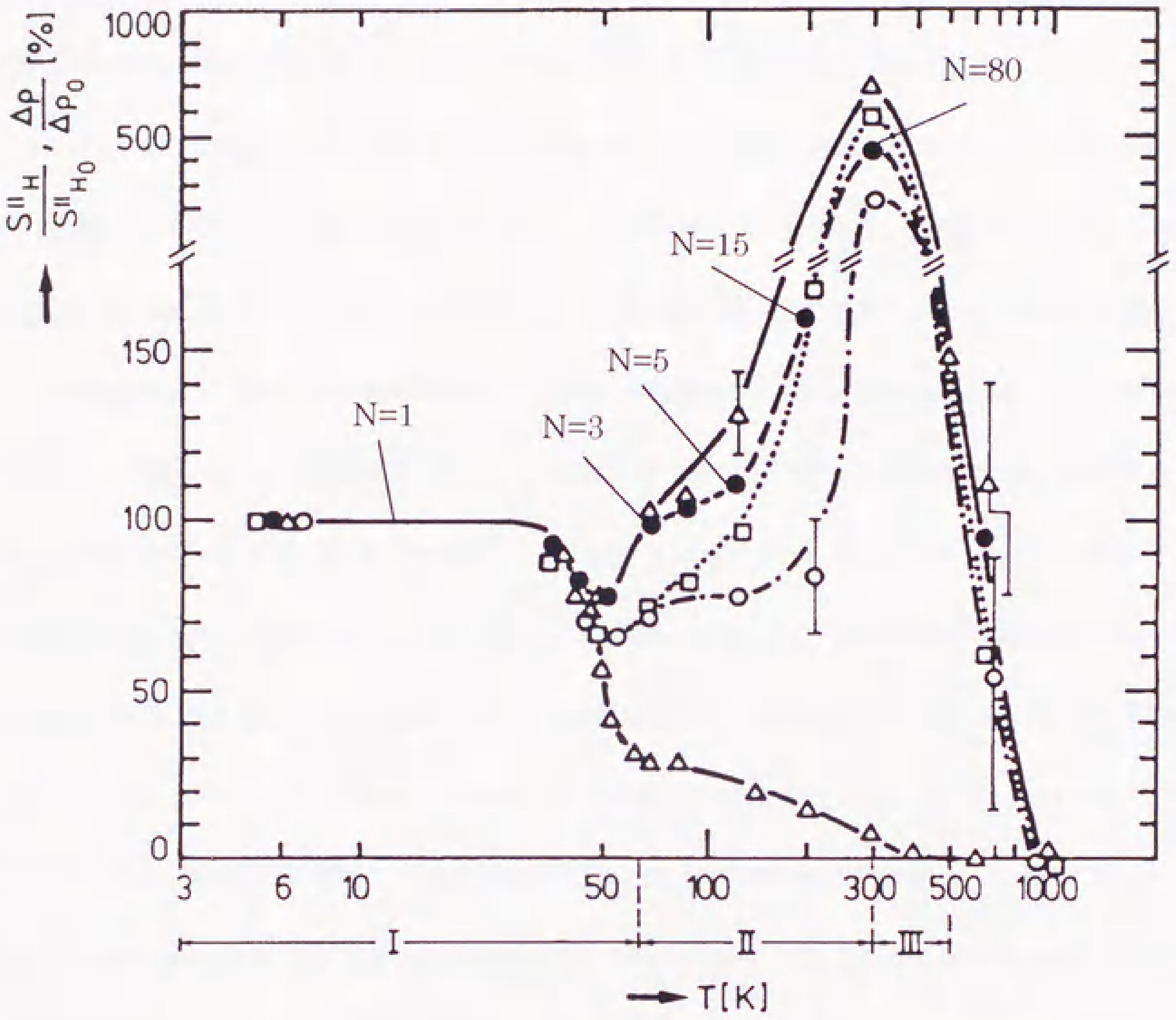

Fig.1-7 Thermal annealing of the Huang diffuse scattering intensity from measurements at (400) reflections in the [100] direction of *q*.

Samples ;

● : Ni I (Interstitial concentration = 261 ppm)

□ : Ni II (268 ppm)

○ : Ni III (179 ppm)

△ : Ni IV (522 ppm)

1.4 Purpose of this study

In nuclear engineering, the elucidation of defect formation mechanism and the utilization of ion-irradiation for this purpose are the important subjects to evaluate the life time of structural materials in nuclear power plants quantitatively.

It is the aim of this study to investigate the defect structures in pure Ni and dilute Ni alloys irradiated with high-energy (～100MeV) ions. The obtained results is thought to enable one to investigate the annihilation of stage I in Ni under high-energy ion-irradiation. Pure Ni and dilute alloys irradiated with phosphorus and iodine ions were investigated by diffuse X-ray scattering method in an attempt to obtain a better understanding of this phenomena. It was considered that the statistically reliable information on number, size and nature of vacancy- or interstitial-loops were needed. Therefore, in this study, the defect structure was investigated by diffuse X-ray scattering (DXS) methods. For this purpose, it become necessary at first to make a computer program to calculate the theoretical diffuse-scattering intensity since there is no appropriate program for our experimental conditions that seems to be able to evaluate the number of dislocation loops precisely.

References

[1] A. Seeger, *Proc. 2nd UN Int. Conf. on Peaceful Uses of Atomic Energy, Geneva,* **6**(1958)250.

[2] J. A. Brinkman, *J. Appl. Phys.* **25**(1954)961.

[3] G. H. Kinchin and R. S. Pease, *Rep. Prog. Phys.* **18**(1955)200.

[4] R. S. Averback, *J. Nucl. Mater.* **216**(1994)49.

[5] R.S. Averback, R. Benedek and K. L. Merkle, *Phys. Rev.* B**18**(1978)4156.

[6] R. S. Averback, R. Benedek and K. L. Merkle, *J. Nucl. Mater.* **75**(1978)162.

[7] A. Iwase, S. Sasaki and T. Iwata, *Phys. Rev. Lett.* **58**(1987)2450.

[8] A. Iwase and T. Iwata, *Nucl. Instr. and Moethds in Phys. Res.* B**90**(1994)322.

[9] A. Iwase, T. Iwata, T. Nihira and S. Sasaki, *Rad. Eff. And Deffects in Solids* **124**(1992)117.

[10] H. Ekstein, *Phys. Rev.* **68**(1945)12.

[11] K. Huang, *Proc. R. Soc.* A **190**(1947)102.

[12] W. Cochran and G. Kartha, *Acta Crystallogr.* **9**(1954)941.

[13] M. A. Krivoglaz, *Theory of X-ray and Thermal Neutron Scattering by Real crystals* (Plenum Press, New York, 1969).

[14] P. H. Dederichs, *Phys. Rev.* B**4**(1971)1041.

[15] H. Trinkaus, *Phys. Status solidi* (b) **5**(1972)307.

[16] P. Ehrhart, *Report of the Kernforschungsanlage, Julich, Germany, Report No. Jul-810-FF, 1971*

[17] P. Ehrhart and W. Shilling, *Phys. Rev.* B**8**(1973)2604.

[18] B. C. Larson and W. Schmatz, *Phys. Rev.* B**10**(1973)2307.

[19] P. H. Dederichs, *J. Phys.* F**2**(1973)471.

[20] A. R. Stokes and A. J. C. Wilson, *Proc. Phys. Soc.* **56**(1944)174.

[21] H. G. Houbold, *J. Appl. Cryst.* **8**(1975)175.

[22] H. G. Houbold, *Revue de Physique Appliquee* **11**(1976)73.

[23] P. Ehrhart and U. Shlagheck, *J. Phys. F : Met. Phys.* **4**(1974)1575, 1589.

[24] P. Ehrhart, *J. Nucl. Mater.* **69/70**(1978)200.

[25] P. Ehrhart, *J. Nucl. Mater.* **216**(1994)170.

[26] O. Bender and P. Ehrhart, *J. Phys. F : Met. Phys.* **13**(1983)911.

[27] E. Segura and P. Ehrhart, *Radiat. Eff.* **42**(1979)233.

[28] R. S. Averback and P. Ehrhart, *J. Phys. F : Met. Phys.* **14**(1984)1347.

[29] P. Ehrhart and R. S. Abverback, *J. Phys. F : Met. Phys.* **14**(1984)1365.

[30] P. Ehrhart and R. S. Averback, *Phil. Mag.* A**60**(1989)283.

2. Theory

2.1 Introduction

Scattering experiments with radiation of a wavelength similar to the atomic distance of ~1Å are the appropriate tools for the investigation of the microscopic structure of defects in crystalline solids. Quite different types of radiation like X-rays, thermal neutrons or electrons have been used for such structural analysis. In contrast to the case of the direct imaging, X-rays have advantages in evaluation of the details of the diffraction pattern. The defect induced changes in a diffraction pattern are schematically shown in Fig.2-1. Compared to the "perfect crystal" , we observe essentially three changes: (a) a shift of the position of the Bragg peaks corresponding to the average change of the lattice parameter. (b) An attenuation of the intensity of the Bragg peaks which can be quantitatively described by a "static Debye-Waller Factor". This value yields the average number of atoms that are no longer contributing to the Bragg scattering due to the defect induced displacements of the lattice atoms. (c) A diffuse X-ray scattering (DXS) background, that reflects the no longer perfectly destructive interferences, is observed between Bragg peaks. The distribution of this diffuse scattering intensity contains very detailed information on the defects. The X-ray method reach the sensitivity the small diffuse intensity of typically 10-100 ppm of atomic size defects [1]. Therefore, the determination of the structural properties of self-interstitial atoms (SIA) and vacancies (V) has become a unique field of application for the X-ray diffraction technique (XRD). The additional characteristic feature of the DXS is the increase of the scattering intensity when defects form clusters. Therefore clustering can be very sensitively detected.

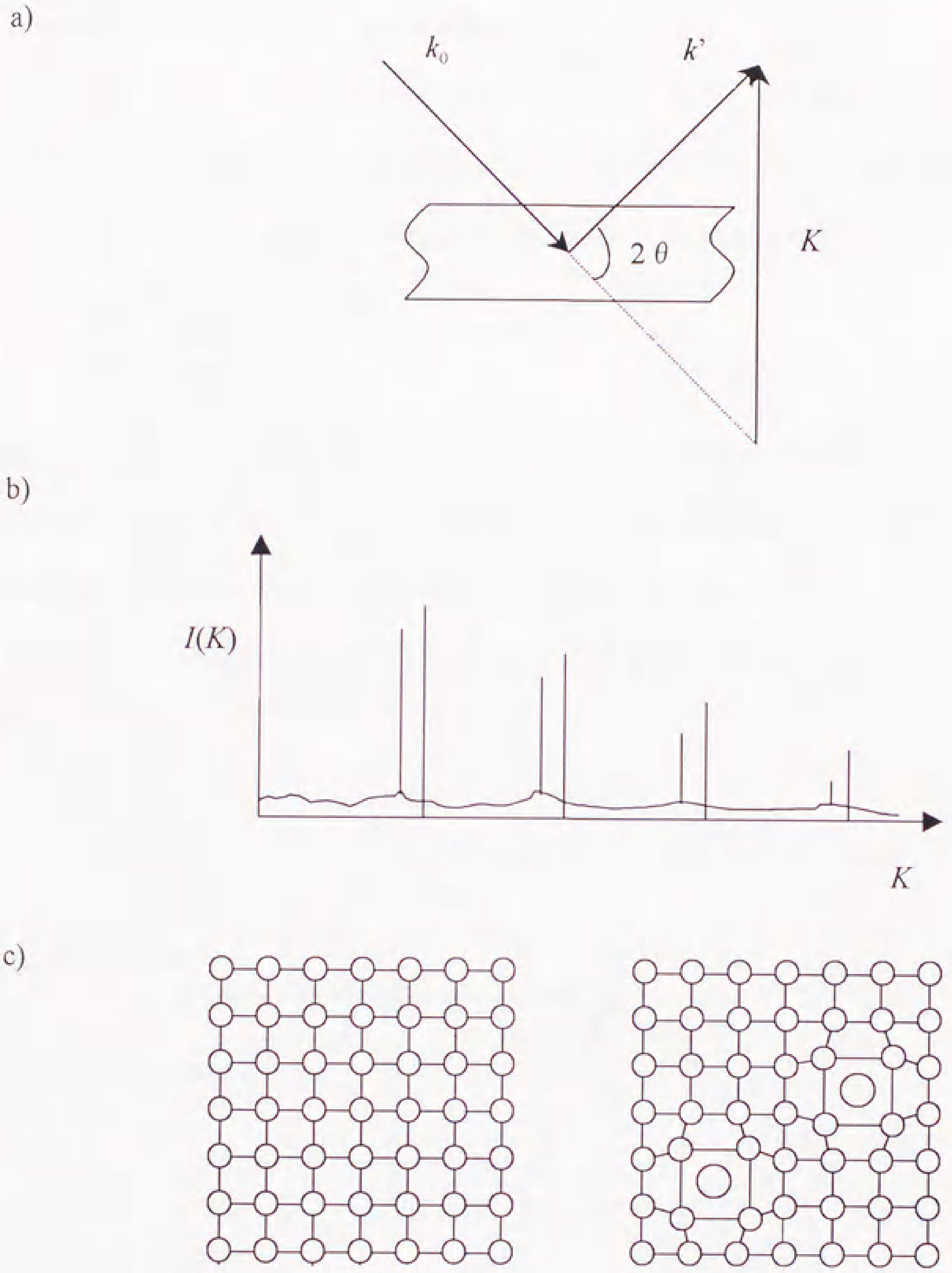

Fig. 2-1 Schematic of the scattering experiment and of the change of the diffraction pattern due to points defects : (a) Scattering triangle (b) Diffraction pattern of "ideal" crystal and of the distorted crystal. (c) Arrangement of atoms in a perfect crystal and in a crystal containing point defects with distortion field

2.2 Interaction of X-rays with matter

The elastic scattering cross section, which is the process of interest, can be quantitatively understood by a classical calculation of the induced dipole radiation of the electrons, which yields the Thomson scattering cross section :

$$\frac{d\sigma}{d\Omega_{Th}} = \left|\frac{e^2}{mc^2}\right|^2 \frac{1+\cos^2 2\vartheta}{2} \quad . \tag{2-1}$$

If there are several scattering centers, there is a phase shift between the different scattered waves that has to be considered in the calculation of the total scattering amplitudes. This phase factor can be understood from Fig.2-2 which shows the scattering of an incoming wave characterized by a wave vector k_0 and a scattered wave k'.

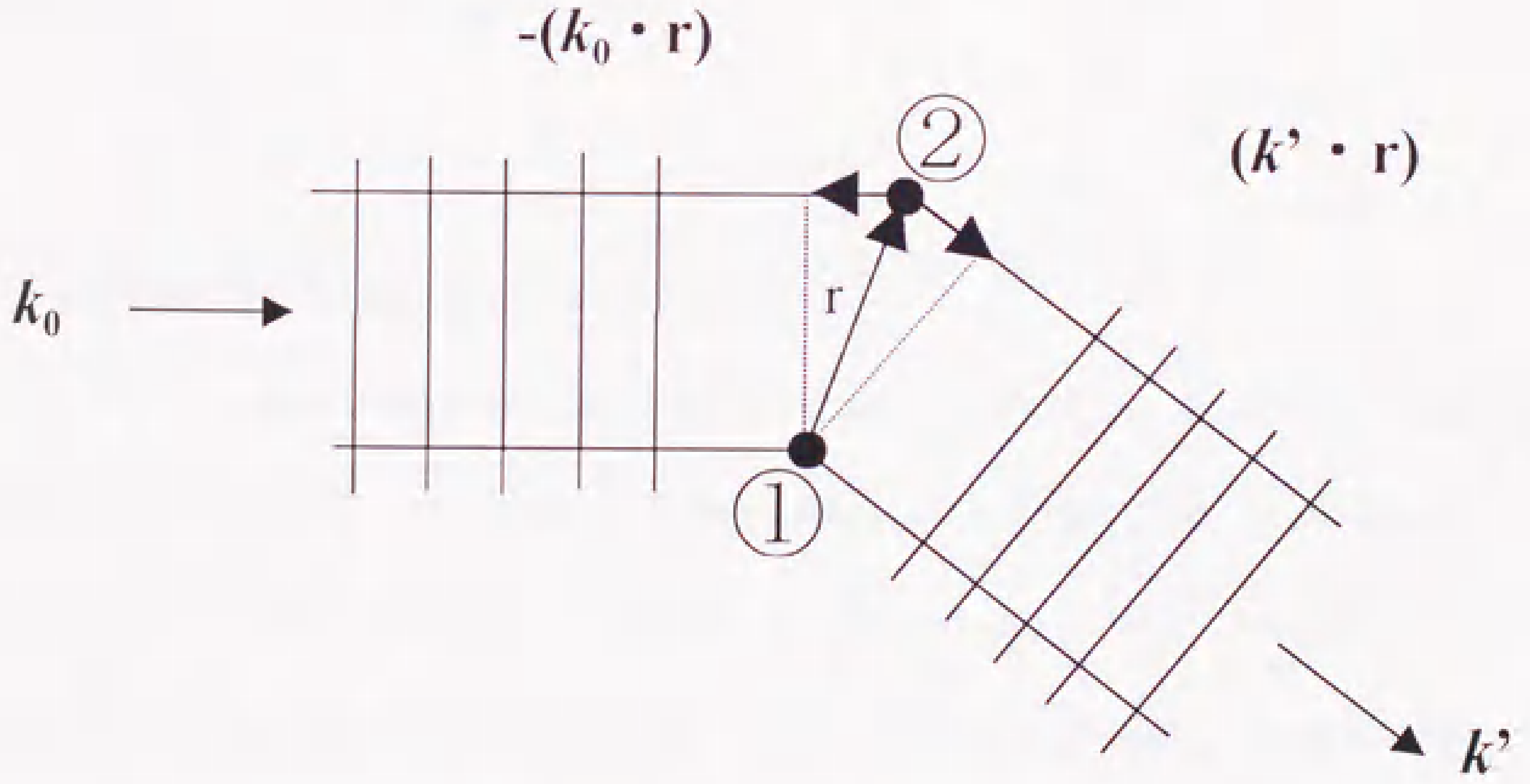

Fig.2-2 Schematic illustration of the phase difference of the scattered waves from two scattering centers.

The atomic scattering cross section is

$$\frac{d\sigma}{d\Omega_{Th}} = |f(K)|^2 \left.\frac{d\sigma}{d\Omega}\right|_{Th} , \tag{2-2}$$

where *f(K)* is the so called atomic factor ;

$$f(K) = \int \rho(r) e^{iK\cdot r} d^3 r , \tag{2-3}$$

i.e. the Fourier transform of the electron density distribution.

In the following I will discuss the scattering function *S*(*K*), i.e. the scattering cross section per atom that is given in units of the Thomson cross section :

$$S(K) = \frac{1}{N}\left|\sum_{n=1}^{N} f_n e^{iK\cdot r_n}\right|^2 . \tag{2-4}$$

This scattering amplitude depends only on the scattering vector $K=k'-k_0$. From this basic formula we can directly deduce the Bragg scattering : we expect a maximum intensity when all scattering contributions are in phase or $K\ r_n = 2\pi$. This means that the atoms can be considered as arranged on planes of separation *d* or

$$n\lambda = 2d\sin\vartheta . \tag{2-5}$$

2.3 Theoretical background of the DXS

For a quantitative description of the distribution of the scattering intensity from a crystal that contains point defects, I start with the basic Eq.(2-4), that presents a Fourier transform of the atomic arrangement in the crystal. This atomic arrangement is superposition of the local distribution of the defects and their individual displacement fields. Krivoglaz [2] has shown that these contribution can quite generally be factorized and that the diffuse scattering cross section *S* from the point defects (single defects or clusters) can be expressed as the product of the square of the Fourier transform of the concentration fluctuation of the defects, $\tilde{c}(q)$, and the square of the scattering amplitude, $A(K)$, due to one defect

$$S(K) = \left\langle \left|\tilde{c}(q)\right|^2 \right\rangle \left|A(K)\right|^2 , \tag{2-6}$$

where K is the scattering vector and q the distance of K from the nearest reciprocal lattice vector G. For a random distribution of defects, $\left\langle \left|c(q)\right|^2 \right\rangle$ is given by $c(1\text{-}c)$ which can be approximated by c for $c<<1$ (c is the concentration). Consequently the scattering pattern is determined by the scattering due to one defect $S(K) = c\left|A(K)\right|^2$. Within this so-called single defect approximation the theory of the diffuse scattering from defects is well developed [3-5].

The scattering amplitude of the individual defect is given by a coherent superposition of the scattering amplitudes resulting from the defect atoms and the displaced lattice atoms in their neighborhood. Accordingly the diffuse-scattering intensity arising from defects can be written as

$$S(K) = c\left| f_D + \sum_m f_m e^{iK\cdot r_m} (e^{iK\cdot s_m} - 1) \right|^2 , \tag{2-7}$$

where f_D represents the scattering amplitude from additional or missing atoms which define the lattice defects ("Laue scattering"). The sum in Eq.(2-7) describes the diffuse scattering amplitude (total amplitude minus the Bragg reflection amplitude) from the lattice atoms m displaced from their ideal position r_m by s_m due to the presence of the defects ("distortion scattering").

2.3.1 Point defects (Huang Diffuse Scattering)

For cubic crystals the relaxation volume of the defects as well as the measured change of the lattice parameter, $\Delta a / a$, are directly related to the trace of P_{ij} (dipole force tensor [6]),

$$V^{rel} = TrP/(C_{11} + 2C_{12}) \quad (2\text{-}8)$$

$$\frac{\Delta a}{a} = \frac{1}{3}\frac{\Delta V}{V} = \frac{c}{3}\frac{V^{rel}}{\Omega} = \frac{c}{3\Omega}\frac{TrP}{(C_{11} + 2C_{12})} \;. \quad (2\text{-}9)$$

C_{ij} are elastic constants and Ω is the atomic volume. The long range displacement field can generally be described by

$$s(r) = \frac{1}{r^2} fct.(C_{ij}, r, P_{ij}) \;, \quad (2\text{-}10)$$

where $fct.(C_{ij}, r, P_{ij})$ is an angular dependent function. The characteristic decrease proportional to r^{-2} yields a q^{-1} behavior of the Fourier transform :

$$s(q) = \frac{1}{q} fct.(C_{ij}, q, P_{ij}) \quad (2\text{-}11)$$

Using this expressions one can look on the scattering cross section S in more detail. In principle one can numerically calculate the exact scattering starting from the basic Eq.(2-7). As the displacements are very small at larger distances the exponential in Eq.(2-7) can be expanded and one obtain

$$S(K) = c\left| f_D + \sum_{n=1}^{N} f_n e^{iK\cdot r_n}(e^{iK\cdot s_n} - 1 - i\cdot K\cdot s_n) + i\cdot f\cdot K\cdot s(q)\right|^2 \;, \quad (2\text{-}12)$$

Due to the q^{-1} behavior of $s(q)$ the term $Ks(q)$ is dominating close to the Bragg reflection and as the values of the Fourier transform at small q image the displacements at larger distance this scattering intensity images the long range part of the displacement field. Considering in addition only the leading term remaining after further approximations for the contributions to the sum in Eq.(2-12), this equation yield

$$S(K) = c\left| f_D - f(L/c) + i\cdot f\cdot K\cdot s(q)\right|^2 \;, \quad (2\text{-}13)$$

with

$$L/c = \sum_{n=1}^{N}(1 - \cos Ks_n) \;.$$

The most characteristic features of the Huang Diffuse Scattering can be demonstrated for the simplest case of an isotropic displacement field in an isotropic crystal :

$$s(r) = C\frac{r}{r^3} = \frac{V^{rel}}{4\pi\gamma}\frac{r}{r^3}\ , \tag{2-14}$$

$$s(q) = i\frac{V^{rel}}{\gamma\Omega}\frac{q}{q^2}\ .$$

Inserting this results yields :

$$S(K) = c\left| f_D - f(L/c) - f\frac{V^{rel}}{\gamma\Omega}\frac{K}{q}(K \cdot q)\right|^2 . \tag{2-15}$$

As L is positive the sign of this mixed term depends on the sign of the displacement field and changes with the direction of q. This leads to an asymmetry of the HDS comparing the scattering at $\pm q$ close to a Bragg peak. From the measurements at $\pm q$ these symmetric and antisymmetric contributions can be separated and we obtain the leading term separated ;

$$S_H(q) = (S_H(q_+) + S_H(q_-))/2 = c|f|^2\left|\frac{V^{rel}}{\gamma\Omega}\frac{K}{q}\cos(K \cdot q)\right|^2 . \tag{2-16}$$

The distribution of the intensity around a Bragg reflection is given by the $cos^2(Kq)$ distribution shown in Fig.2-3, the so-called Huang spheres. If q is perpendicular to $K \fallingdotseq G$, there is zero intensity.

For cubic crystals the quantitative description of HDS intensity can be expressed in terms of three quadratic forms of the components of P_{ij} :

$$S_H = c|f|^2\frac{K^2}{q^2}\frac{1}{\Omega^2}\left[\gamma^{(1)}(TrP)^2 + \gamma^{(2)}\sum_{i>j}(P_{ii} - P_{jj})^2 + \gamma^{(3)}\sum_{i>j}P_{ij}{}^2\right] . \tag{2-17}$$

The $\gamma^{(i)}$ depend on the elastic constants C_{ij} and the direction of q and K ; the general expression is given in Refs.[2,3]. Hence from a fit of Eq.(2-17) to the intensity distribution around a suitable Bragg reflection the all parameters can be determined.

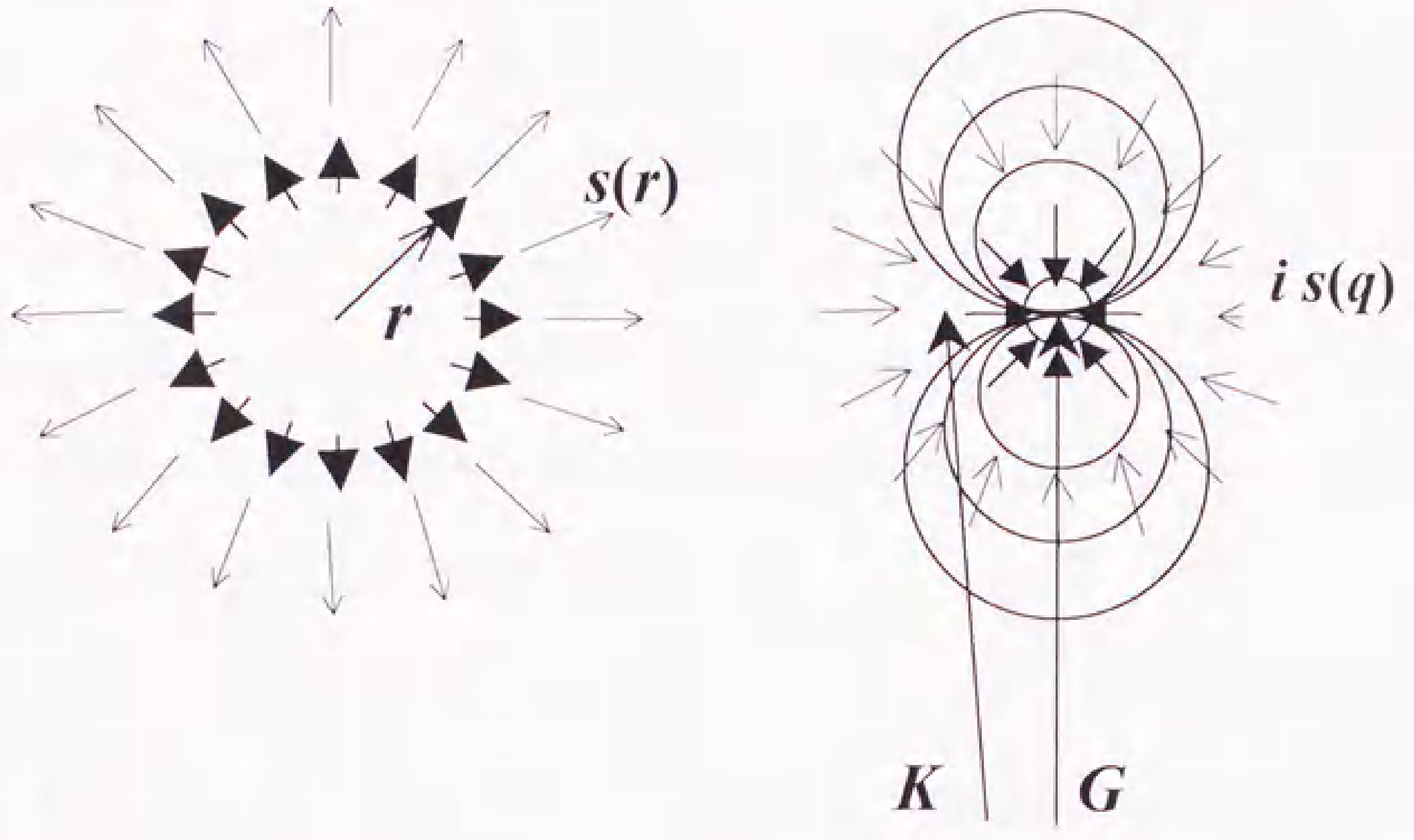

Fig.2-3 (a) Displacement field $s(r)$ and (b) the intensity distribution $Ks(q)$, that is characterized by the Huang spheres. For q perpendicular to G the scattering vector K is perpendicular to $s(q)$.

2.3.2 Dense defect clusters (Stokes - Wilson Scattering)

In the most simple approximation we can consider a defect cluster as a new point defect (Fig.2-4). We start with a random distribution of defects for which the HDS is given by $S_H^1 \approx c(V^{rel})^2$. If it is assumed that upon clustering the long-range strain fields of point defects (that part which gives rise to HDS) superimpose linearly, then for clusters containing n defects, HDS is given by the relation

$$S_H^n \approx (c/n)(nV^{rel})^2 \approx nS_H^1 \ . \tag{2-18}$$

This result can be simply understood as the defects that were scattering independently (and incoherent due to the random distribution) now scatter coherently. This coherence yields a factor of n in the intensity. As the lattice parameter ($\sim c \cdot Tr\,P$) is not affected by this process eventual losses of defects during agglomeration can be detected, and the combination of S_{H} and $\Delta a/a$ yields the increased defect size and the concentration of clusters. The approximations in the calculation of the Huang scattering are valid only in the region $q << 1/R_{\mathrm{cl}}$ where R_{cl} is the distance from the center of the defect cluster to the location where the displacements $S(R_{\mathrm{cl}})$ have fallen to $1/G$. Thus for larger clusters, the regions for measuring S_{Huang} and S_{anti} are closer to the Bragg peaks. For larger values of q the diffuse scattering from an isotropic displacement field can be described by the asymptotic expression [4].

$$S_{ADS} = c|f|^2 \frac{V^{rel}}{4\gamma\Omega^2} \frac{G}{q^4} \phi \ . \tag{2-19}$$

where γ is the Eshelby constant and ϕ is a function of the angle between G and q. Characteristics of the asymptotic scattering are its linear dependence on the defect concentration, proportionality to q^{-4} and independence to cluster size. Although Eq.(2-19) is derived for isotropic defects these characteristics of the asymptotic scattering are quite generally valid. For quantitative results, however, numerical calculations of S_{ADS} are necessary. As the displacement field of a cluster, e.g. a dislocation loop can be calculated by elastic continuum theory [6], the scattering can be calculated in a straightforward manner by the use of Eq.(2-19) [7].

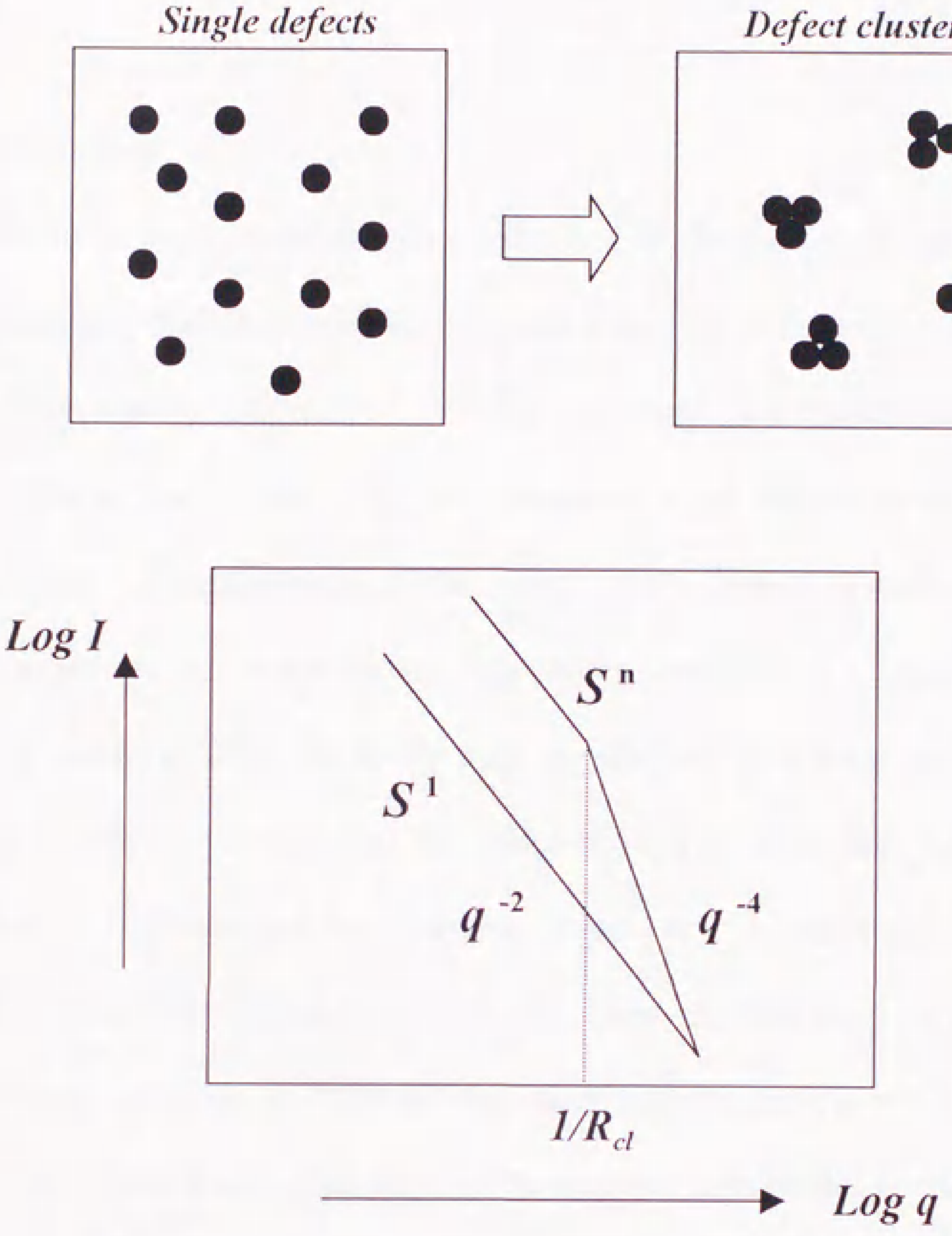

Fig.2-4 Schematics of the formation of defect clusters by the agglomeration of primary point defects and corresponding change of the scattering close to a Bragg peak.

2.4 Experimental technique

2.4.1 Scan technique

In order to exploit the information contained in the scattering function $S(K)$ we have to measure the distribution of the scattered intensity as a function of K , i.e. as a function of the scattering angle 2θ ($\sim|K|$) as well as of the direction within the reciprocal lattice of the crystal (θ or ω-rotation) and single crystal samples are therefore required. Measurements of the change of the lattice as well as of the HDS have been achieved by conventional laboratory techniques (Fig.2-5). The characteristics radiation from an X-ray tube is selected by a bent focussing crystal monochromater, which is necessary in order to obtain sufficient intensity. The scattered radiation is detected at the scattering angle 2θ . A monitor detector samples the incoming beam and allows correction for beam fluctuations. The two major technical advances that yield an order of magnitude improvement in the measuring time are : the rotating anode X-ray generator and at the other end of the system the position sensitive detector that allows the simultaneous measurement within a certain angular region. Figure 2-6 shows a typical setup at a synchrotron. Due to the high intensity of the beam focussing is generally not used and a more convenient flat crystal monochromater arrangement is applied. By rotation of the crystal to the appropriate Bragg angle any wavelength can be selected out of the continuum radiation of the synchrotron, and by using a two crystal arrangement the beam can be kept at a fixed exit position for all wavelengths. The figure shows in addition the different rotation axes that are necessary to align a single crystal.

The θ (or ω) rotation of the sample and the 2θ-rotation of the detector are used in order to achieve scans in a plane of the reciprocal lattice. A radial scan in the reciprocal lattice is achieved by a 1 : 2 coupled motion of sample and detector (θ -2 θ -scan) and is schematically illustrated in Fig.2-7.

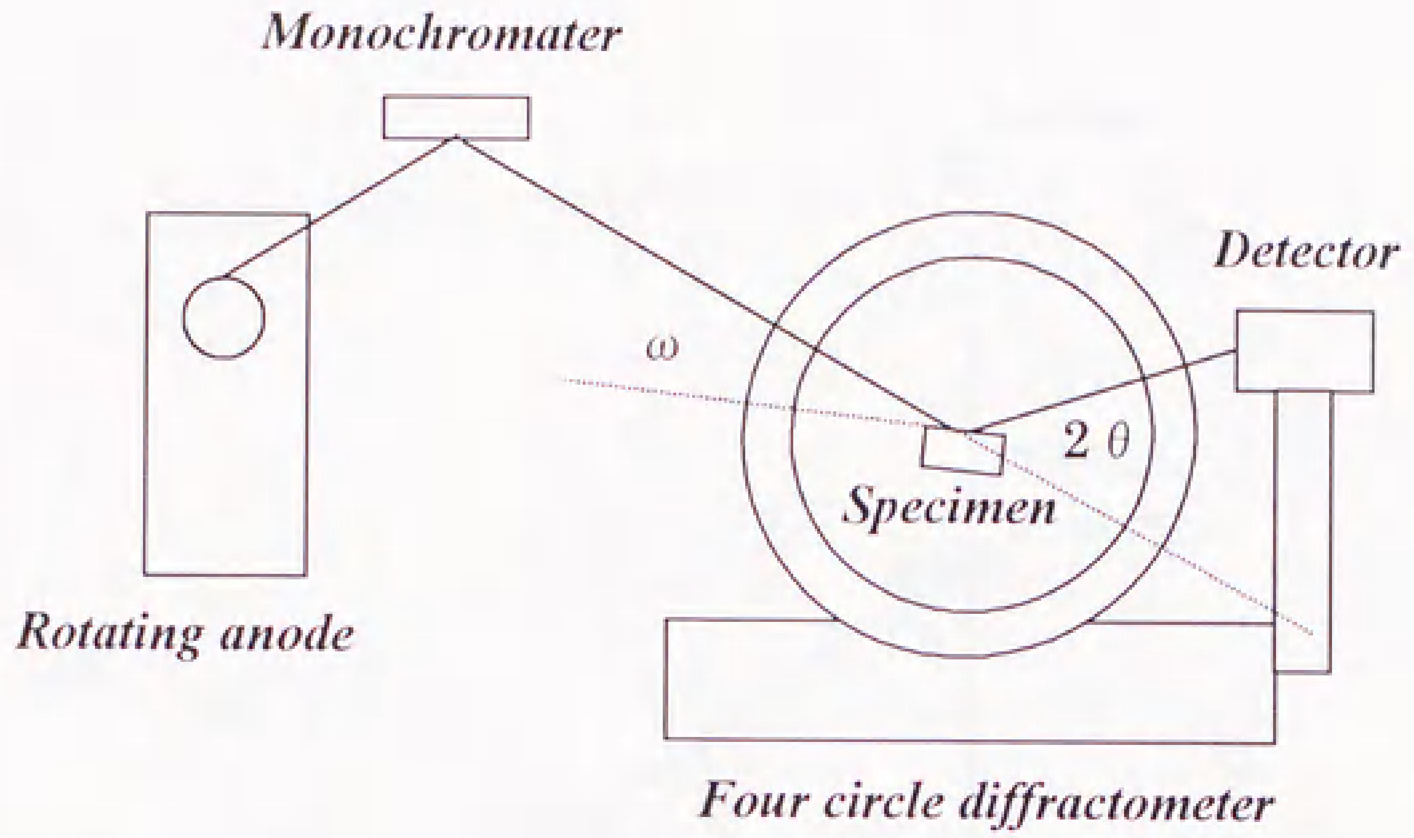

Fig.2-5 Experimental setup of an X-ray diffraction experiment for laboratory System.

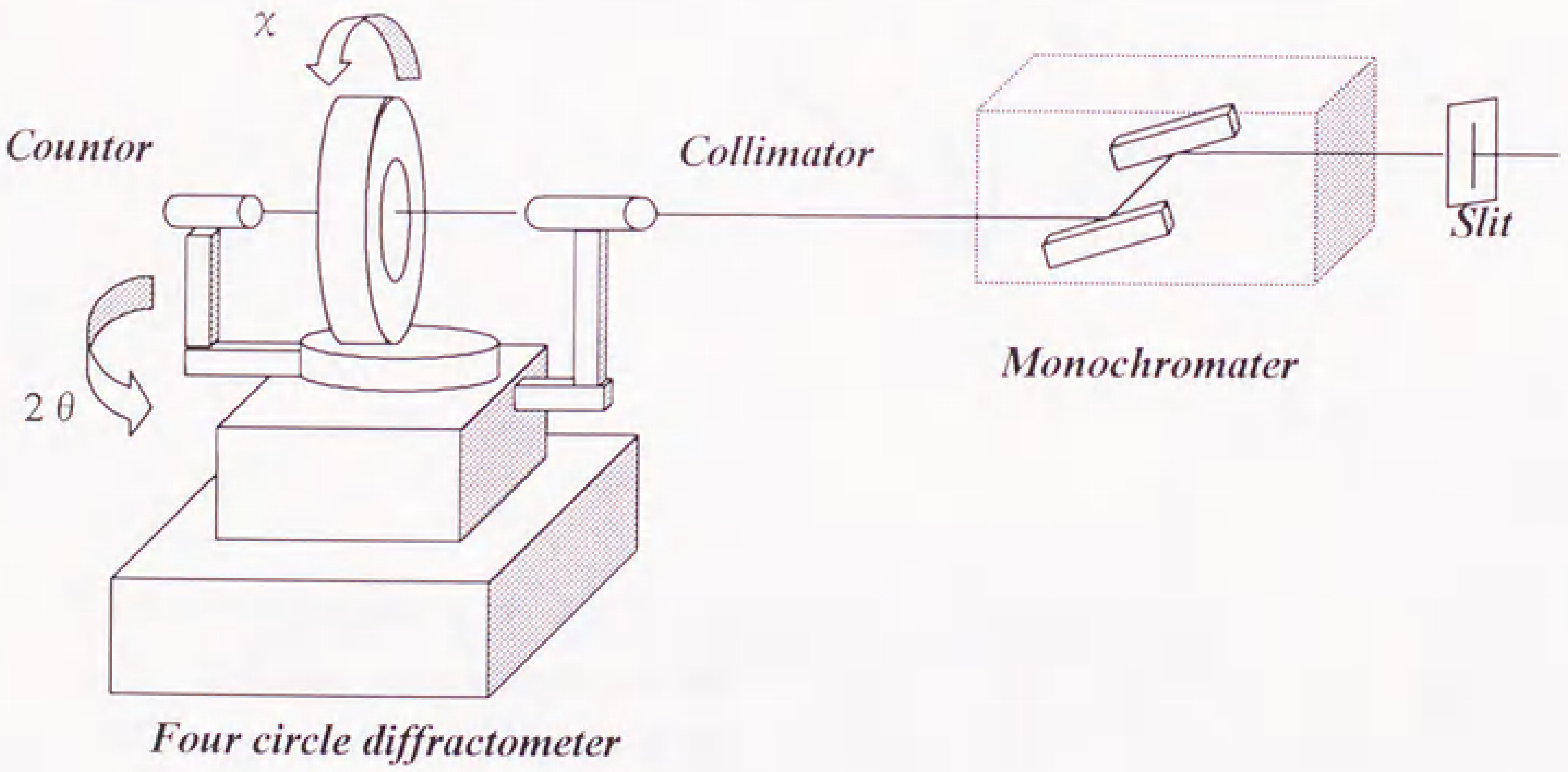

Fig.2-6 Beam line at a synchrotron.

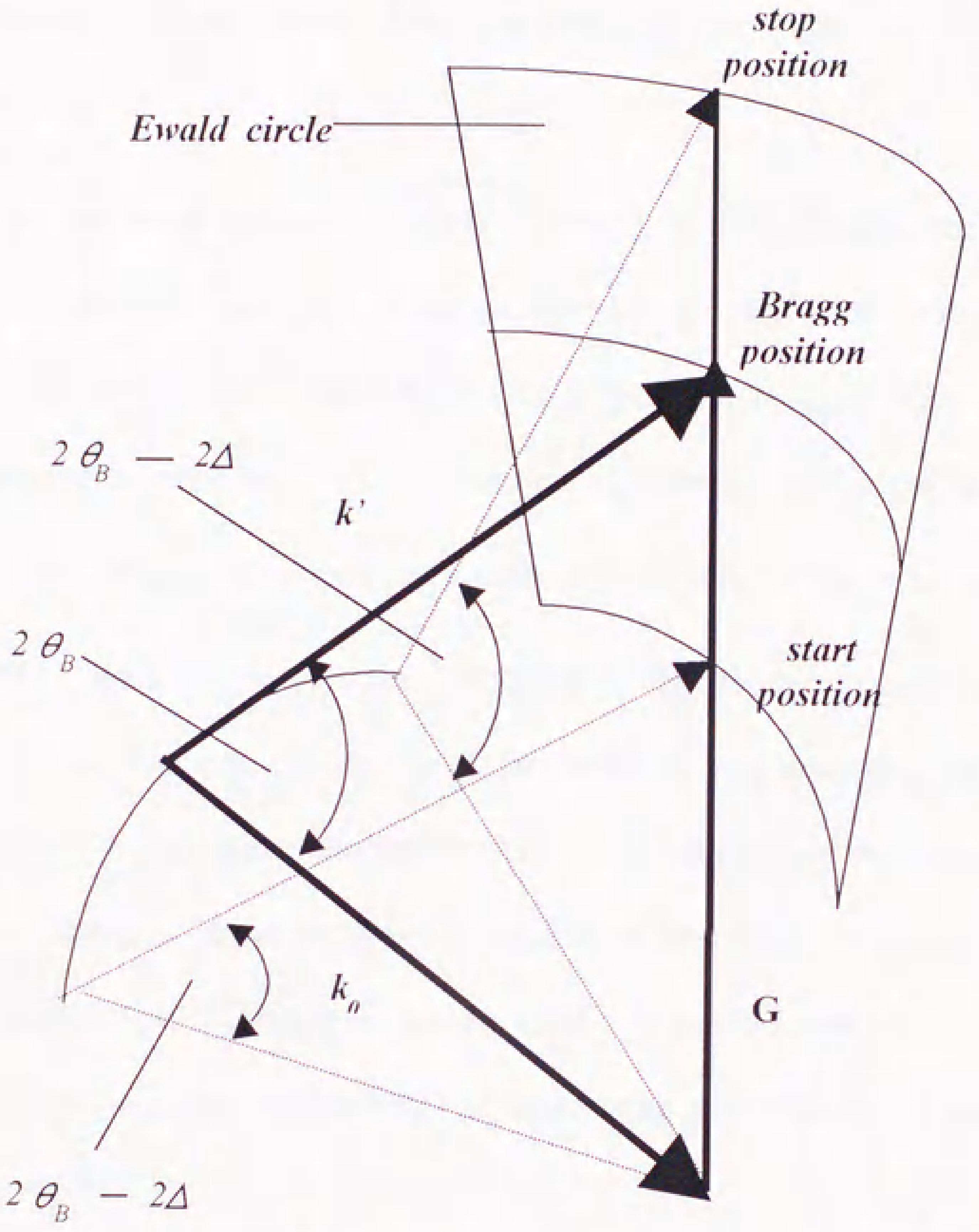

Fig.2-7 Illustration of a θ-2θ scan in a reciprocal space.
The scan starts with an angular deviation $-\Delta$ from the Bragg angle and stops at a deviation $+\Delta$.

2.4.2 Conversion of intensities to absolute units

The scattered intensity obtained experimentally can be written :

$$I(\frac{quanta}{\sec}) = I_0 \cdot A \cdot d_{eff} \cdot N \cdot d \cdot \Omega_2 \cdot p \cdot S(K) \ , \tag{2-20}$$

where I_0 is the incoming intensity (quanta s^{-1} cm^{-2}), A is the illuminated area of the sample, d_{eff} the effective thickness of the sample that is determined essentially by the absorption within the sample. For reflection at a thick sample d_{eff} is $1/(2\mu)$. (for other scattering geometries see Ref.[8]). N is the number of atoms per cm^3. Hence $A \cdot d_{eff} \cdot N$ is the number of scattering atoms. $d\Omega_2$ is size of the solid angle of the scattered beam (area of the detector / distance to the sample squared). p is the polarization factor that depends on the polarization of the incoming beam and the scattering angle. For the determination of $S(K)$, I_0 and the geometrical parameters (A, $d\Omega_2$) must be known. However, I_0 is too high to be measured by quantum detectors. Therefore, a convenient technique is the use of a well known reference scatterer as a calibration sample (e.g. polystyrene) that eliminates the geometrical parameters as well and S(K) is given by

$$S(K) = \frac{I}{I_{cal}} \cdot \frac{(d_{eff}N)_{cal}}{d_{eff}N} \cdot \frac{p_{cal}}{p} \cdot S(K)_{cal} \ . \tag{2-21}$$

The reference sample, polystyrene (C_8H_8), was measured at a scattering angle 2θ of 100° . The experimental cross section given by Sparks and Borie is 61.1 (*e.u.*). Eq.(2) is correct for reflection from an infinitely thick sample in the symmetrical arrangement.

References

[1] P. Ehrhart, *J. Nucl. Mater.*,**216**(1994)170.

[2] M. A. Krivoglaz, *Theory of X-ray and Thermal-Neutron scattering by Real Crystals* (Plenum, New York, 1969)

[3] P. H. Dederichs, *J. Phys.* F**3**(1973)471.

[4] H. Trinkaus, *Phys. Status Solidi* B**51**(1972)307.

[5] H. Trinkaus, *Z. Naturforsch.* 28a(1973)980.

[6] S. M. Ohr, *Phys. Status Solidi* B**64**(1974)317.

[7] P. Ehrhart, H. Trinkaus and B.C. Larson, *Phys. Rev.* B**25**(1982)834.

[8] International Tables of X-ray Crystallography, vol. I-IV (Kynoch Press, Birmingham, 1962)

3. Numerical calculation

3.1 Introduction

Theoretical work has made it possible to treat the small q region near Bragg reflections for arbitrary elastic anisotropy through the use of Fourier transformed elastic Green's functions and the dipole-force tensor of the defects. Therefore, the interpretation of the scattering in the small-q region is quite reliable. However, it is not always possible to limit diffuse scattering measurements to this region for a variety of reasons such as the presence of a distribution of sizes of defects or insufficient crystal perfection. If defects form clusters, the diffuse scattering intensity often become to show q^{-4} dependence. As shown in chapter 1, q^{-2} region where the interpretation is reliable becomes restricted in the small q value. The detailed calculation of the diffuse scattering intensity for q^{-4} region was conducted by some researchers [1,2]. Although they managed to calculate the theoretical intensity by introducing their contrived method for saving the computing time, it seemed complicated. This was due to the fact that the calculation was very time consuming due to the performance of the largest computer at that time.

The basic equation is easy to comprehend as follows ;

$$A(K)=\sum_{m} e^{iK\cdot r_m}(e^{iK\cdot s_m}-1)\pm\sum_{n} e^{iK\cdot(r_n+s_n)} . \tag{3-1}$$

The first sum in Eq.(2-1) describes the diffuse-scattering amplitude (total amplitude minus the Bragg reflection amplitude) from the lattice atoms m displaced from their ideal positions r_m by s_m due to the presence of the dislocation loop ("distortion scattering"). The second sum represents the scattering amplitude from the additional or missing atom n, which define the lattice defect ("Laue scattering").

K is the scattering vector. Larson et al. [1] wrote the amplitude of diffuse scattering in the form of five components as

$$\begin{aligned}
A_1^S(K) &= \frac{b\pi R^2}{V_c}\frac{2J_1(QR)}{QR}e^{i\Delta_h^L}, \\
A_2^A(K) &= -h_i G_{in}\frac{P_{nm}q_m}{V_c}\frac{2J_1(QR)}{QR}, \\
A_2^S(K) &= -q_i G_{in}\frac{P_{nm}q_m}{V_c}\frac{2J_1(QR)}{QR}, \\
A_3^S(K) &= \frac{1}{V_c}\int \cos(q\cdot r)\left[\cos(K\cdot s(r))-1\right]dr, \\
A_3^A(K) &= \frac{1}{V_c}\int \sin(q\cdot r)\left[\sin(K\cdot s(r))-K\cdot s(r)\right]dr,
\end{aligned} \tag{3-2}$$

where

b : the Burgers vector

R : the radius of dislocation loop

V_c : the atomic volume

J_1 : the first-order Bessel function

Q : the projection of q onto the plane of the loop

q : the momentum transfer relative to a reciprocal lattice vector

$s(r)$: the displacement from the average lattice position

G_{in} : the lattice Green function

However, the imaginary parts caused by the different stacking sequence associated with the intrinsic vacancy loop and the extrinsic interstitial loop seem not to be taken into considered as performed by Ehrhart et al. [2].

3.2 Improvement of calculation method

Although the calculation of diffuse scattering had been time consuming [2], the calculation became to be less time consuming nowadays due to the high-performance of computer. The calculation could be done even by taking the positions of individual lattice atoms in the computer program. This made it possible to calculate directly from Eq.(3-1) without using Eqs.(3-2) or (3-3), therefore, the program became very simple to comprehend as follows.

The scattering amplitude *S*(*K*) at a point *K* in reciprocal space resulting from a loop can be written as

$$A(K) = \sum_{j \le LOOP} e^{iK \cdot r_j^L} + \sum_{j \le SPACE} (e^{iK \cdot r_j'} - e^{iK \cdot r_j}) , \tag{3-4}$$

where r_j^L are the positions of the atoms in the loop and $r_j' = r_j + s_j$ are the positions of the remainder of the atoms in the crystal which are displaced s_j from the average lattice position r_j.

Introducing the displacement s_j from the average position, Eq.(3-4) can be written as

$$A(K) = \sum_{j \le LOOP} e^{iK \cdot r_j^L} + \sum_{j \le SPACE} e^{iK \cdot r_j} \left(e^{iK \cdot s_j} - 1 \right) , \tag{3-5}$$

Writing the scattering vector $K = h + q$ in terms of a reciprocal lattice vector h and the momentum transfer q relative to h, $A(K)$ can be put in a convenient form by introducing a phase factor (not affecting the intensity) $e^{ih \cdot r_j}$. With this phase factor, and using the fact that $e^{h \cdot r_j} \equiv 1$,

$$A(K) = \sum_{j \le LOOP} e^{i\left(h \cdot r_j^L + q \cdot r_j^L\right)} + \sum_{j \le SPACE} e^{ih \cdot r_j} e^{iq \cdot r_j} \left(e^{i\left(h \cdot s_j + q \cdot s_j\right)} - 1 \right) . \tag{3-6}$$

For making easy to programming, this formula can be written as

<u>vacancy loop</u> ;

$$A(K) = - \sum_{j \le LOOP} e^{iK \cdot r_j^L} + \sum_{j \le SPACE} \left(e^{iK \cdot r_j} - e^{iK \cdot r_j} \right) , \tag{3-7}$$

interstitial loop ;

$$A(K) = -\sum_{j\leq LOOP} e^{i\left(h\cdot r_j^{L} + h\cdot s_j + q\cdot r_j^{L} + q\cdot s_j\right)} + \sum_{j\leq SPACE} e^{ih\cdot r_j}\, e^{iq\cdot r_j}\left(e^{i(h+q)\cdot s_j} - 1\right) . \tag{3-8}$$

The summation is restricted in a loop for $\sum\limits_{j<LOOP}$, and in all space for $\sum\limits_{j<SPACE}$. However, the summation, $\sum\limits_{j<SPACE}$, is saved since the strain field become negligible at the position where is far from a loop. In this study, therefore, the summation volume is 13R.

On the other hand, the reduction of calculation time can be obtained in the calculation program because the displacement fields differ only in sign in the continuum approach.

Therefore, Eq.(3-7) and (3-8) can be written as follows.

vacancy loop :

$$A(K)\big|_{q>0} = -\sum_{j\leq LOOP} e^{i\left(h\cdot r_j^{L} + h\cdot s_j + q\cdot r_j^{L} + q\cdot s_j\right)} + \sum_{j\leq SPACE} e^{ih\cdot r_j}\, e^{iq\cdot r_j}\left(e^{i(h+q)\cdot s_j} - 1\right) . \tag{3-9a}$$

$$A(K)\big|_{q<0} = -\sum_{j\leq LOOP} e^{i\left(h\cdot r_j^{L} + h\cdot s_j - q\cdot r_j^{L} - q\cdot s_j\right)} + \sum_{j\leq SPACE} e^{ih\cdot r_j}\, e^{-iq\cdot r_j}\left(e^{i(h-q)\cdot s_j} - 1\right) . \tag{3-9b}$$

interstitial loop :

$$A(K)\big|_{q>0} = \sum_{j\leq LOOP} e^{i\left(h\cdot r_j^{L} + q\cdot r_j^{L}\right)} + \sum_{j\leq SPACE} e^{ih\cdot r_j}\, e^{iq\cdot r_j}\left(e^{i\left(h\cdot s_j - q\cdot r_j\right)} - 1\right) . \tag{3-10a}$$

$$A(K)\big|_{q<0} = \sum_{j\leq LOOP} e^{i\left(h\cdot r_j^{L} - q\cdot r_j^{L}\right)} + \sum_{j\leq SPACE} e^{ih\cdot r_j}\, e^{-iq\cdot r_j}\left(e^{i\left(h\cdot s_j + q\cdot s_j\right)} - 1\right) . \tag{3-10b}$$

In order to limit computer time the lattice sum must be confined someway. Since a sharp truncation of the sum results in spurious ripples in the intensity distribution, a smoothly decaying function should be used as has been discussed by Keating and Goland [3]. Accordingly, we have introduced a Gaussian function *exp*[-

$(1/2d)r^2]$ to Eqs.(3-9) and (3-10).

Mathematically, this is related to a convolution of the intensity $I(q)$ with a Gaussian function $\exp(-\frac{1}{2}d^2q^2)$. The corresponding smearing out of the intensity distribution can be kept negligible compared to the resolution of the experiments, and still results in significant computational savings. Values of d ～ 2 to 3 times the loop radius (R) were found to be reasonable values for 20-Å loops as discussed below.

In the following, the effect of this Gaussian function used in this study on the absolute intensity of diffuse scattering is examined. The absolute value of diffuse-scattering intensity is given through introducing this Gaussian function for the real space :

$$e^{-\frac{r^2}{2d^2}} . \tag{3-11}$$

However, the Fourier transform of this function should be examined since the intensity of diffuse-scattering is calculated for reciprocal lattice space. The Fourier transform of Eq.(2-12) can be written as

$$\frac{d}{\sqrt{2\pi}} e^{-\frac{d^2q^2}{2}} , \tag{3-12}$$

by using the following formula of the Fourier transform :

$$\frac{1}{2\sqrt{\pi a}} e^{-\frac{y^2}{4a}} = \frac{1}{2\pi} \int_{-\infty}^{\infty} dx e^{ixy} e^{-ax^2} \tag{3-13}$$

The Gaussian function can not affect the absolute intensity of diffuse-scattering since the integration of Eq.(3-13) in the section [-∞, ∞]

$$\frac{d}{\sqrt{2\pi}} \cdot \frac{\sqrt{2\pi}}{d} = 1 ,$$

by using the following formula :

$$\int_{-\infty}^{\infty} dx e^{-a^2x^2} = \frac{\sqrt{\pi}}{a} . \qquad (3\text{-}14)$$

3.3 Results and discussion

The calculation of diffuse-scattering intensity for evaluating the size distribution of loops requires the calculations of the displacement fields corresponding to the loop radius R. Therefore, first of all we calculated the displacement field. In Fig.3-1 and 3-2, I have plotted the displacement component u_x and u_z of prismatic loops in the (111) plane of Cu as a function of distance along the loop axis. The component u_z is normalized with respect to the magnitude of the Burgers vector b. The component was also in good agreement with that reported by Ohr [4].

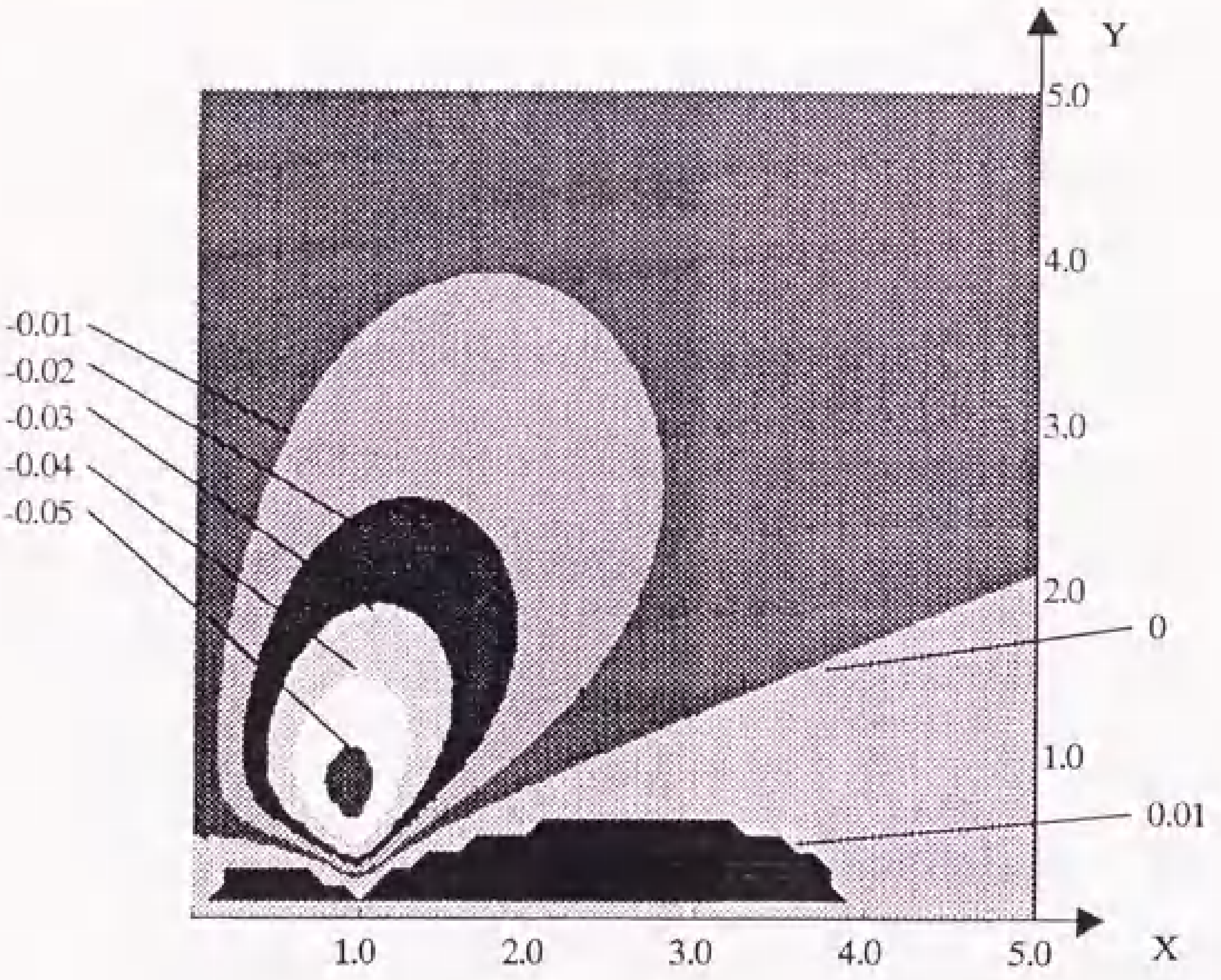

Fig. 3-1 Equi-displacement contour plot of u_z in units of b for a prismatic dislocation loop in the (111) plane of Cu

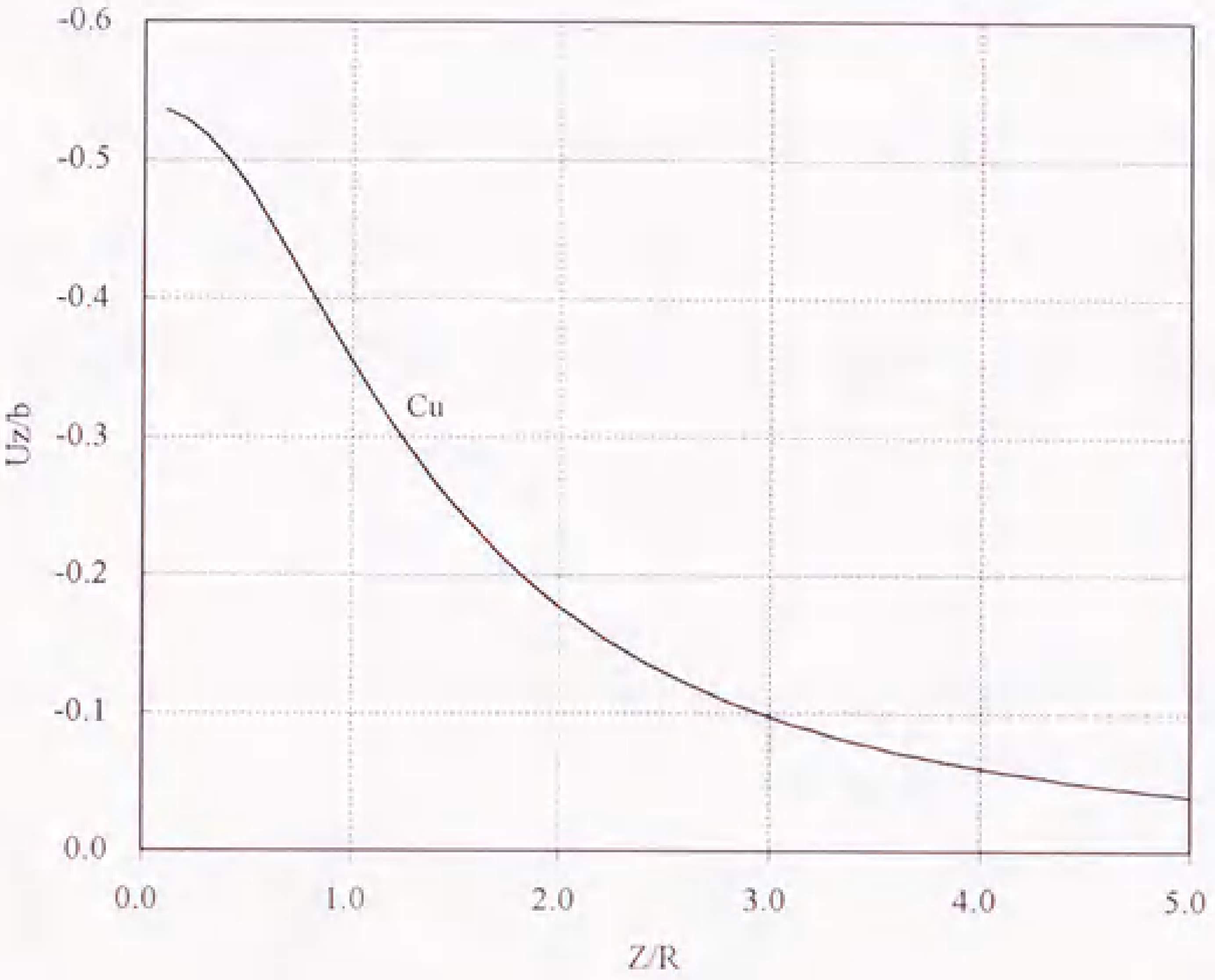

Fig. 3-2 Displacement component u_z at $x = y = 0$ as a function of z for a pure edge prismatic dislocation loop (Frank-type loop) in the (111) plane of Cu.

It is concluded that the displacement field obtained in this study is in good agreement with that calculated by Ohr. Using this displacement field, I secondly calculated the diffuse-scattering intensities from various *FCC* metals under some experimental conditions. Firstly, the effect of d in the Gauss function (Eq.(3-11)) was examined. Ehrhart et al. introduced this function for only small q value, however, this function should be used carefully from the view point of its effect on the absolute intensity of diffuse scattering. The calculations from Frank-type dislocation loop with radius R = 10Å in Ni for d = 0, 1, 2, 3 and 4 were performed as shown in Fig.3-3. Some ripples in the scattering intensity for d = 0 are seen, indicating the presence of the effect of artificial periodicity of crystal lattice. This effect was pointed out by Keating and Goland [3]. However, this effect can be avoided by introduction of Gauss function as shown in Fig.3-3. It seems that the most appropriate value of d is from 3 to 4 from the view points of the degree of the deviation from the original intensity distribution ($d = 0$). It was reported by Ehrhart et al. that the value of $d \sim 2$ to 3 was reasonable. Therefore, the value of $d \sim 2$ to 3 was used for this theoretical calculation of diffuse scattering.

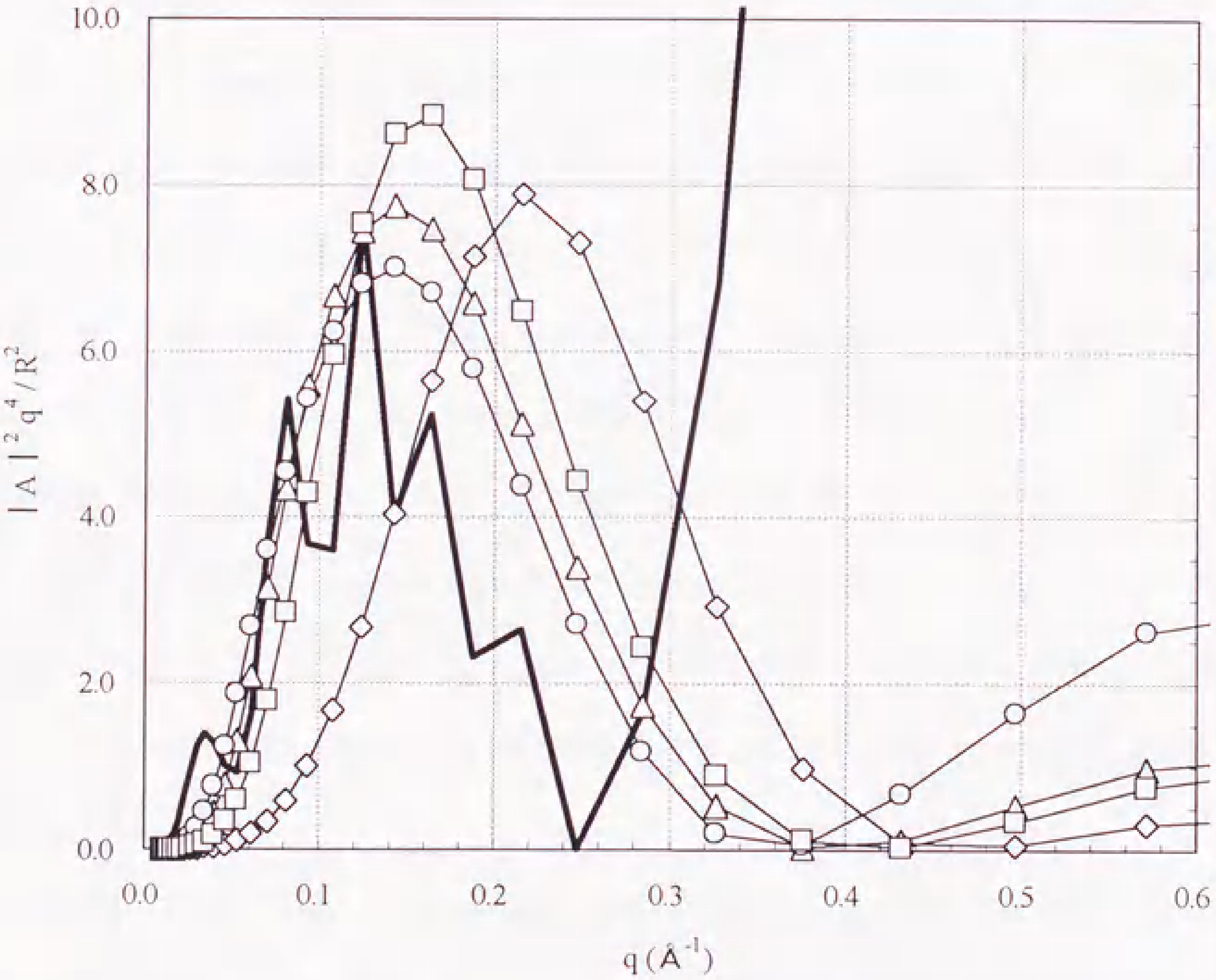

Fig.3-3 The d-dependence of theoretical diffuse-scattering intensity from a Frank-type loop in Ni for $q > 0$. The thick solid line corresponds to the theoretical diffuse scattering intensity for the case of $d = 0$.
○ : $d = 1$ △ : $d = 2$ □ : $d = 3$ ◇ : $d = 4$

Next, the theoretical diffuse-scattering intensity from a Frank-loop in Al was calculated to compare with the results obtained by Ehrhart et al. [3]. Figure 3-4 shows the result for four order of the (*hhh*) reflection. It was reported by Ehrhart et al. that there were oscillations of diffuse-scattering intensity in a plot of Iq^4. These oscillations are also appeared in this study as shown in Fig.3-4, therefore, the theoretical calculation based on our simple program was demonstrated to be suitable and applicable to other metals.

In addition to the normal case (Burgers vector b is parallel to both q and h direction), we calculated the theoretical diffuse-scattering amplitude for the case that the loops exist on other {111} planes since the existence of loops on other planes seemed to cause an unexpected intensity. The results showed that the intensities of diffuse-scattering from other three planes equivalent to {111} were negligible small compared with that from the plane perpendicular to (111) direction (Fig.3-5). Therefore, the theoretical intensity of diffuse-scattering for the (111) [111] case from loop lying in the {111} plane is almost identical to that from loops lying on the plane perpendicular to (111) direction. The size distribution and the number density of loops can be obtained from the fitting of this theoretical diffuse-scattering intensity to experimental one.

Finally, I calculated the theoretical diffuse scattering intensities from a perfect loop lying on the {111} plane in Cu and Ni. The result for a perfect loop was compared with that for a Frank-type loop. Figure 3-6 shows that the theoretical intensity from both perfect- and Frank-loop with a raduis R = 10Å in Cu for (222) [111] case. It is seen in this figure that the difference of the distribution of diffuse-scattering intensity between perfect- and Frank-type loop is small.

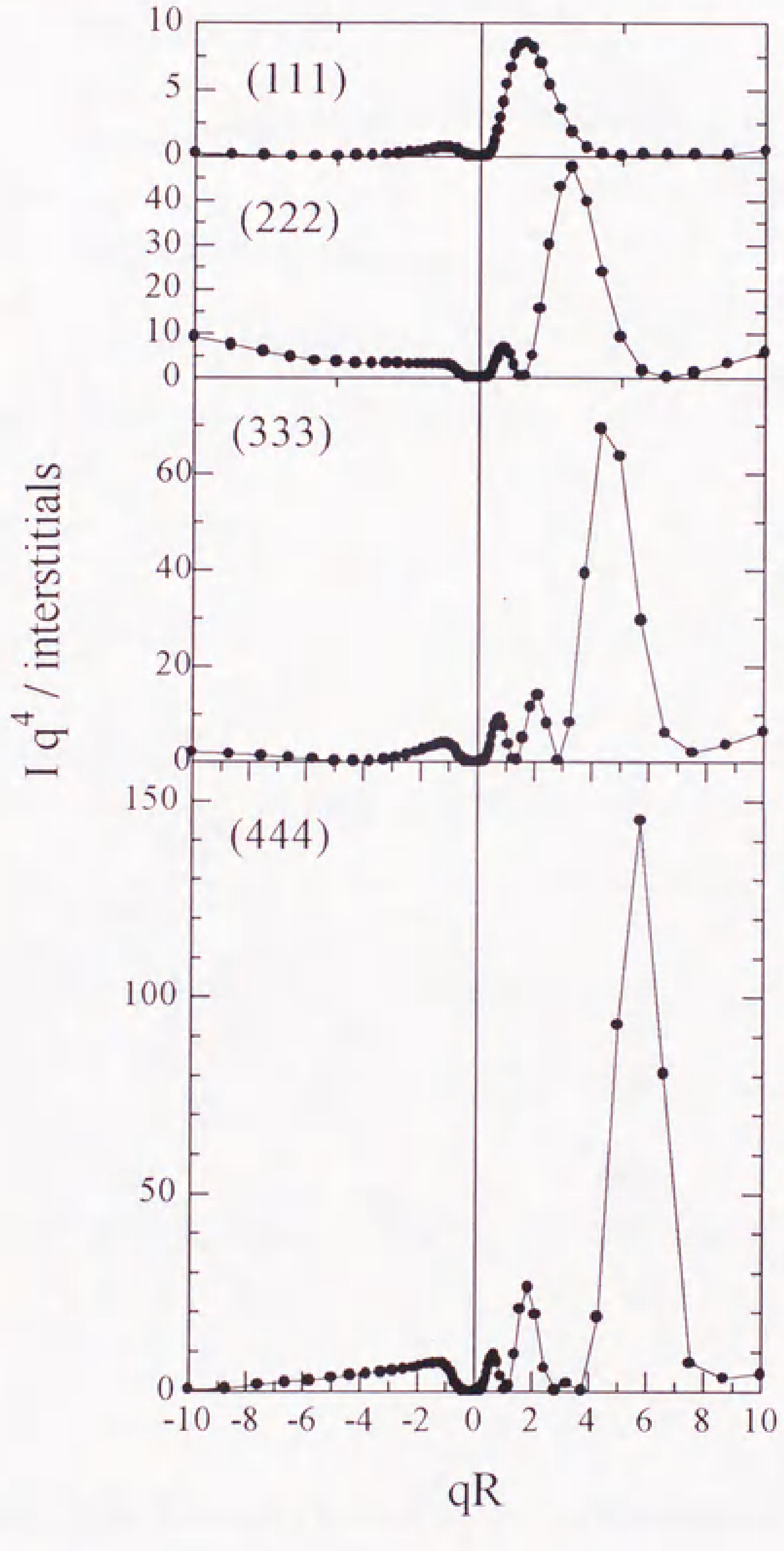

Fig.3-4 Oscillations of the intensity from a loop parallel to [111], the Burgers vector *b* = (a/3)[111], at (111), (222), (333) and (444) reflections.

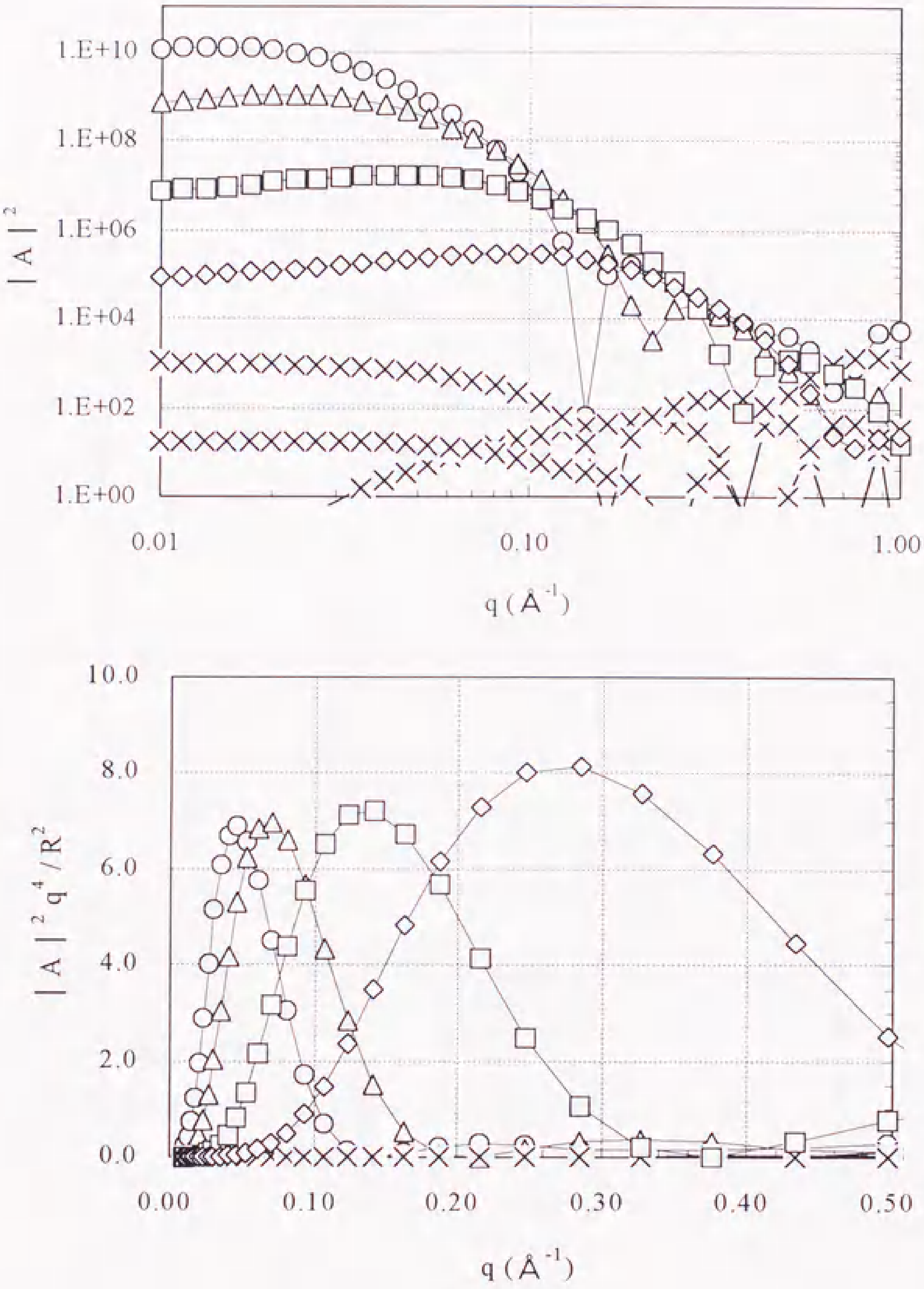

Fig. 3-5 The diffuse-scattering intensities from a Frank-type interstitial-loop lying on the equivalent four planes to {111} plane.

○ : loop radius R = 30Å, △ : 20Å, □ : 10Å, ◇ : 5Å,
× : 10Å (the intensities from other three planes)

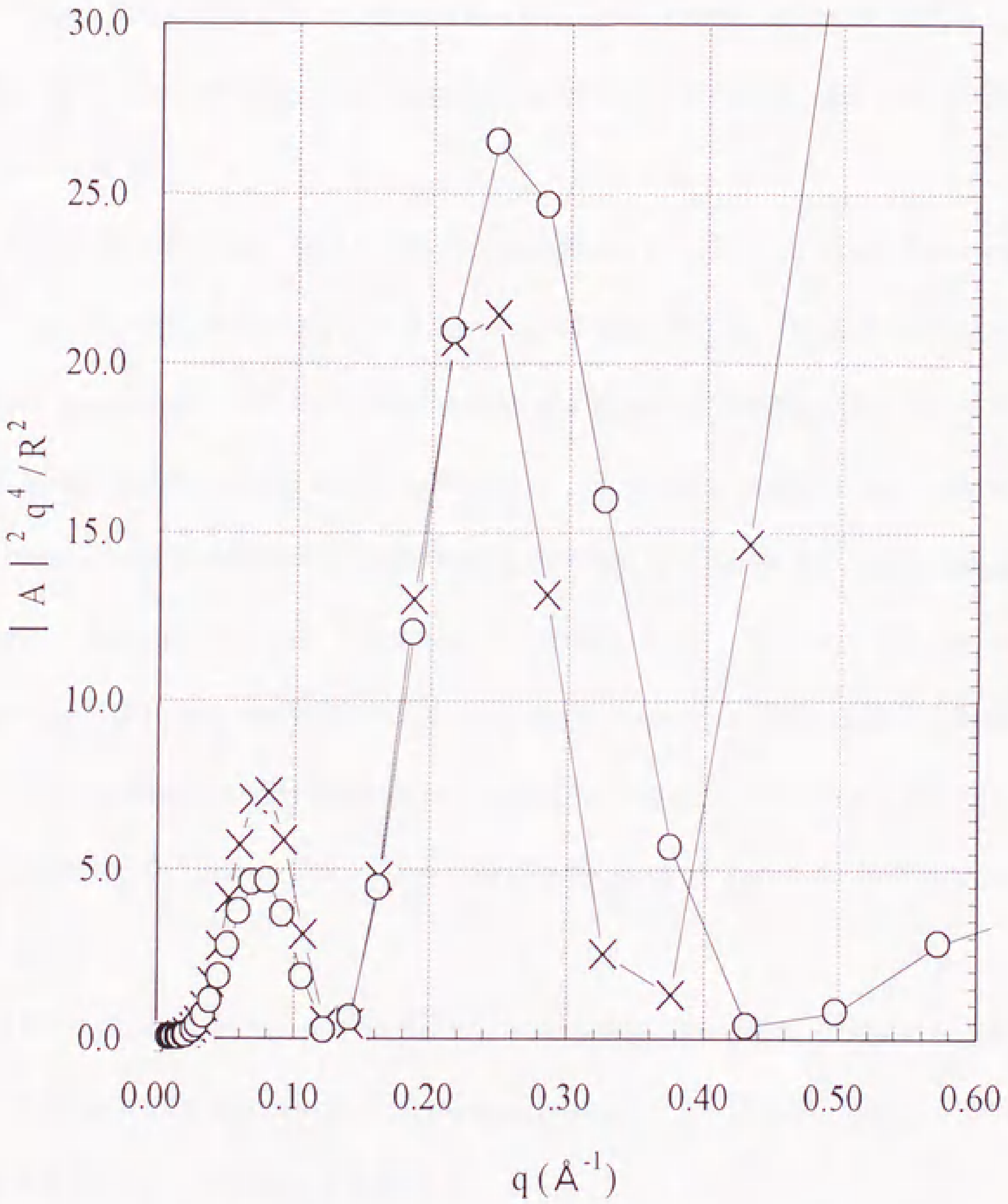

Fig. 3-6 The diffuse scattering intensities from Frank- and perfect-interstitial loop with a radius R = 10 Å in Cu for (222) [111] case.

○ : Frank-loop
× : Perfect loop

For the comparison, the (111) [111] case was calculated as shown in Fig.3-7. It was seen the difference of the scattering intensity for (111) [111] case between perfect- and Frank-loop become large compared with that for (222) [111].

Figure 3-8 shows that in Ni for the (111) [111] case. As seen in this figure, there is large difference of scattering intensity between for Frank- and for perfect-loop as observed for Cu.

There is evidence from TEM investigation [6] that most of the loops (about 90%) are of the Frank type and only 10% are perfect loop in ion-irradiated Ni. However, loops have been observed to transform into glissile perfect loops within their mutual strain field or close to the surface [7]. The latter process may lead to a loss of perfect loops and, in addition, the diffuse scattering of smaller loops that might not have completely relaxed is better described by perfect loop. Because of this uncertainly, Ehrhart et al. [8] used the mixture of 50% Frank loop and 50% perfect interstitial loop for evaluating the size distribution of interstitial loops. Therefore, the same method was applied for the estimation of the size distribution of vacancy- and interstitial-loops in this study.

The q-dependencies of the diffuse scattering intensities calculated theoretically for a vacancy- and a interstitial-loop with a radius $R = 10$, 30 and 50 Å in this study are shown in Fig.3-9 as typical examples.

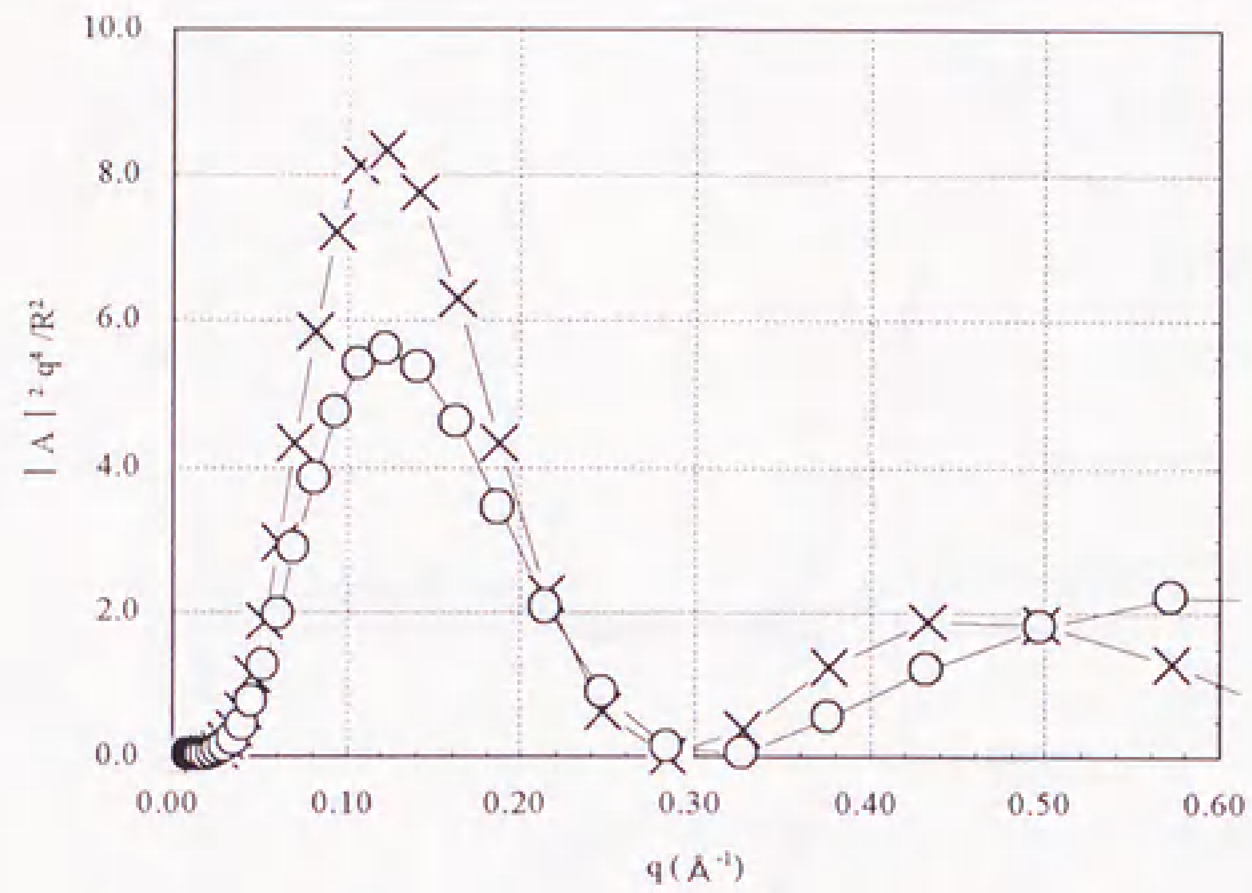

Fig. 3-7 The diffuse scattering intensities from Frank- and perfect-interstitial loop with a loop radius R = 10 Å in Cu for (111) [111] case.

○ : Frank-loop × : Perfect loop

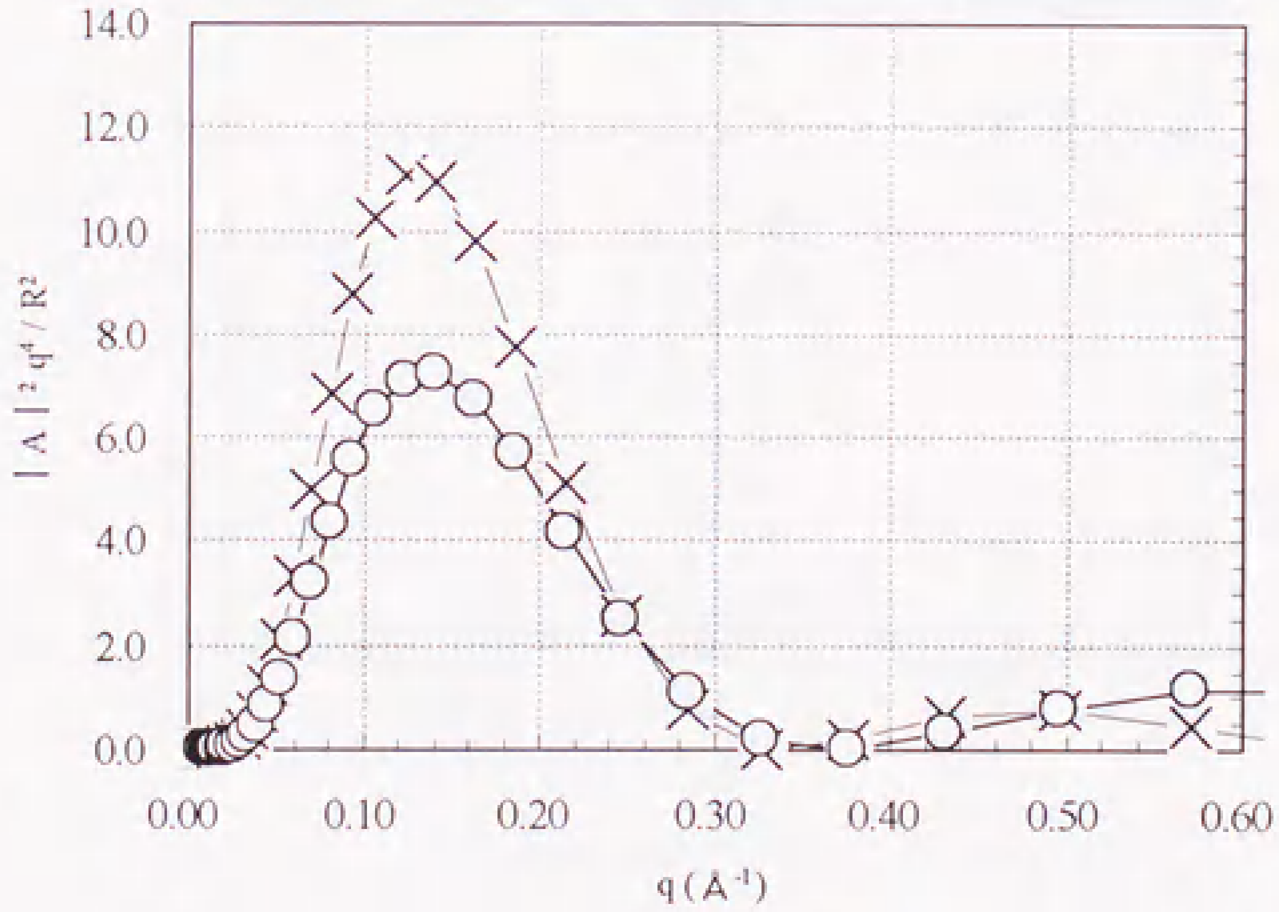

Fig.3-8 The diffuse scattering intensities from Frank- and perfect-interstitial loop with a loop radius R = 10 Å in Ni for (111) [111] case.

○ : Frank-loop × : Perfect loop

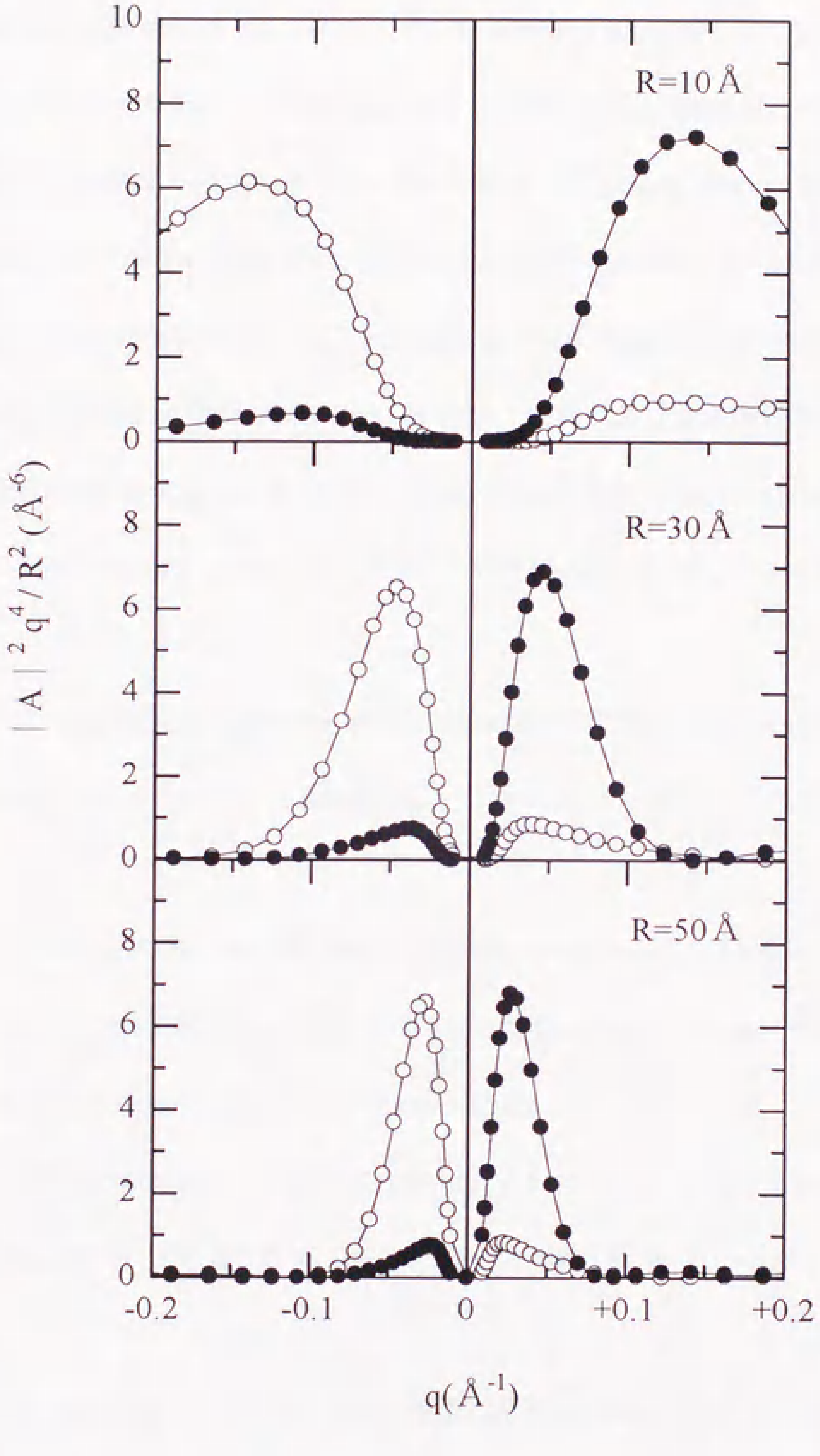

Fig. 3-9 Intensity of diffuse x-ray scattering scaled by q^4/R^2 calculated theoretically for vacancy (white symbols) and interstitial (black symbols) loop in Ni.

3.4 Conclusion

The detailed calculation of the diffuse scattering intensity for q^{-4} region were conducted by some researchers. Although they could calculate the theoretical intensity by introducing their contrived method by the request of saving the computing time, it seemed difficult to follow without the original computer program or some guidance by them. The theoretical calculation of the diffuse scattering intensity was very time consuming even for the largest computer at that time In this study, the calculation could be done even by taking the positions of individual lattice atoms in the program by the aid of high-performance recent computer. The obtained results were summarized as follows :

(1) The most appropriate value of d in Gaussian function used for the theoretical calculation of DXS intensity was determined. The value of $d \sim 2$ to 3 was used in this study.

(2) From the comparison the theoretical diffuse-intensity for high order reflection from a dislocation loop in Al, the theoretical calculation based on our simple program was reliable, and moreover, applicable to other metals.

(3) The theoretical intensity of diffuse-scattering from loop lying in the {111} plane was almost identical to that from a loop lying in the plane perpendicular to (111) direction.

(4) From the calculation of the theoretical diffuse-scattering intensities from a Frank-type loop and a perfect loop, it was revealed that there was a difference among them. Precise individual estimation of the size distribution of the different type defect under their coexistent condition seemed difficult, however, this problem seemed to be overcame by the combination with other experimental tool.

References

[1] B. C. Larson and W. Schmatz, *Phys. Stat. Sol.* (b)**99**(1080)267.

[2] P. Ehrhart, H. Trinkaus and B. C. Larson, *Phys. Rev.* B**25**(1982)834.

[3] D. T. Keating and A. N. Goland, *Acta. Cryst.* A**27**(1971)134.

[4] S. M. Ohr, *Phys. Status Solidi* B**64**(1974)317.

[5] S. I. Rao, C. R. Houska, K Grabowski, G. Ice and J. Sparks, *J. Appl. Phys.* **69**(1991)8104.

[6] J. Narajan and B. C. Larson *J. Appl. Phys.* **48**(1977)4536.

[7] G. Das and T. E. Mitchel, *J. Nucl. Mater.*,56(1975)297.

[8] P. Ehrhart and R. S. Averback, *Phil. Mag.* A**60** (1989) 283.

4. Defect clusters in pure Ni irradiated with high-energy ions

4.1 Introduction

The defect formation in metals by ion-irradiation has been of great interest because the cascade damage by ions is thought to simulate the damage structure by fission and fusion reactor irradiations. The displacement cascades introduce not only Frenkel pairs but also defect clusters. To investigate the defect formation processes by ions, the annealing experiments after low temperature irradiation with < 1MeV ions have been performed by Averback et al [1-3]. From these studies, it was revealed that the stage I recovery in metals decreased as the energy density in cascade increases. They concluded this phenomena to be caused by the instability of close defect pairs in the vicinity of energetic displacement cascades. This phenomena, energy transferred to the region around pre-existing defects cause their annihilation, is called "radiation annealing". Iwase et al. also performed the post-irradiation annealing experiments but after around 100MeV ion irradiation [4-6]. Typical example of recovery curves $\Delta\rho/\Delta\rho_0$ and the temperature derivatives of the recovery curves $-d(\Delta\rho/\Delta\rho_0)/dT$ as functions of the annealing temperature T in the low-temperature region are shown in Fig.1-2 (a) and (b). The reduction of stage I recovery is seen for high-energy heavy-ion irradiation as observed by Averback et al. The anomaly of the stage I recovery at different energies and different projectile species were compared in terms of the spectra of PKA energy. As a parameter that characterizes a PKA energy spectrum, Averback et al. employed the PKA median energy $T_{1/2}$. The PKA median energy means that half of the displaced atoms result from PKA's with energies higher than $T_{1/2}$. The amounts of the stage I recovery in Ni are plotted in Fig.1-3 as a function of $T_{1/2}$. As can be seen in this figure, for the low-energy ion-irradiation, the amount of the stage I recovery change systematically with increasing PKA median energy. For high-energy ion-irradiation, the behavior of the stage I recovery is greatly different from that for the low-energy ion-irradiations observed by Averback et al. For I-ion irradiation, the stage I peak nearly completely disappears, and moreover, even the recovery peak around 100K disappears. Thus, the anomalous reduction of the stage I recovery for high-energy ion-irradiations is not related to the PKA median energy, and it can not be explained within the framework of the defect formation and the radiation annealing by the nuclear collisions. For high-energy heavy ions cause high-density electron excitations along their ion paths in solids. The amount of electron excitations is given by the electronic stopping power, i.e., the energy transferred from ions to electrons in the specimen per unit length of the ion path. In order to study the effect of this thermal spike phenomenon due to electron excitations on the stage I recovery, they plotted the amount of the stage I recovery in Ni as a function of the electronic stopping power (Fig.1-4). This figure shows that the amount of the stage I recovery in Ni is strongly related to the electronic stopping power.

Radiation defects have been known to induce diffuse X-ray scattering (DXS) around the Bragg peaks. The intensity distribution of this diffuse scattering contains detailed information on the radiation defects. The DXS technique has, therefore, become an important method for the determination of the defect structures (i.e. defect types and size distribution of each defect) [7]. Furthermore, diffuse X-ray scattering has been used widely for the investigation of atomic point defects and smaller sized defect clusters formed under the annealing experiments combined with electrical resistivity. As has been investigated by DXS experiments [8], the recovery of defects occurs in several temperature ranges as a result of thermally activated motion of the defects. It was revealed that the recombination of close Frenkel-pairs occurred at stage $I_{A\sim C}$ (below 60K). At stage $I_{D,E}$ (45-60K), the recombination of Frenkel-pairs occurs due to the long-distance migration of interstitials. The di-interstitials forms and interstitial loop begin to grow by the absorption of interstitials during the stage II. As seen in Fig.1-7, the intensity of DXS from this interstitial clusters (loops) become maximum at around 300K. The electrical resistivity change is not sensitive to the formation of interstitial clusters where during thermal annealing. Vacancies become to migrate and recombine with interstitial loops at stage III. Therefore, the DXS experiments around 300K make it easy to investigate the defect structure. As mentioned above, the resulting defect structures for high-energy ion-irradiation are expected to be affected by the radiation annealing. The radiation annealing model is, in certain respects, oversimplified. In particular, the possibility of interstitial clustering, either during the thermal spike or isochronal annealing, is neglected [1]. Therefore, it seemed important to investigate this phenomena by DXS experiment.

In this study, the DXS experiments were performed at room temperature on pure Ni irradiated with 150MeV phosphorus ions and 85MeV iodine ions at low temperature. The resulting structures at 300K (end of stage-II) were analyzed by fitting the theoretical diffuse X-ray scattering intensities of the dislocation loops to the experimental ones. The thick specimens were used in this experiments since the specimen surface has been known to work as sinks for interstitial atoms for thin specimen.

4.2 Experimental

4.2.1 Samples and irradiation condition

High purity single-crystal samples of pure Ni were spark-cut from large single crystals supplied by Johnson Mathey Chemicals Ltd (JMC). The large single crystals of 99.998% purity were grown by the Czochoralski method. The size of all samples was about $10\times5\times1$ mm^3. The irradiation with 150MeV phosphorus ions (P^{9+}) was performed up to doses of 5.3×10^{13}, 1.6×10^{14} and 4.1×10^{14} ions/cm^2 by the JAERI Tandem accelerator at 30K. The irradiation with 85MeV phosphorus ions (I^{7+}) was performed up to a dose of 1.9×10^{13}ions/cm^2 by the JAERI Tandem accelerator at 50K. The irradiation experiments were always performed in a vacuum of 1×10^{-6} Torr.

Figures 4-1 show depth profile of both displacement damage (vacancies) and the energy density of electron-excitation calculated with TRIM code [9] for each irradiation under the usual assumption of threshold energy of 33eV. These figures show only surface region since the effective thickness for DXS study is 5μm. The projected range of phosphorus ions was 18μm, therefore, chemical effect of phosphorus on defect clustering is thought to be negligible. The projected range of iodine ions was 6 μm, however, chemical effect of iodine on defect clustering has not been reported. The stopping power along an ion path is so large that the annihilation of defects is expected.

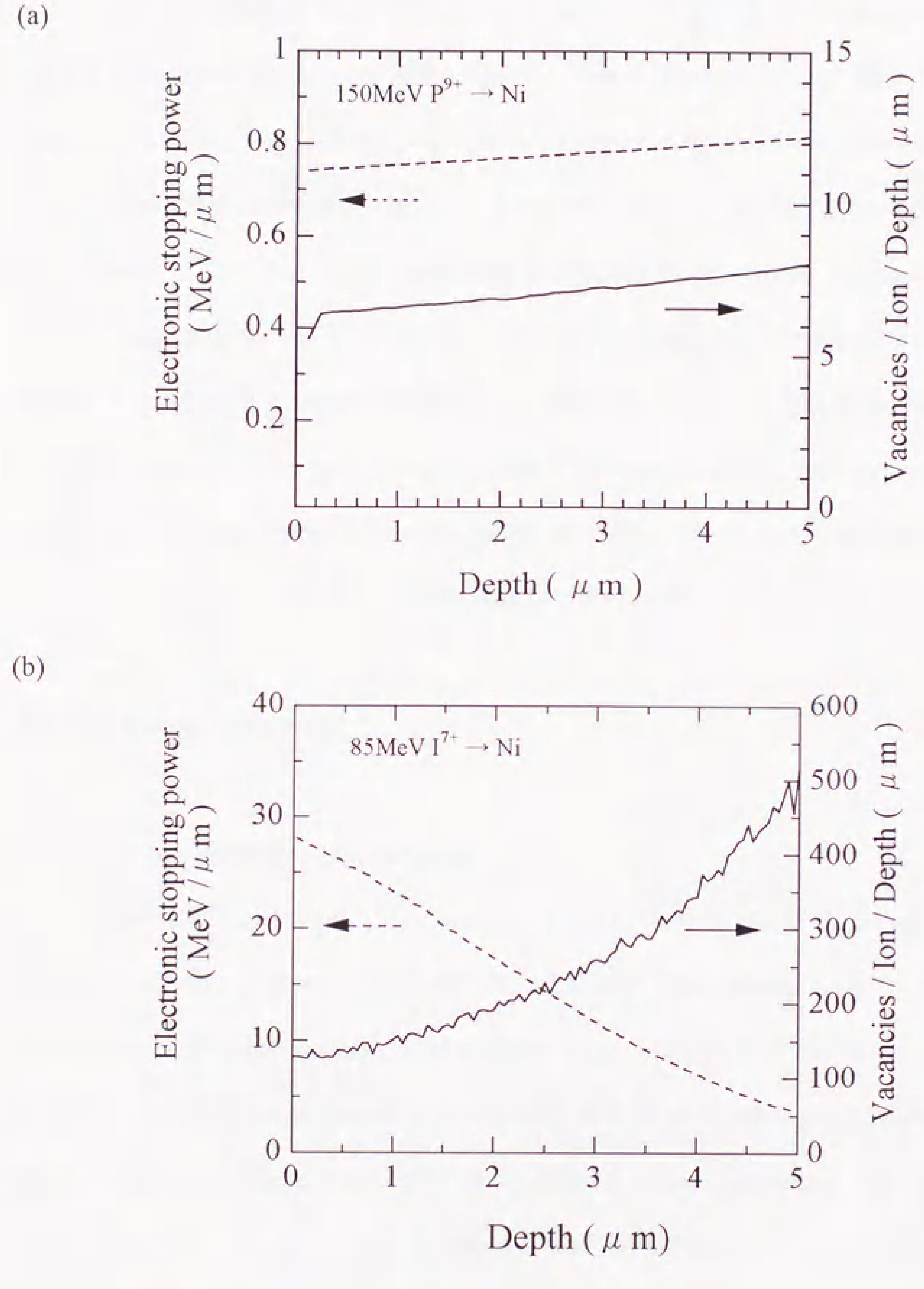

Fig. 4-1 The depth profile of both displacement damage and energy density of electron excitation (stopping power) for P-ion irradiation (a) and I-ion irradiation (b).

4.2.2 Measurements of DXS

The DXS experiments on irradiated samples were performed at room temperature with a four-circle diffractometer installed at Photon Factory of Institute of Materials Structure Science, High Energy Accelerator Research Organization in Tsukuba or at the Crystal Structure Analysis beamline in Super Photon ring – 8 GeV (Spring-8) with a wavelength of Cu Kα_1. The scattering intensities were always measured near the (111) reflection in the [111] direction. The diffuse scattering intensity was obtained by taking a difference between the intensity from an irradiated and that from a non-irradiated region of the same sample. The statistically reliable results were obtained using the high-flux synchrotron radiation by long-time (5-10 hr / scan) measurement. For example, approximately >600,000 counts were required at each point.

4.3 Results and discussion

4.3.1 150MeV phosphorus irradiation

Figures 4-2 to 4-4 show the intensity of DXS close to the (111) Bragg reflection in the [111] direction measured for Ni irradiated with phosphorus ions at room temperature. The intensity is the normalized value compared to that of the incident X-ray beam. Figure 4-5 shows the q-dependence of diffuse scattering intensities for $q > 0$. The q^{-4} dependencies are seen for all irradiation doses, indicating the presence of interstitial loops. It can be seen in Fig. 4-5 that the dose dependence of the scattering intensity became negligible small at around 10^{14}ions/cm^2. The intensity of Stokes-Wilson (q^{-4}) scattering is proportion to the concentration of defects, therefore, this result means that the amount of survived interstitials decreased at around 10^{14}ions/cm^2.

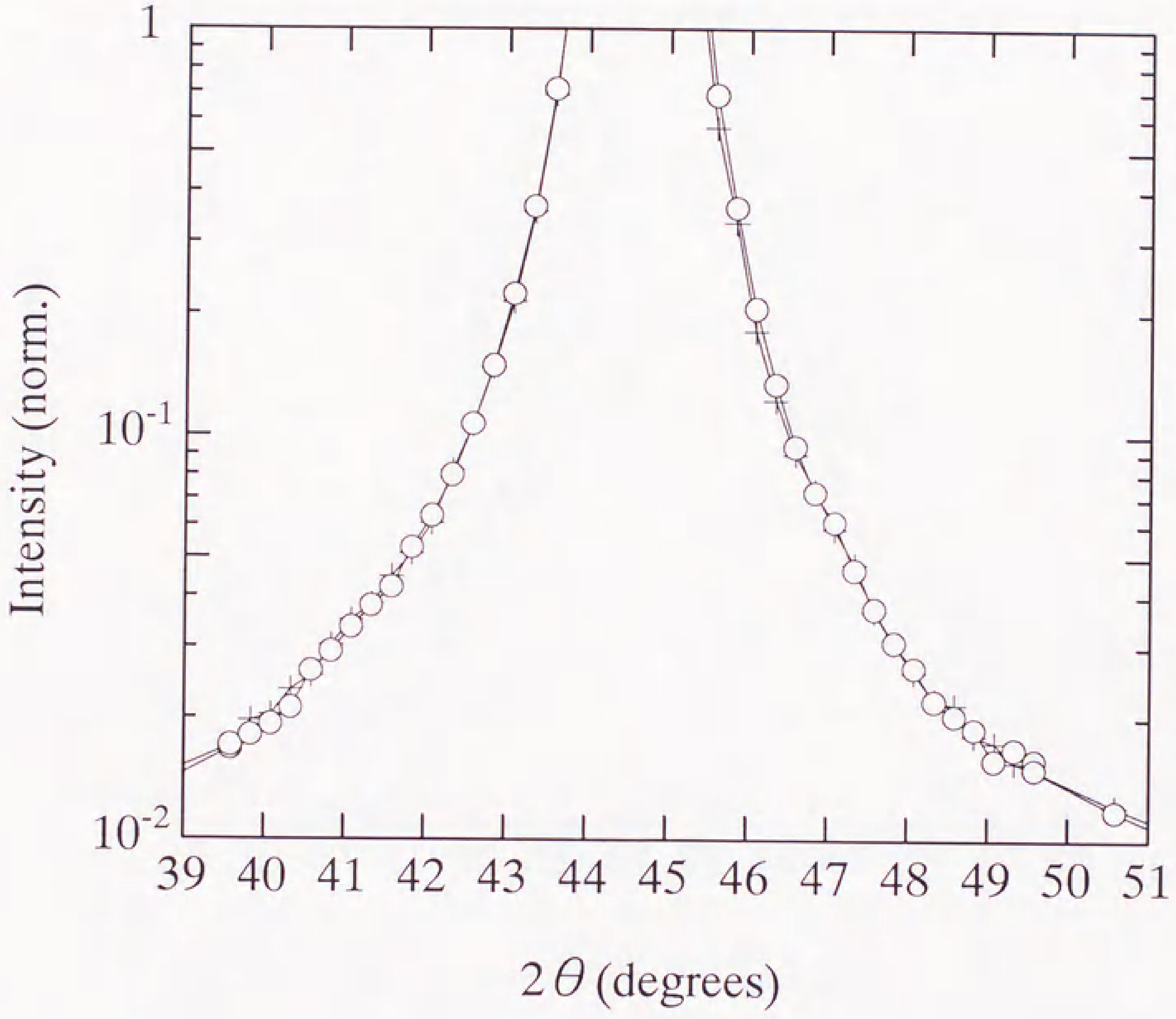

Fig.4-2 Intensity of X-ray scattering from pure Ni close to the (111) reflection in the [111] direction measured at room temperature.

○ : after irradiation (dose : 5.3×10^{13}ions/cm^2)
+ : before irradiation

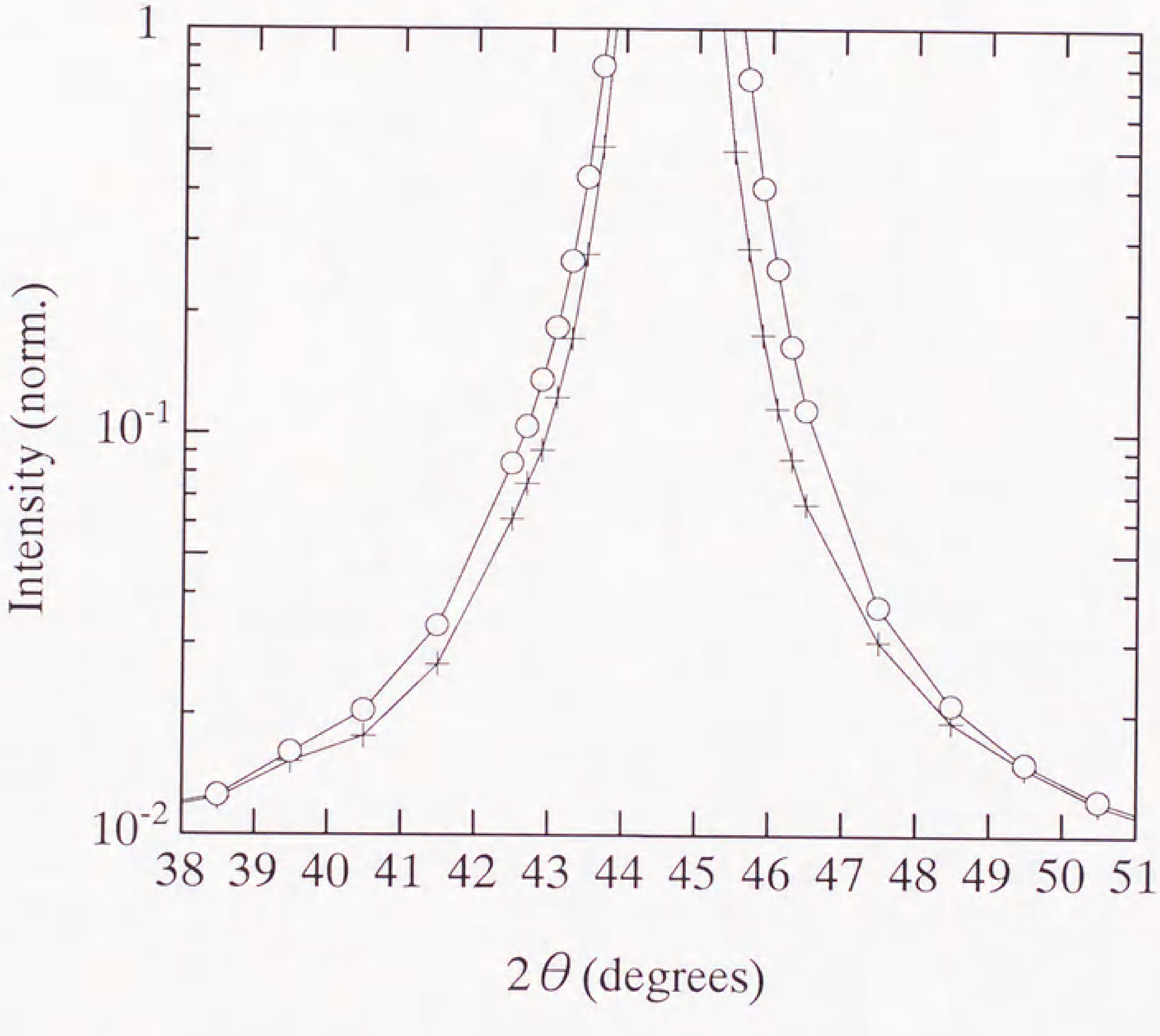

Fig.4-3 Intensity of X-ray scattering from pure Ni close to the (111) reflection in the [111] direction measured at room temperature.

○ : after irradiation(dose : 1.4×10^{14}ions/cm^2)
+ : before irradiation

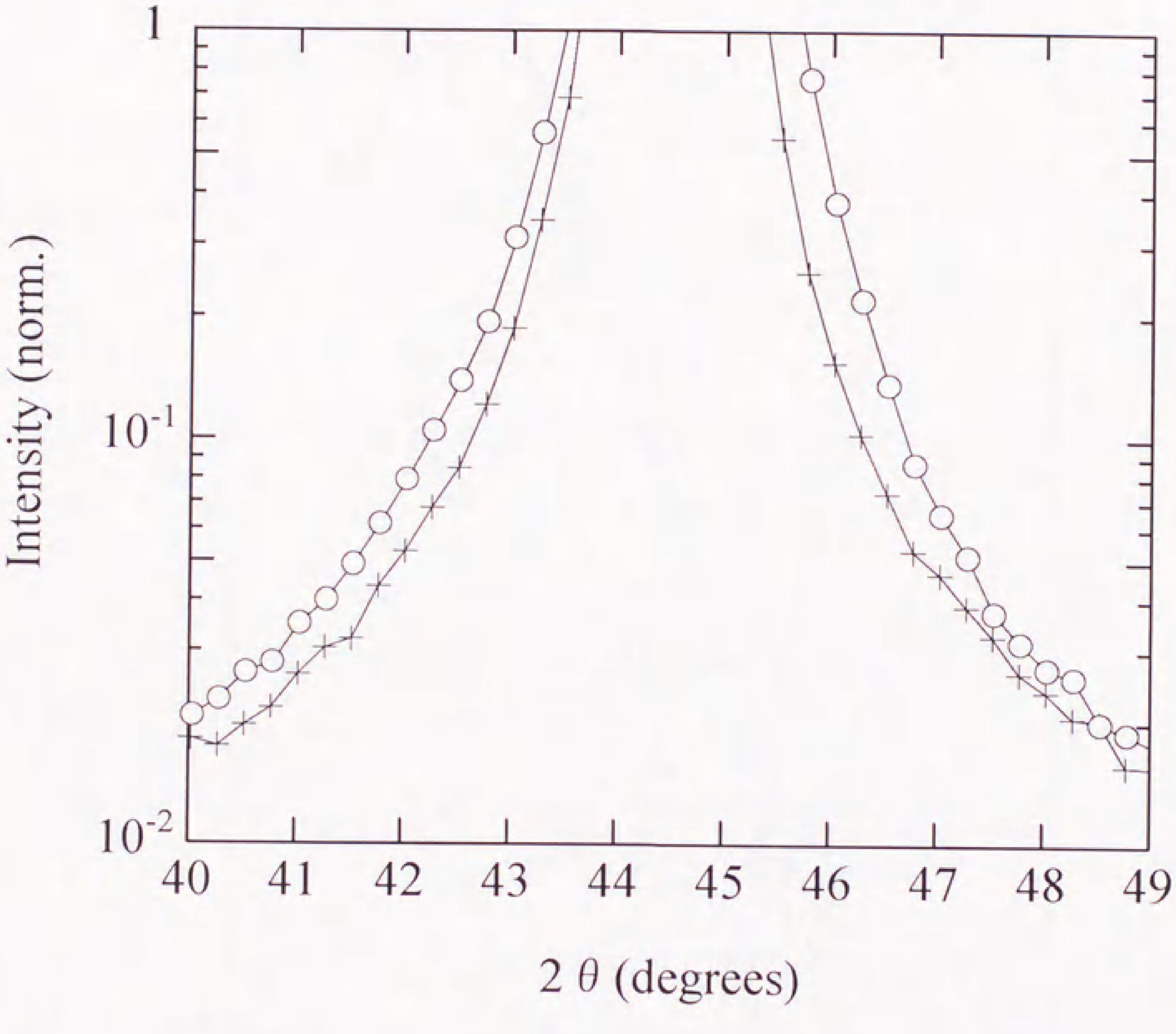

Fig.4-4 Intensity of X-ray scattering from pure Ni close to the (111) reflection in the [111] direction measured at room temperature.

○ : after irradiation(dose : 4.1×10^{14}ions/cm^2)
+ : before irradiation

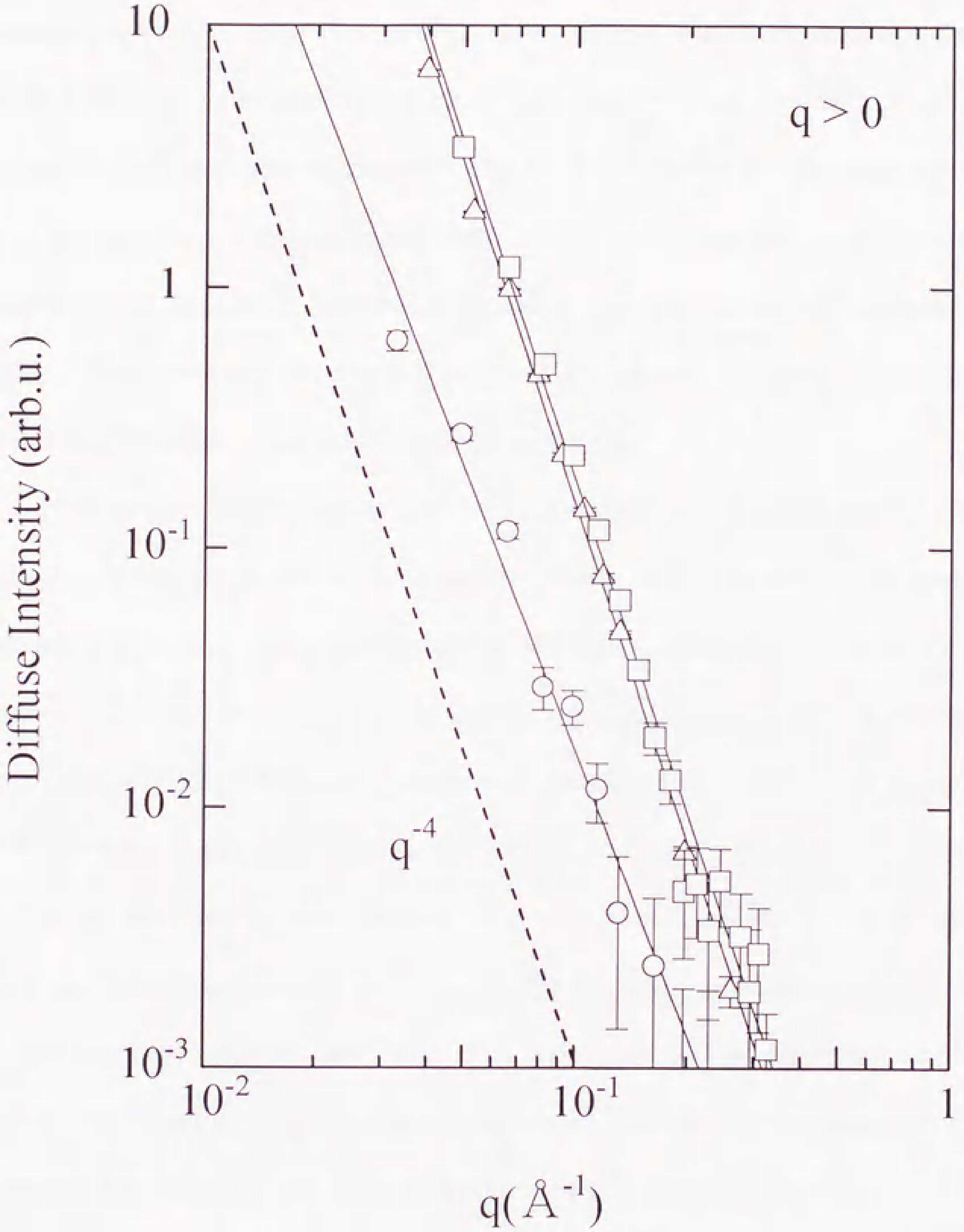

Fig.4-5 The q-dependence of diffuse scattering intensity in pure Ni (q > 0)

○ : irradiation dose 5.3×10^{13} ions / cm^2
△ : irradiation dose 1.6×10^{14} ions / cm^2
□ : irradiation dose 4.1×10^{14} ions / cm^2

Figure 4-6 shows the q-dependence of diffuse scattering intensities for $q < 0$. The q^{-3} dependencies are seen indicating the presence of small vacancy loops. These q^{-4} dependencies become clear by scaling these diffuse scattering intensities by q^{4}. Diffuse scattering intensities scaled by q^{4} for pure Ni irradiated with P-ions as a function of irradiation dose as shown in Fig.4-7. The increment of diffuse intensities due to the increase of the irradiation dose is seen, indicating the number density of defects survived until room temperature increases with the increase of irradiation dose at 30K. The asymmetry about $q = 0$ indicates the presence of the difference in loop size distribution between interstitial- and vacancy loops.

More detailed information on the defect structures (i.e. number density and size distribution of loops) can be obtained by fitting the theoretically calculated q-dependence of diffuse scattering intensity to the experimental data as reviewed in the literature [10]. For this purpose, the q-dependencies of scattering amplitudes from vacancy and interstitial dislocation loops were calculated as a function of loop radius. The lattice sums in Eqs.(2-10) and (2-11) were performed for Frank loops which were found to be predominant in irradiated *FCC* metals as observed by TEM, and the calculation of the displacement field was carried out using a formula reported by Ohr [11] and corrected later by Rao [12]. The q-dependencies of scattering amplitudes along the <111> reciprocal lattice vector calculated theoretically are shown in Fig.3-9 for both a single vacancy loop and a single interstitial loop with a loop radius $R = 10$, 30 and 50 Å in Ni as a typical example. For the fit of the data in the present study, the theoretical diffuse scattering intensities from vacancy loops and interstitial-loops were calculated as a function of loop radii of 5, 10, 20, 30, 40, 50 and 60 Å. The size distribution of the dislocation loops can be obtained by assuming the coexistence of the

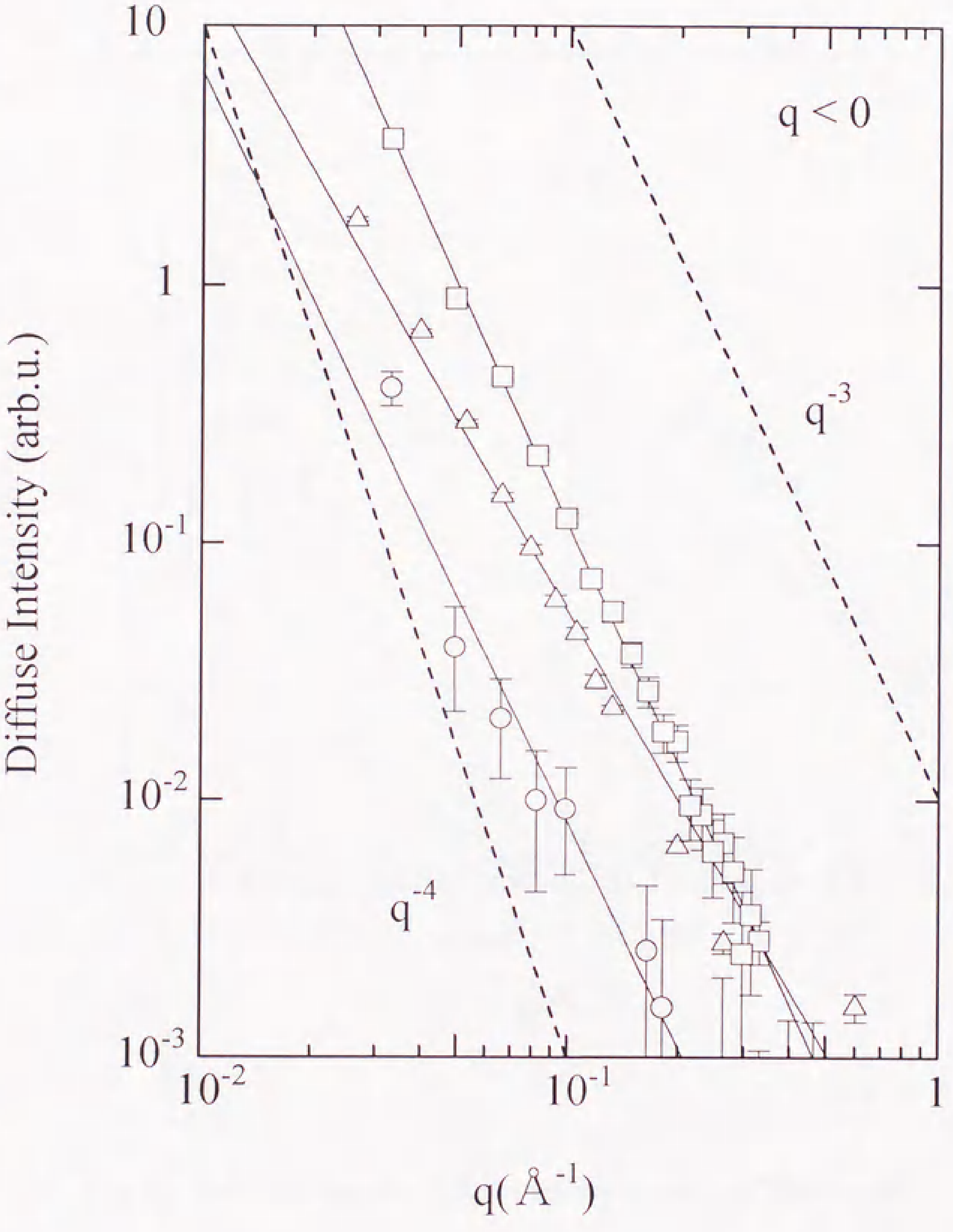

Fig.4-6 The q-dependence of diffuse scattering intensity in pure Ni ($q < 0$)

○ : irradiation dose: 5.3×10^{13} ions / cm^2
△ : irradiation dose: 1.6×10^{14} ions / cm^2
□ : irradiation dose: 4.1×10^{14} ions / cm^2

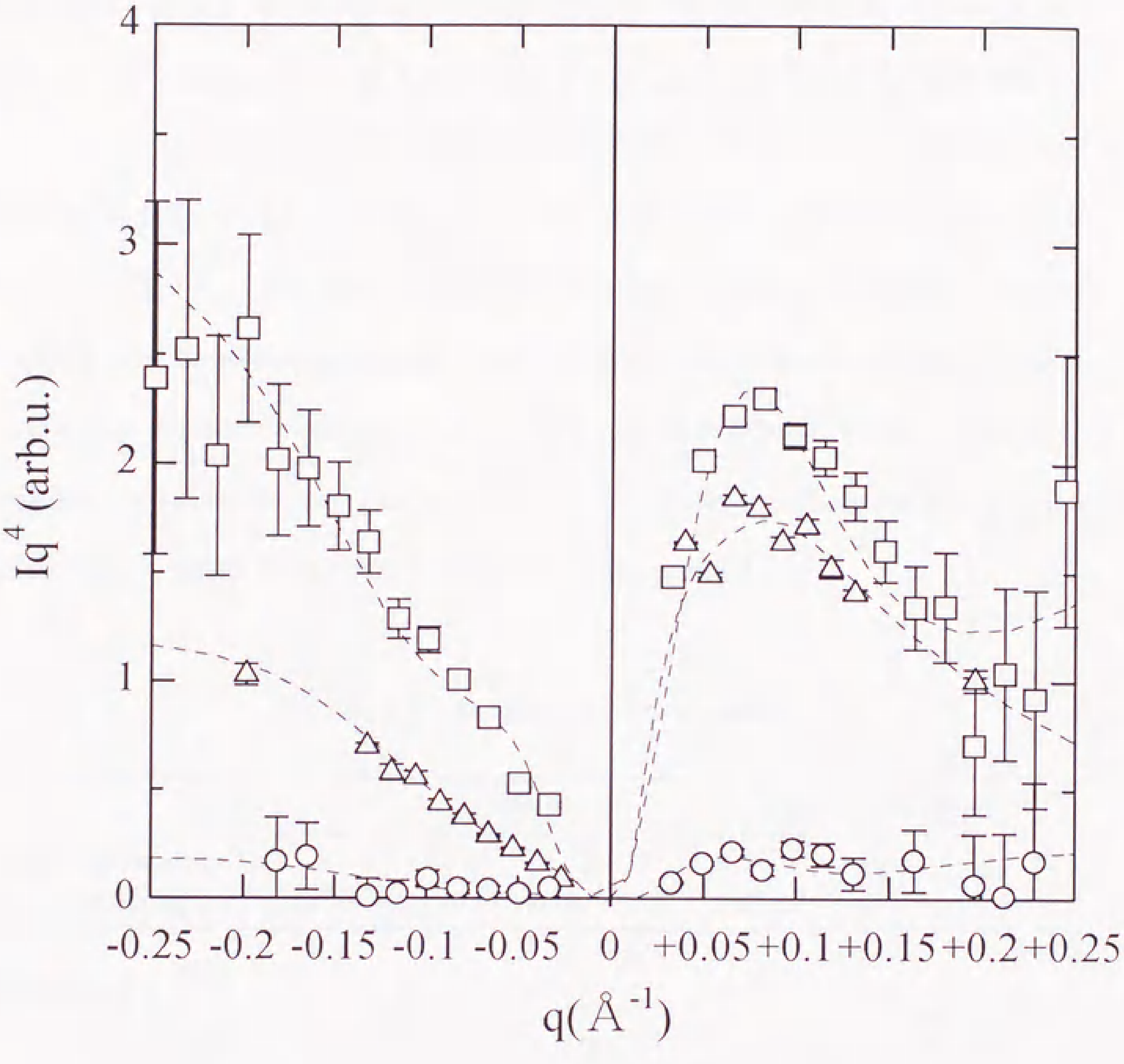

Fig.4-7 The defect-induced diffuse intensity scaled by q^4 for pure Ni.

○ : 5.3×10^{13} ions /cm^2
△ : 1.6×10^{14} ions /cm^2
□ : 4.1×10^{14} ions /cm^2
--- : the fitted curve for evaluating the size distribution of loops

several dislocation loops with different radii and fitting the calculated q-dependence to the experimental data. The results of a least-squares fitting, that are given by the dashed lines, are also shown in Fig.4-7 in comparison with the experimental data points. Table 4-1 summarizes the total number density of interstitial loops N_L^I and vacancy loops N_L^V, average loop radius $<R_L>$ and total number density of interstitial atoms N_I and vacancies N_V in the loops. The size distribution of the number density of loops in Ni is shown in Fig.4-8. The size distribution of vacancy loops is relatively narrow compared with that of interstitial loops, which is thought to be due to the small mobility of vacancies compared with interstitials. The size distributions for the number of interstitials or vacancies contained in loops with size R obtained from the fitting to the data for the irradiation three kinds of doses are shown in Fig.4-9.

Table 4-1 Summary of the results

irradiation species / dose (dpa)	*Vacancies*			*Interstitial atoms*		
	N_V (10^{18}cm^{-3})	$<R_L^V>$ (Å)	N_L^V (10^{17}cm^{-3})	N_I (10^{18}cm^{-3})	$<R_L^I>$ (Å)	N_L^I (10^{17}cm^{-3})
phosphorus						
5.3×10^{13}ions/cm^2 (4.1×10^{-5} dpa)	0.07	5.1	0.04	0.10	6.1	0.03
1.6×10^{14}ions/cm^2 (1.2×10^{-4} dpa)	0.44	5.3	0.26	0.88	11.6	0.08
4.1×10^{14}ions/cm^2 (3.2×10^{-4} dpa)	1.14	5.2	0.66	0.90	13.2	0.07
iodine						
1.9×10^{13}ions/cm^2 (5.2×10^{-4} dpa)	4.02	5.4	1.94	0.74	10.3	8.29

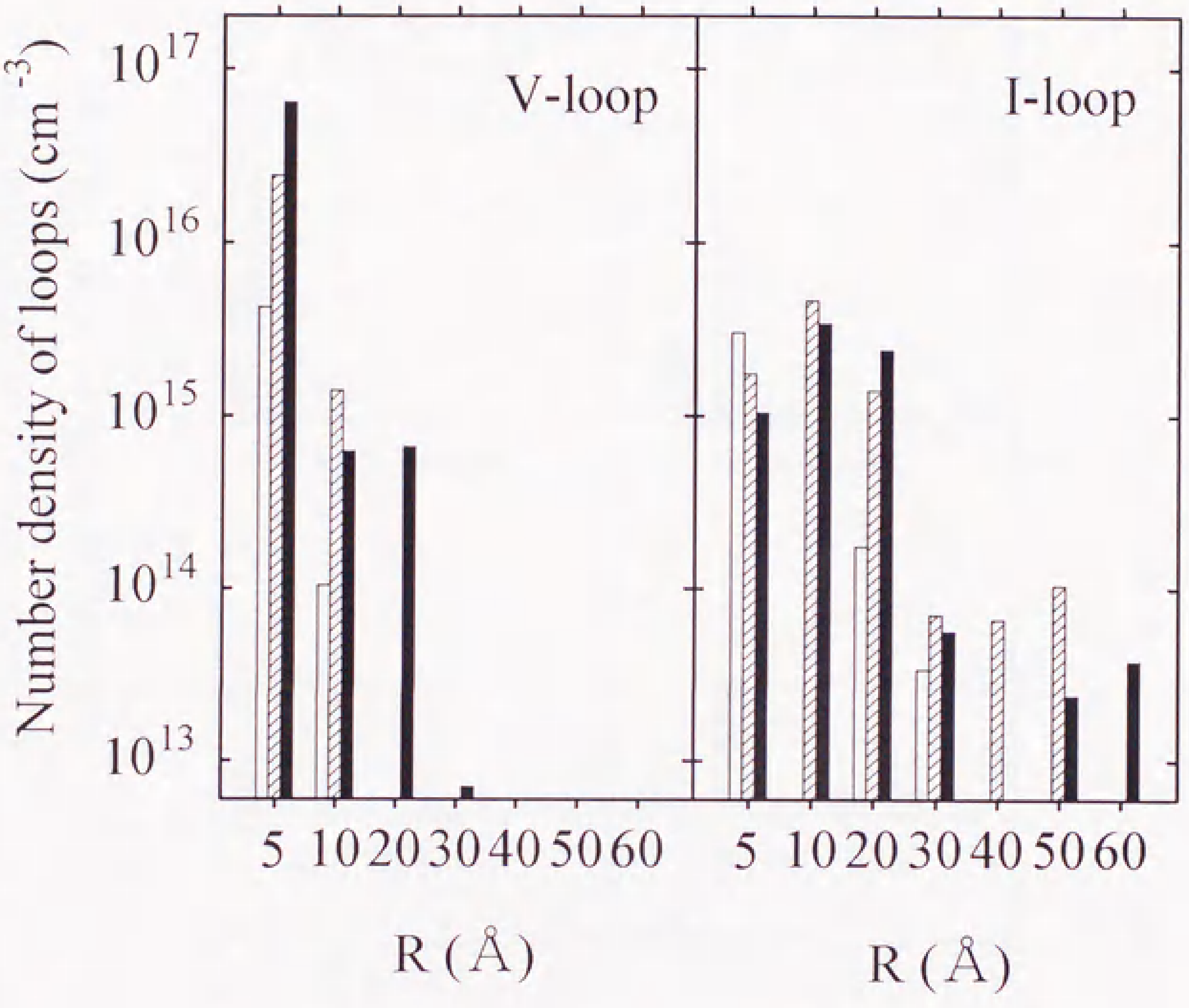

Fig.4-8 The size distribution of loops at room temperature in pure Ni irradiated with 150MeV phosphorus ions.

□ 5.3×10^{13}ions/cm^2

▨ 1.6×10^{14}ions/cm^2

■ 4.1×10^{14}ions/cm^2

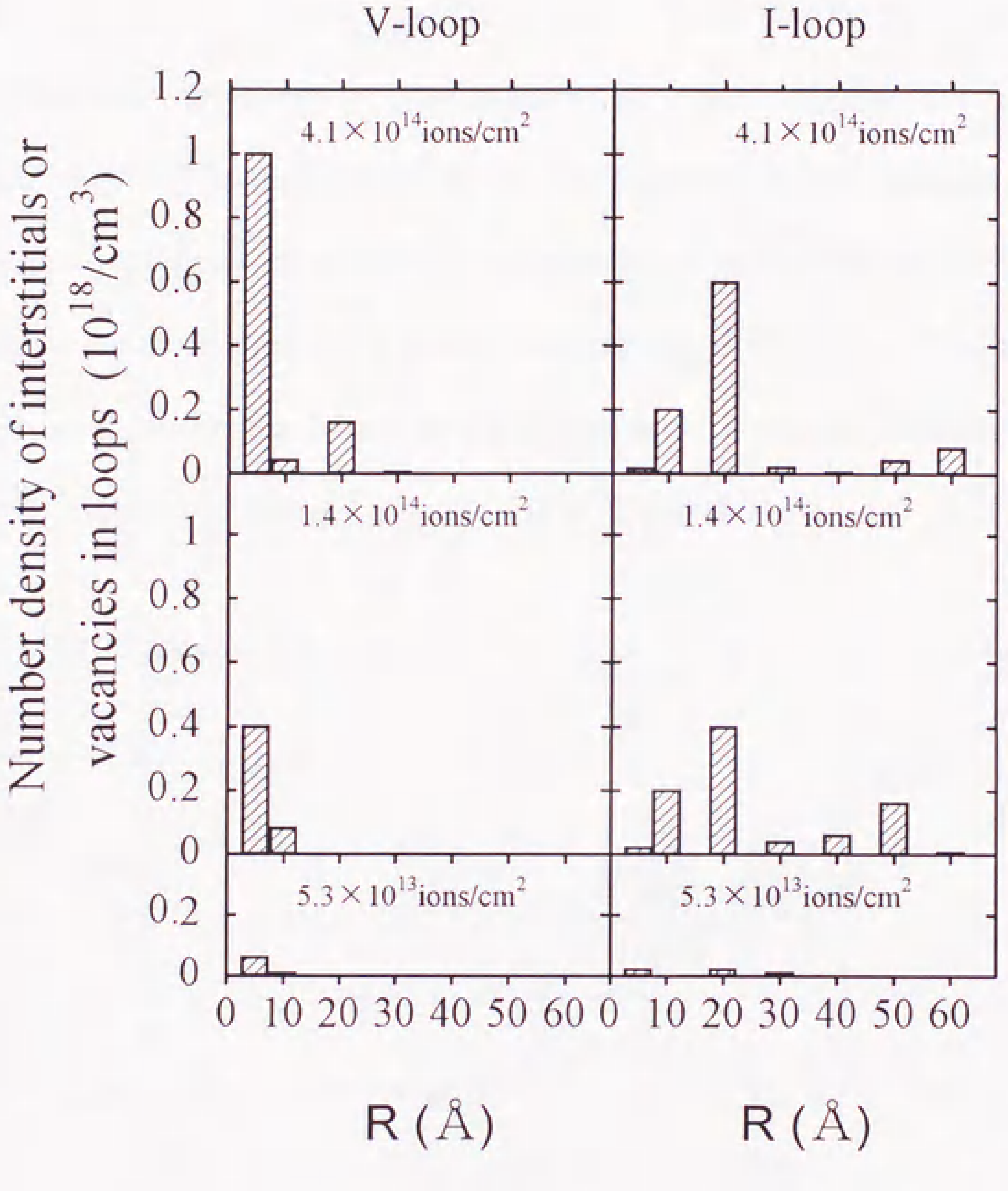

Fig.4-9 The number density of interstitials or vacancies in loops with a radius R for pure Ni irradiated with 150MeV phosphorus ions.

The result of electrical resistivity change for Ni irradiated with 120MeV chlorine at < 10K has been reported by Iwase [4-6]. Iwase showed that the radiation annealing by electron excitation occurred in Ni independently with the specimen thickness [13]. Therefore, the radiation annealing defects were also expected during in this high-energy P-ion irradiation experiment. Furthermore, they reported that the dependence of electrical resistivity on the irradiation dose was negligibly small at around 10^{14} ions/cm^2, indicating the presence of remarkable annihilation of interstitials at this dose. Figure 4-10 shows the dose dependence of the number density of defects in loops. Inspection of Fig.4-10 shows that numbers of interstitials and vacancies contained in loops are different. Since total number of vacancies in a perfect volume sample should be equal

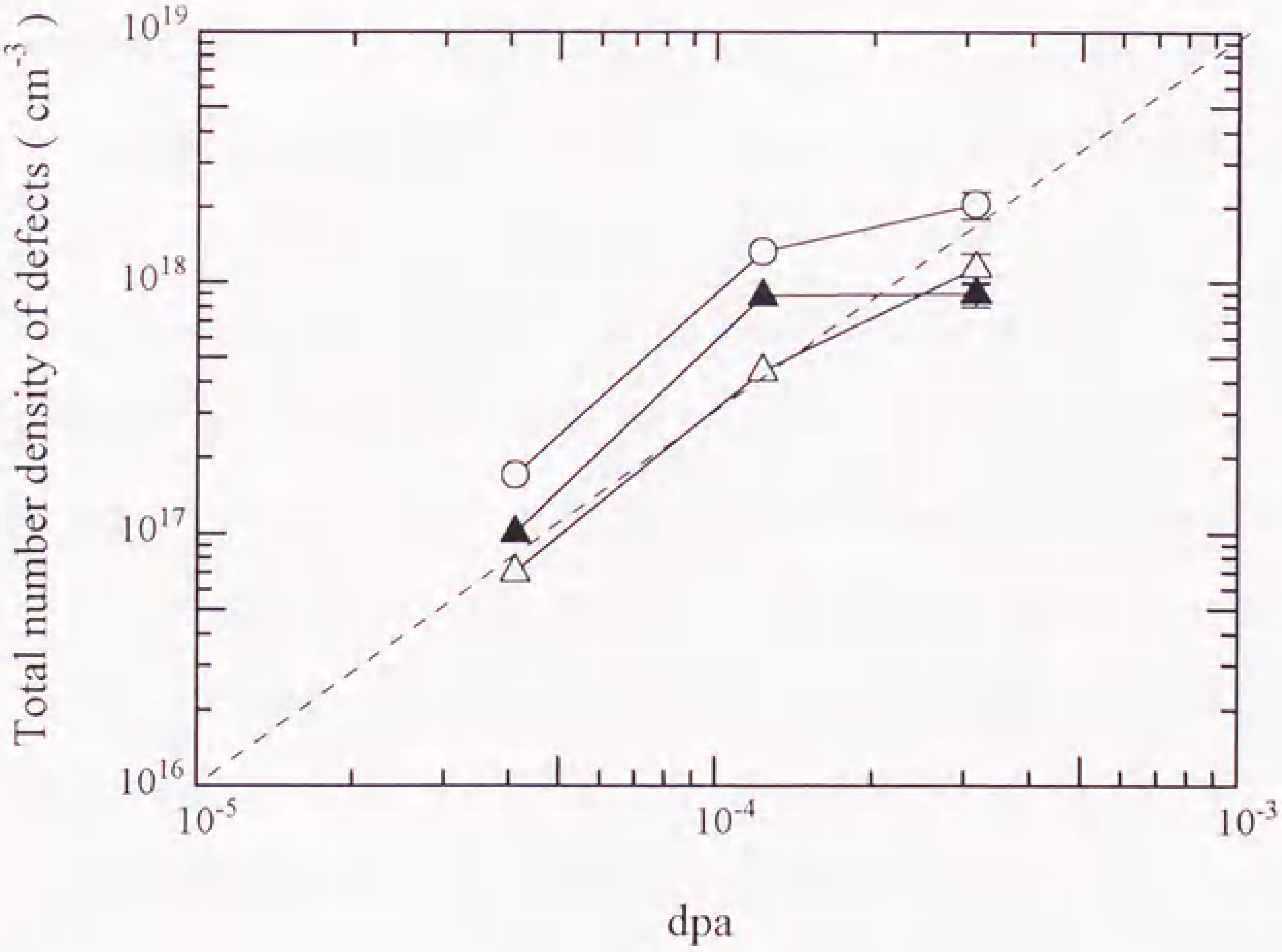

Fig.4-10 The dose (dpa) dependence of the number density of defects (vacancies and /or interstitials) in loops in 150MeV P-ion irradiated Ni.

○ : Total (Vacancies + Interstitials), △ : Vacancies, ▲ : Interstitials to that of interstitials, large numbers of interstitials compared with that of vacancies for the irradiation doses of 5.3×10^{13} and 1.4×10^{14}ions/cm^2 indicate that an small fraction of vacancies is not bound in observable loops [14]. However, for a irradiation dose of 4.1×10^{14}ions/cm^2, the number of interstitials becomes smaller than that of vacancies. Furthermore, the dose dependence of the number density of interstitials in interstitial loops on dose becomes negligibly small around 10^{14} ions/cm^2. This saturation type behavior exceeds the error in the loop counting method as shown by the error bars in this figure. Several possible mechanisms, such as the overlap of cascades or the enhanced radiation annealing, were considered to explain this experimental result. Figure 4-11 shows the dependence of the number density of vacancy loops in Ni on the irradiation dose for different ion irradiation. The data by I, Br, Cl irradiations were obtained by TEM [15]. The dependence of the number density of vacancy clusters on the mass of irradiation ions (I, Br, Cl) for the results with use of TEM is seen in this figure. In both case (DXS and TEM), the linear behavior (slope = 1) is seen, indicating that a vacancy loop is thought to be formed from an isolated cascade. For a low irradiation dose such as this study, the formation of vacancy loops with cascade overlap may not occur. Therefore, the overlapping of cascades was considered to be difficult to explain this result. The enhanced radiation annealing, on the other hand, was thought to explain this saturation type behavior of interstitials against the irradiation dose.

It seemed necessary to compare this result with that obtained by Ehrhart et al. for neutron-irradiated Ni [10]. They observed that the total number of interstitial atoms in neutron-irradiated Ni was 10% of the calculated number of displaced atoms. Resistivity recovery curve obtained by Horak et al. [16] following irradiation to similar

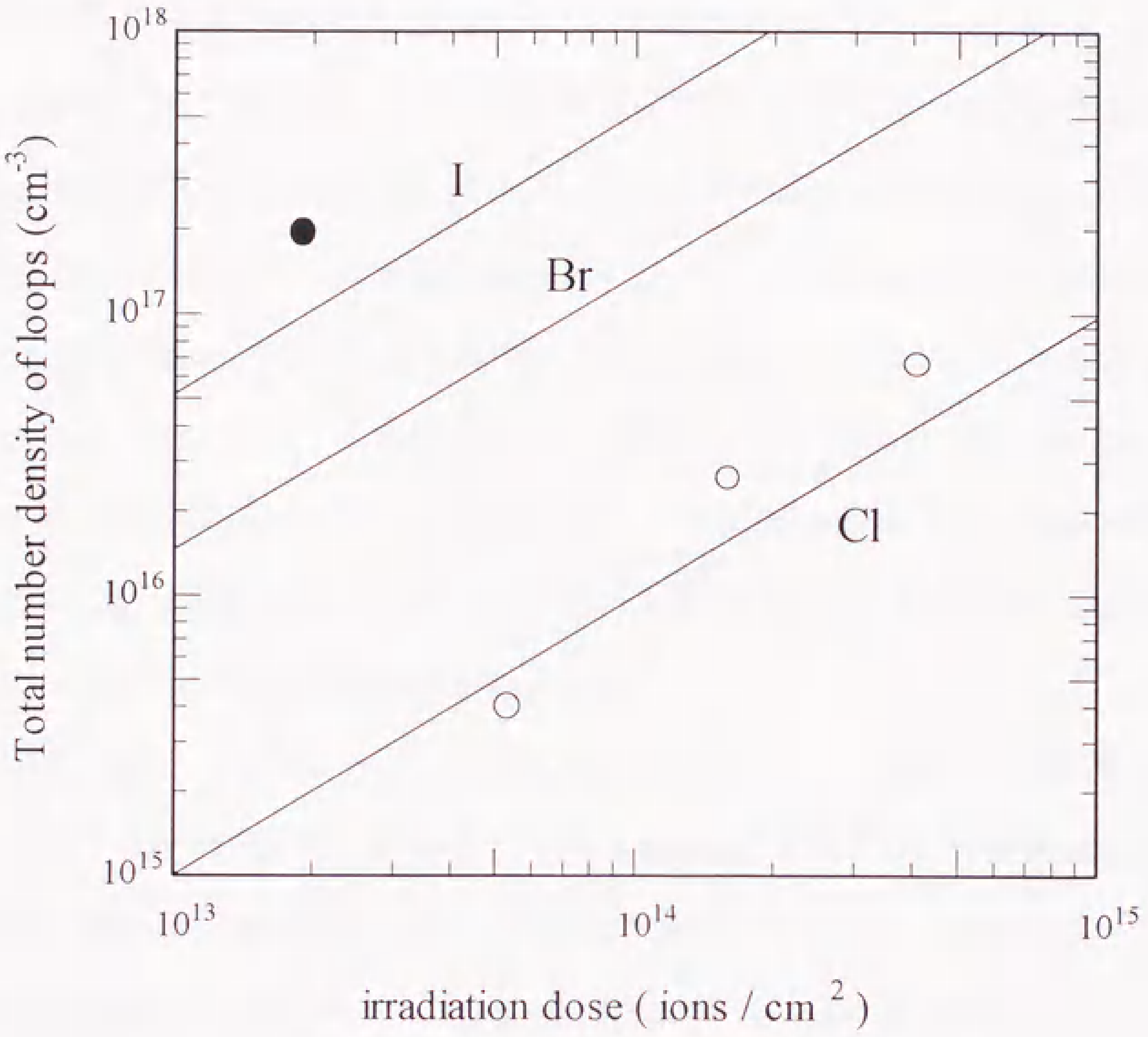

Fig.4-11 Dependence of the number density of vacancy-loop on P-ion irradiation dose together with the data by other researcher (I-, Br-, Cl-irradiations).

○ : P-ion irradiation, ● : I-ion irradiation (in this DXS study)

neutron doses indicate that 15% of the defects remain at 300K. Therefore, Ehrhart et al. concluded that one-third (~ half) of the initially created interstitials were lost during irradiation by spontaneous recombination. If the number of displaced atoms could be estimated by Trim code, the total number of interstitial atoms in Ni was about 3% of the calculated number of displaced atoms for this 150MeV phosphorus-ion irradiation. Resistivity recovery curve obtained by Iwase [14] following 120MeV chlorine irradiation to similar doses indicate that 40% of the defects remain at 300K. The amount of the resulting defects obtained by electrical resistivity measurement for P-ion irradiation at 300K was expected to be the same as that for Cl-ion irradiation, although there is a small difference of the irradiation condition between 150MeV P-ions and 120MeV Cl-ions (i.e. mass and energy of ions). We could conclude that 92.5% of the initially created interstitials were lost during irradiation by radiation annealing for a irradiation dose of 4.1×10^{14}ions/cm^2. This result indicates that the damage efficiency is about 0.075. The recombination probability within the mother cascade for high-energy ion-irradiation was larger than that for neutron-irradiation, indicating the presence of the enhanced radiation annealing.

The defect formation cross-section determined for a irradiation dose of 4.1×10^{14}ions/cm^2 was about 6×10^{-20}cm^2. Fig.1-3 showed that PKA median energy of 1.32MeV ^{14}N-ions was nearly equal to that of 120MeV Cl-ions. The PKA median energy of 150MeV P-ions for this study was expected to be similar to that of 120MeV Cl-ions. Therefore, the comparison of the damage efficiency between 1.32MeV ^{14}N-ions and 150MeV P-ions at the same PKA median energy became possible. Iwase et al. reported that the damage efficiency of 1.32MeV ^{14}N-ions was about 0.42 [17]. Thus, the damage efficiency for high-energy ion irradiation was one-fifth of that for low-energy ion-irradiation even at the same PKA median energy.

The differences in the defect structure between previous TEM study [15] (Fig.4-11) and this study are the presence of interstitial loops and the size of vacancy loops. The average size of vacancy loops observed by this DXS experiments (5Å) is nearly the visible limit of TEM, indicating the effect of the sample thickness. The specimens for TEM were irradiated after electropolishing into thin foil. In the case of thin foil irradiation, the evolution of defect structure is strongly affected by surrounding sinks for point defects [18]. In the present case of bulk specimen irradiation, on the other hand, the possibility that interstitials promptly escape from cascade and annihilate at surface sinks was thought to be low compared with the case of thin foil specimen. The average size of vacancy loops, in this mechanism, was thought to become small due to the recombination between interstitial atoms and cascades in this experiments.

4.3.2 85MeV iodine irradiation

The results of DXS experiment for 85MeV iodine irradiation are as follows : Figure 4-12 shows the intensity of DXS close to the (111) Bragg reflection in the [111] direction measured for Ni irradiated with iodine ions at room temperature. The intensity is the normalized value compared to that of the incident X-ray beam. Figure 4-13 shows the q-dependence of diffuse scattering intensities for $q > 0$. The q^{-4} dependencies are seen indicating the presence of interstitial loops. Figure 4-14 shows the q-dependence of diffuse scattering intensities for $q < 0$. These q^{-4} dependencies become clear by scaling these diffuse scattering intensities by q^4. Fig.4-15 shows the diffuse intensity scaled by q^4. The asymmetry about $q = 0$ indicates the presence of the difference in loop size distribution between interstitial- and vacancy-loops. The size distribution of the number density of loops in Ni is shown in Figs.4-16. The size distribution for the number of interstitials or vacancies contained in loops with size R obtained from the fitting to the data is shown in Figs.4-17. The number density of defects, especially for vacancies in vacancy loops, is very large compared to that for P-ion irradiation. The data point for I-ion irradiation is also plotted in Fig.4-11. The data points for I-ion irradiation positioned higher than that of TEM compared with the

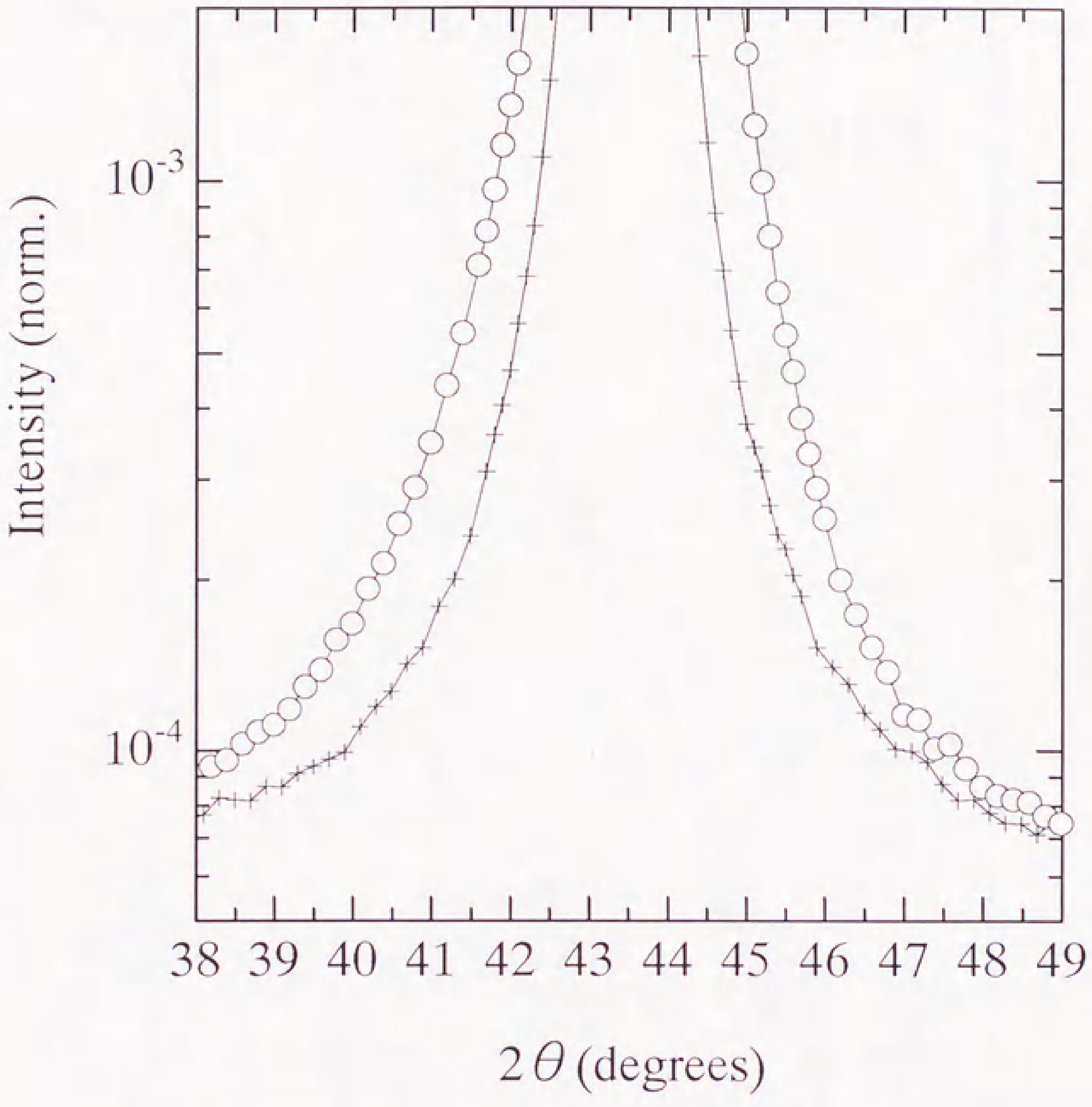

Fig.4-12 Intensity of X-ray scattering from Ni close to the (111) reflection in the [111] direction measured at room temperature.

○ : after irradiation (dose : 1.9×10^{13}ions/cm^2)
+ : before irradiation

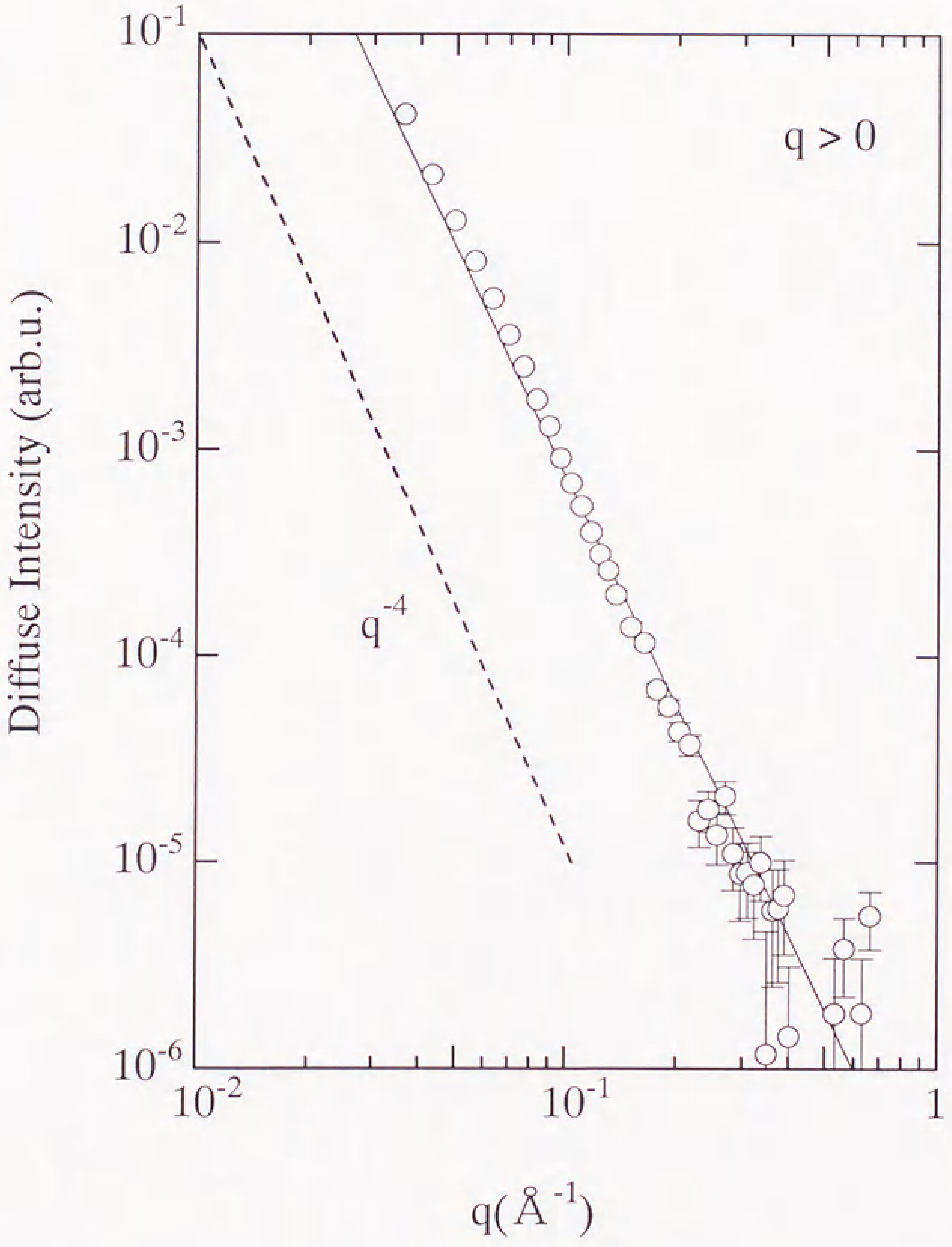

Fig.4-13 The q-dependence of diffuse scattering intensity in Ni (q > 0).
(irradiation dose : 1.9×10^{14} ions / cm^2)

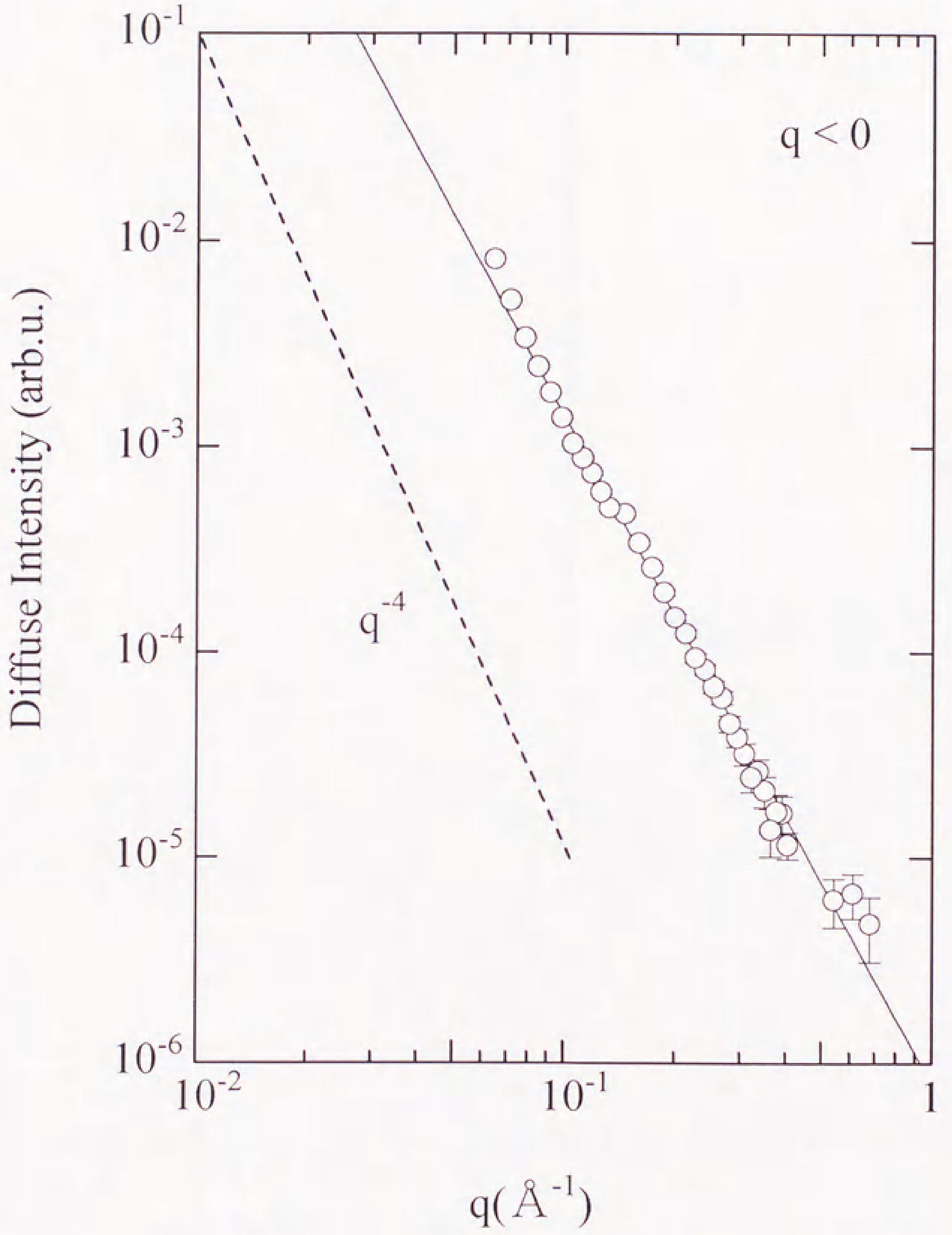

Fig4-14 The q-dependence of diffuse scattering intensity in Ni (q < 0).

(irradiation dose : 1.9 × 10^{14} ions / cm^2)

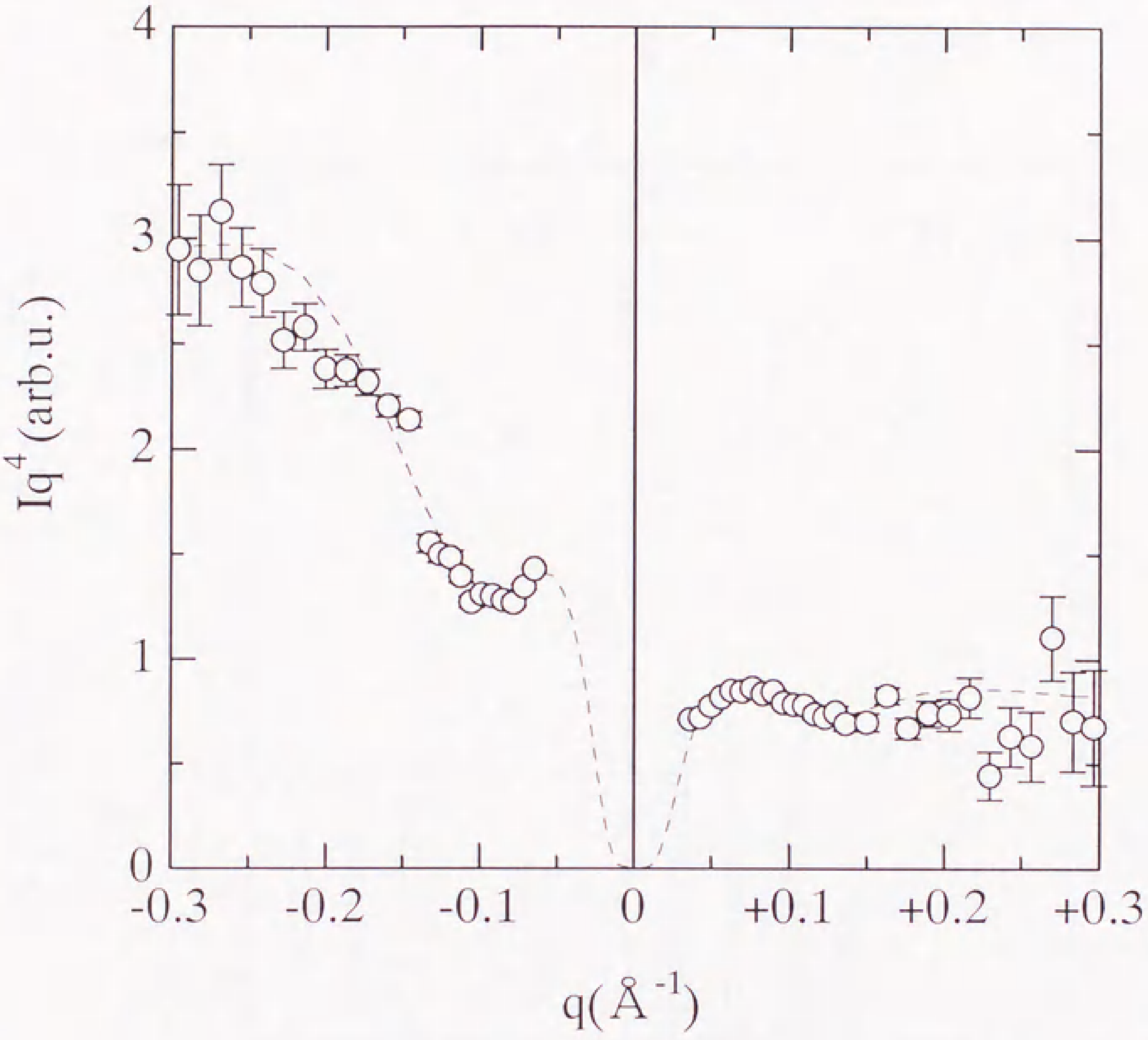

Fig.4-15 Diffuse scattering intensity scaled by q^4 obtained from Ni with dashed line fitted to the data.

○ : 1.9×10^{13} ions / cm^2
--- : fitted curve

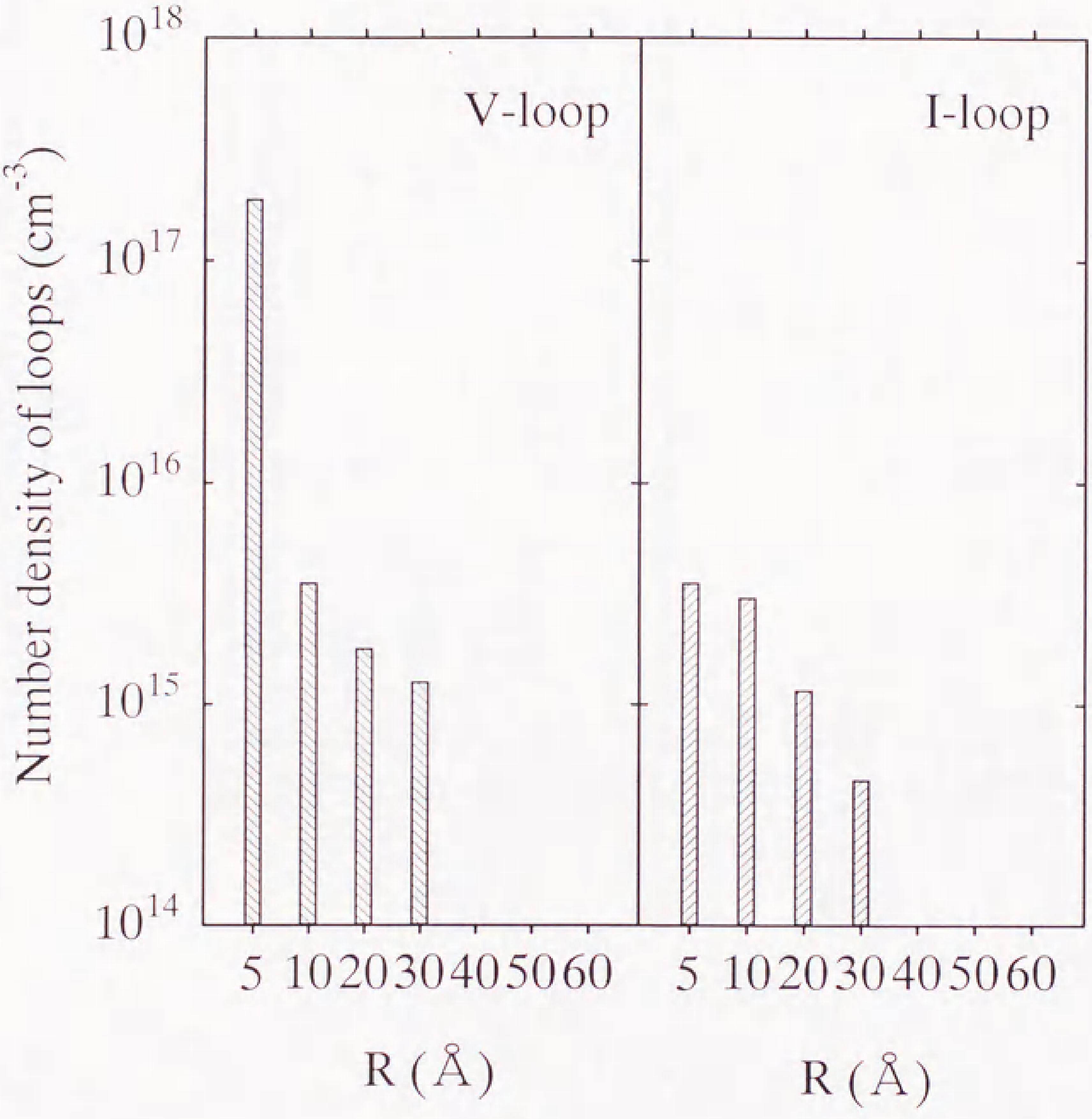

Fig.4-16 Distribution of the number density of loops with radius R for the irradiation dose of 1.9×10^{13} ions / cm^2.

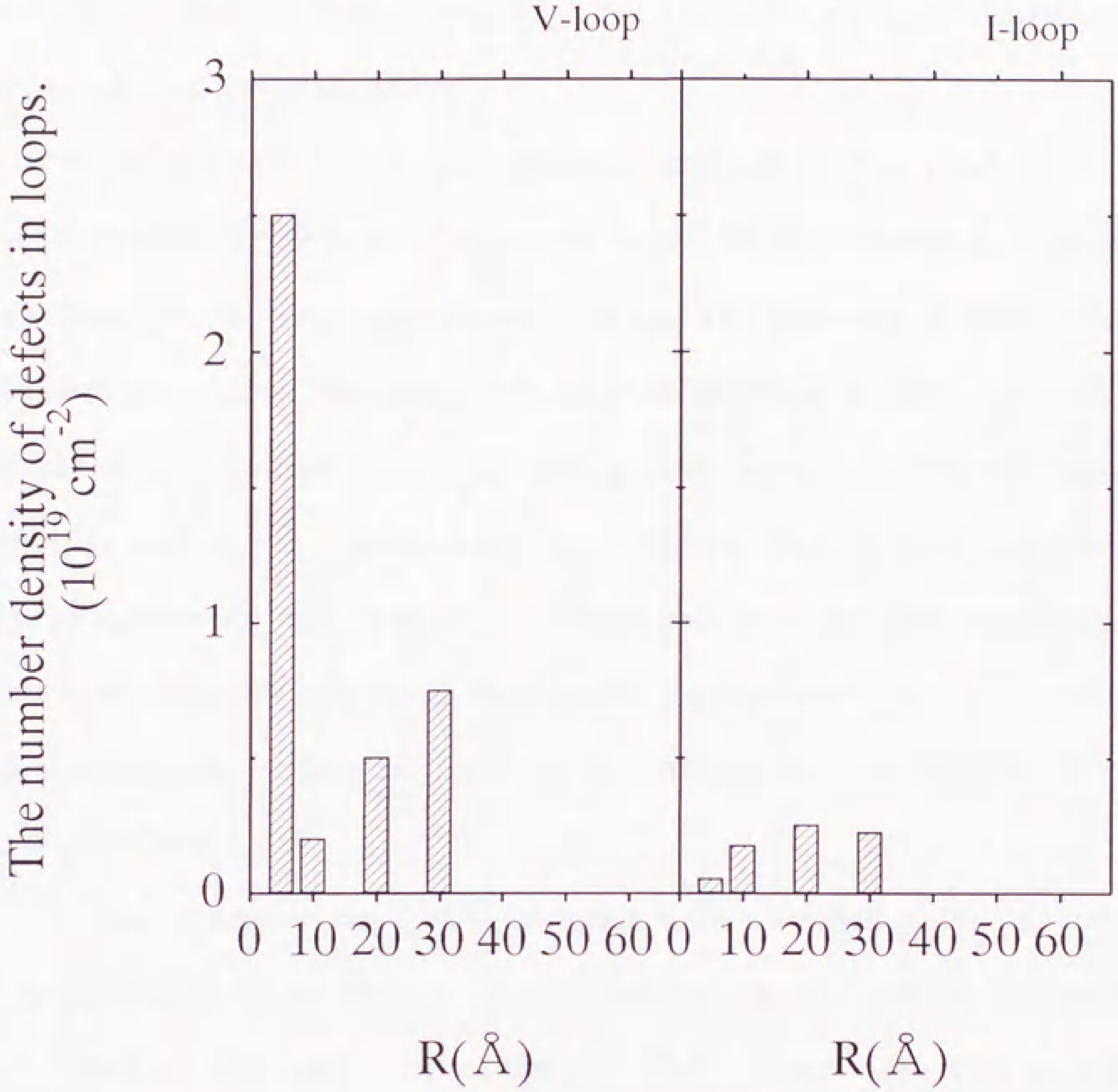

Fig.4-17 The size distribution of interstitials or vacancies in loops with a radius R for I-ion irradiation (dose of 1.9×10^{13} ions/cm^2)

case of P-ion irradiation. This difference is explained by that the depth dependence of vacancies introduced by I-ions as seen in Fig.4-1. That is, the region investigated for TEM was restricted at near the surface.

If the number of displaced atoms could be estimated by Trim code, the total number of interstitial atoms in Ni was about 1.6% of the calculated number of displaced atoms. Resistivity recovery curve obtained by Iwase [14] following 100MeV iodine irradiation to similar doses indicate that 50% of the defects remain at 300K. Therefore, we could conclude that about 97% of the initially created interstitials were lost during 85MeV I-ion irradiation by radiation annealing. The recombination probability within the mother cascade for high-energy ion-irradiation was larger than that for neutron-irradiation, indicating the presence of the enhanced radiation annealing. The amount of radiation annealing for I-ion irradiation (97%) was large compared with that for P-ion irradiation (93%).

The defect formation cross-section determined for a irradiation dose of 1.9×10^{13}ions/cm^2 was about 8×10^{-19}cm^2. Fig.1-3 showed that PKA median energy of 1.8MeV ^{40}Ar-ions was nearly equal to that of 100MeV I-ions. The PKA median energy of 85MeV I-ions for this study was expected to be similar to that of 100MeV I-ions. Therefore, the comparison of the damage efficiency between 1.8MeV ^{40}Ar-ions and 85MeV I-ions at the same PKA median energy became possible. Iwase et al. reported that the damage efficiency of 1.8MeV ^{40}Ar-ions was about 0.34 [17]. Thus, the damage efficiency for high-energy ion irradiation was about one-tenth of that for low-energy ion-irradiation even at the same PKA median energy. The results for P- and I-ion irradiation are summarized in Table 4-2.

Iwase et al. investigated the effect of the radiation annealing on stage I recovery

Table 4-2 Summary of experimental and calculated results

Ion	E (MeV)	σ_d^{exp} (cm^2)	Fraction of the annihilation in (%)	$T_{1/2}$ (keV)	Ref.
N	1.32	8.82×10^{-21}	58	7.45	[17]
Ar	1.8	6.60×10^{-20}	66	28.9	[17]
neutron	> 0.1	-	33 - 50	-	[10]
Cl	150	1.1×10^{-21}	-	6.36	[15]
I	120	5.0×10^{-20}	-	34.4	[15]
P	150	6.0×10^{-20}	93	-	this study
I	85	8.0×10^{-19}	97	-	this study

and observed the difference in the degree of the annihilation among stage $I_A \sim I_E$ [19]. The result of the thermal annealing experiments indicates that during I-ion irradiation some configurations of defects were preferentially annihilated and the others were not, i.e. selective defect annihilation occurred during irradiation. They analyzed the results by using a new model describing the production and the selective annihilation for several types of defects in pure Ni. From this analysis, it was revealed that the defect annihilation corresponding to the stage I_{B+C} annealing occurred during the I-ion irradiation with cross section σ_1^I of $6.5\times10^{-12}cm^2$, the stage I_{D+E} defects were annihilated with a cross section σ_2^I of $1.4\times10^{-12}cm^2$ and stage II defects with a cross section σ_3^I of $2.2\times10^{-13}cm^2$. If the radiation-annealing experiments are performed by P-ion irradiation under the same condition as by I-ion irradiation, one can estimate the cross section of annihilation for P-ion irradiation. Firstly, the relation between $\Phi\cdot(\sigma_1^I+\sigma_2^I+\sigma_3^I)$ and the number density of defects annihilated during irradiation estimated by subtracting the number density of interstitials obtained by DXS experiments from that by TRIM. Here, Φ is the irradiation dose. From this procedure, one could a straight-line relation between them, i.e. from (0, 0) to ($\Phi\cdot(\sigma_1^I+\sigma_2^I+\sigma_3^I)$), the number density of interstitials annihilated). Next, one fit to this straight line using the annihilation cross section of each type defects for P-ion, σ_1^P, σ_2^P and σ_3^P, as a fitting parameter. The results of the fitting are shown in Fig.4-18. From this fitting., I obtained the radiation annealing cross-section σ_1^P of 2.0×10^{-13}cm^2, σ_2^P of 1.5×10^{-14}cm^2 and σ_3^P of 3.4×10^{-15}cm^2.

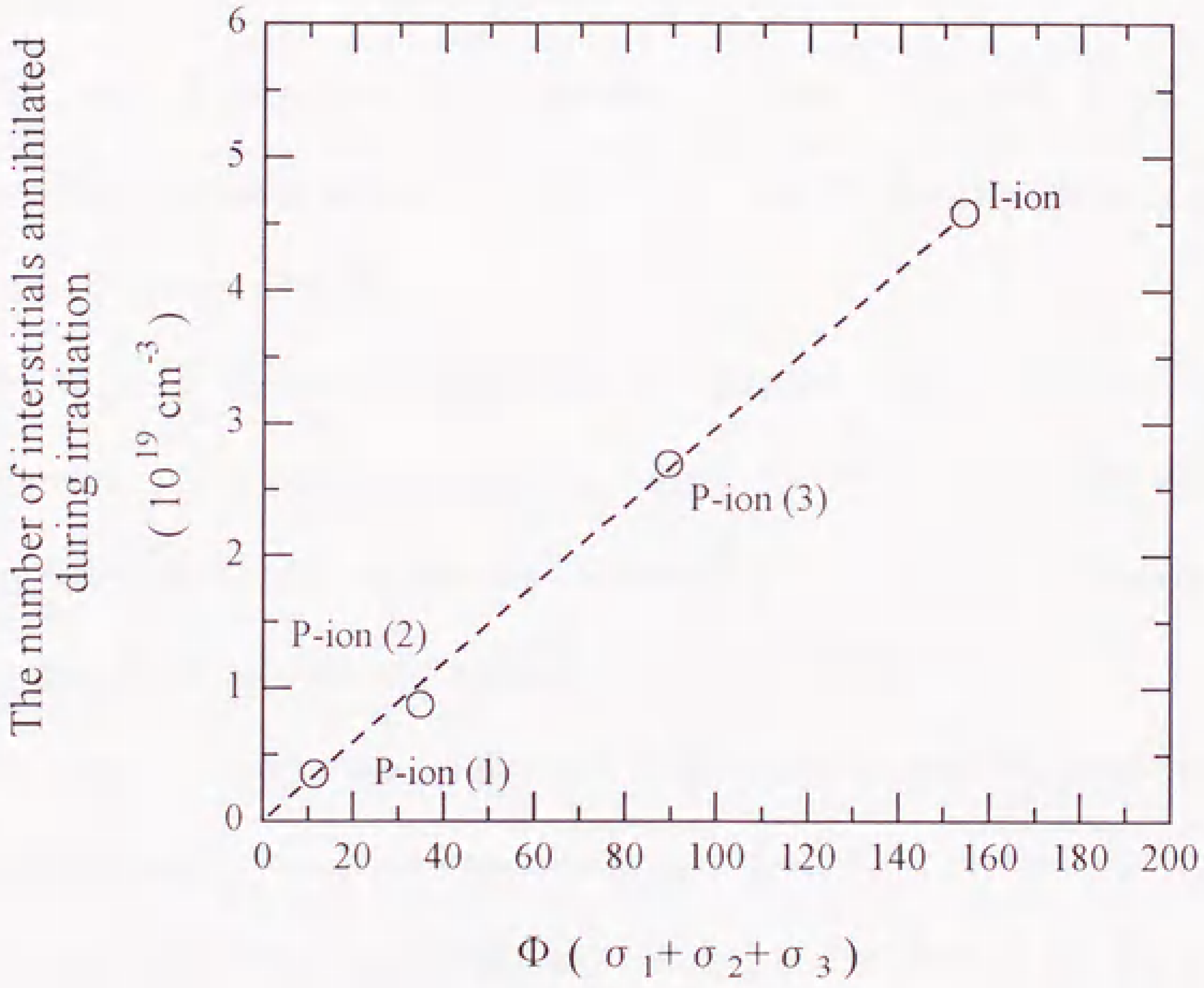

Fig. 4-18 The relation between the interstitials annihilated by P- and I-ions and the cross section of the annihilation scaled by dose.

P-ion (1) : 5.3×10^{13} ions / cm^2
P-ion (2) : 1.6×10^{14} ions / cm^2
P-ion (3) : 4.1×10^{14} ions / cm^2

4.4 Conclusions

The defect structures of pure Ni irradiated with 150MeV phosphorus ions at about 30 K and with 85MeV iodine at 50K were studied by diffuse X-ray scattering (DXS), and the following results were obtained.

(1) The dose dependence of the number density of interstitials in I-loops for P-ion irradiation became negligibly small at the irradiation dose where the radiation annealing occurred intensely.

(2) The dose dependence of the number density of vacancy loops for P-ion irradiation showed a linear behavior (slope = 1), indicating that a vacancy loop were formed from an isolated cascade.

(3) The ratio of interstitials annihilated in cascades to the calculated number of created interstitials for P-ion irradiation was large (about 93%) compared with that for low-energy ion-irradiations (or neutron irradiation). The damage efficiency of P-ion irradiation was about one-fifth of that for low-energy ion-irradiations.

(4) The ratio of interstitials annihilated in cascades to the calculated number of created interstitials for P-ion irradiation was large (about 97%) compared with that for low-energy ion-irradiations (or neutron irradiation). The damage efficiency of I-ion irradiation was about one-tenth of that for low-energy ion-irradiations.

(5) The annihilation cross-sections for each interstitial types in Ni under 150MeV P-ion irradiation were obtained using the data for 85MeV I-ions irradiation. The radiation annealing cross-sections obtained were σ_1^P of $2.0\times10^{-13}\mathrm{cm}^2$ (stage I_{B+C} interstitials), σ_2^P of $1.5\times10^{-14}\mathrm{cm}^2$ (stage I_{D+E}) and σ_3^P of $3.4\times10^{-15}\mathrm{cm}^2$ (stage II interstitials).

References

[1] R. S. Averback and K. L. Merkle, *Phys. Rev.* B**16**(1977)3860.

[2] R. S. Averback, L. J. Thompson and K. L. Merkle, *J. Nucl. Mater.* **69&70**(1978)714.

[3] R. S. Averback, R. Benedek, K. L. Merkle, J. Sprinkle and L. J. Thomson, *J. Nucl. Mater.* **75**(1978)162.

[4] A. Iwase, S. Sasaki and T. Iwata, *Phys. Rev. Lett.* **58**(1987)2450.

[5] A. Iwase and T. Iwata, *Nucl. Instr. and Moethds in Phys. Res.* B**90**(1994)322.

[6] A. Iwase, T. Iwata, T. Nihira and S. Sasaki, *Rad. Eff. and Deffects in Solids* **124**(1992)117.

[7] P. Ehrhart, *J. Nucl. Mat.* **216**(1994) 170.

[8] O. Bender and P. Ehrhart, *J. Phys. F : Met Phys.* **13**(1983)911.

[9] J. F. Ziegler, Computer Code TRIM92, IBM-Research, Yorktown, NY, 1992.

[10] P. Ehrhart and R. S. Averback, *Phil. Mag.* A**60**(1989)283.

[11] S.M.Ohr, *Phys. Status. Solidi* B**64**(1974)317.

[12] S.I.Rao, C.R.Houska, K.Grabowski, G.Ice and J.Sparks, *J. Appl. Phys.* **69**(1991)8104.

[13] A. Iwase, *JAERI-M* 92-124 (1992).

[14] R. Rauch, J. Peisl, A. Schmalzbauer and G. Wallner, *J. Phys.: Condens. Matter* **2**(1990)9009.

[15] S. Sasaki and A. Iwase, *Nucl. Instr. and Meth. in Phys. Res.* B**33**(1988)701.

[16] J. H. Horak and T. H. Blewitt, *J. Nucl. Mater.* **49**(1973/4)161.

[17] A. Iwase, S. Sasaki, T. Iwata and T. Nihira, *J. Nucl. Mater.* **141/143**(1986)786.

[18] S. Kojima, T. Yoshiie and M. Kiritani, *J. Nucl. Mater.* **155**(1988)1249.

[19] A. Iwase, *JAERI-M* 89-071 (1989).

5. Defect cluster in dilute Ni alloys irradiated with high-energy phosphorus ions

5.1 Introduction

In the previous chapter, the effect of radiation annealing on the resulting defect structure after the irradiation of 150MeV phosphorus ions was discussed. At low temperature (30～300K) the major reaction is originated from the migration of interstitials. The DXS is sensitive to this interstitial clustering process, therefore, the elucidation of the effect of solute atoms on the defect structures in dilute Ni alloys is also expected. Vacancies are, on the other hand, immobile at < 300K.

From the large number of TEM studies that have been performed on vacancy loop formation from displacement cascades, it has been shown that the formation of vacancy loops was dependent on irradiation parameter (ion mass, ion energy, irradiation temperature) and material parameters (structure, material, impurity concentration and type) [1-3]. The effect of impurity type and concentration was complicated with some impurities increasing and others decreasing the loop formation probability. The defect structures in dilute Ni alloys [4-6] has been also investigated by TEM. The observed results were interpreted in terms of the molten-zone model for vacancy loop formation, which is based on molecular dynamics computer simulation of low-energy displacement cascade [7-9]. The various solute effects (interruption of replacement collision sequences and focusons, and interstitial-solute binding) were applied to explain these results [5].

In this study, the DXS experiments for dilute Ni-Cu and dilute Ni-Fe alloys irradiated with high-energy P-ions were performed to investigate the role of the interaction between interstitials and solute atoms on radiation annealing.

5.2 Experimental

5.2.1 Samples and irradiation condition

High purity single-crystal samples of dilute Ni alloys (Ni-0.05at.%Fe and Ni-0.04at.%Cu) were spark-cut from large single crystals supplied by Johnson Mathey Chemicals Ltd (JMC). The large single crystals were grown by the Czochoralski method. The size of all samples was about 10×5×1 mm^3. The phase diagrams for both Ni-Cu and Ni-Fe alloys are shown in Figs.5-1 (a) and (b), respectively. As seen in these figures, these alloys form single phase solid solution and do not change the Ni structure (*FCC*). The irradiation with 150MeV phosphorus ions (P^{9+}) was performed up to two kinds of doses of 1.6×10^{14} and 4.1×10^{14} ions/cm^2 by the JAERI Tandem accelerator at 30K in a vacuum of 1×10^{-6} Torr. As seen in Fig.3-1, both the depth profile of both displacement damage (vacancies) and the energy density of electron-excitation in pure Ni were calculated with TRIM code under the usual

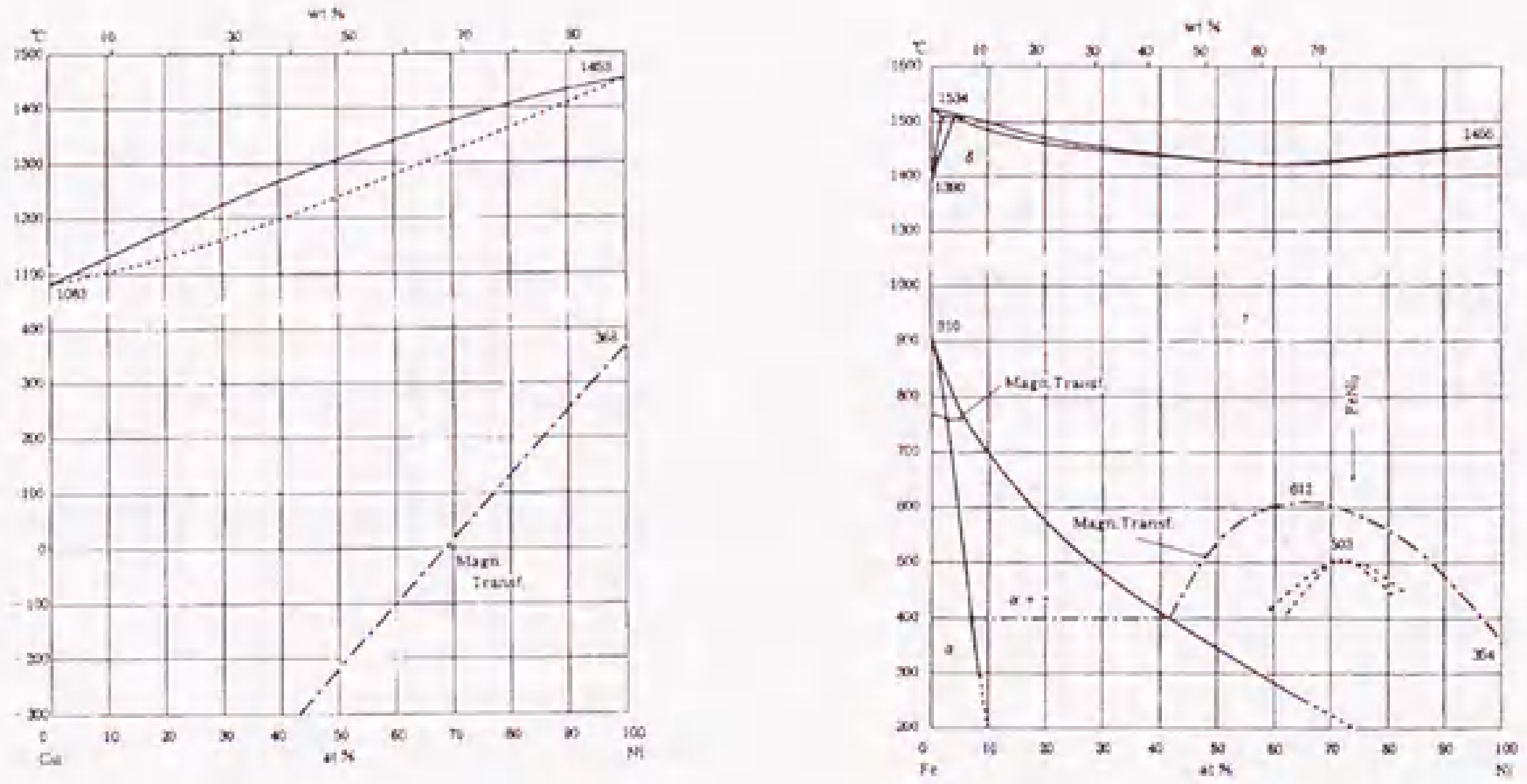

Fig.5-1 (a) phase diagram for Ni-Cu (b) phase diagram for Ni-Fe assumption of threshold energy of 33eV. This figure shows only surface region since the effective thickness for DXS study is 5μm. The projected range of phosphorus ions is 18μm the same as pure Ni, therefore, chemical effect of phosphorus on defect clustering is thought to be negligible. The stopping power along a P-ion path is so large (about 8MeV/μm) that the annihilation of defects is expected under irradiation at 30K.

5.2.2 Measurements of DXS

The DXS experiments on irradiated samples were performed at room temperature with a four-circle diffractometer at JAERI Tokai using a 18kW rotating X-ray anode with a wavelength of Cu Kα_1. The scattering intensities were always measured near the (111) reflection in the [111] direction. The diffuse scattering intensity was obtained by taking a difference between the intensity from an irradiated and that from a non-irradiated region of the same sample.

5.3 Results and discussion

Figures 5-2 to 5-5 show the intensity of DXS close to the (111) Bragg reflection in the [111] direction measured for dilute Ni alloys irradiated with phosphorus ions with use of a 18kW rotating anode at room temperature. Figures 5-6 to 5-7 show the q-dependence of diffuse scattering intensities for $q > 0$. The q^{-4} dependencies are seen indicating the presence of interstitial loops. Figures 5-8 and 5-9 shows the q-dependence of diffuse scattering intensities for $q < 0$. The q^{-3} dependencies are seen indicating the presence of small vacancy loops. Diffuse scattering intensities scaled by q^4 for all dilute alloys with the data for pure Ni irradiated with P-ions up to the same

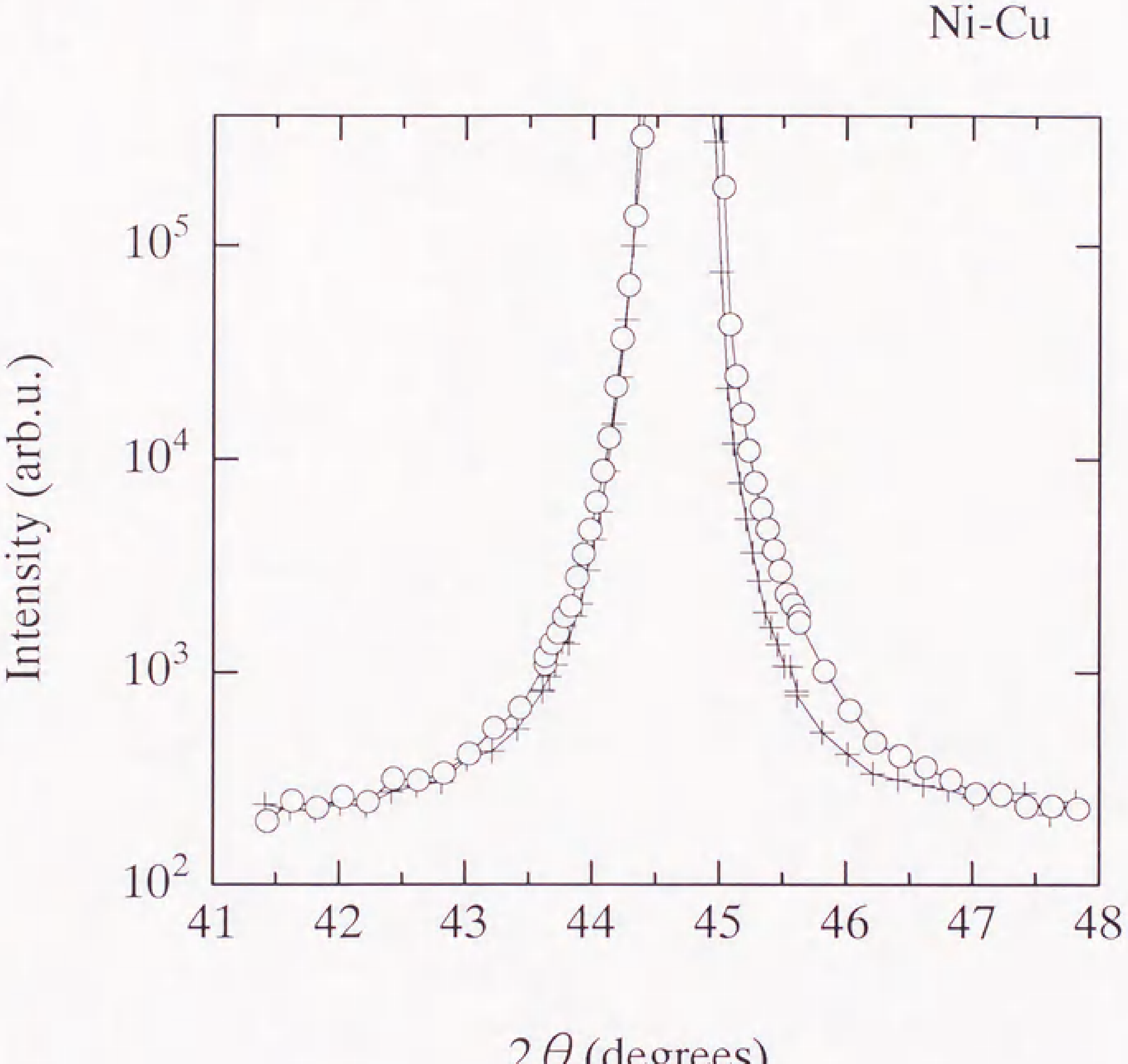

Fig.5-2 Intensity of X-ray scattering from Ni-Cu close to the (111) reflection in the [111] direction measured at room temperature.

○ : after irradiation (dose : 1.6×10^{14}ions/cm^2)
+ : before irradiation

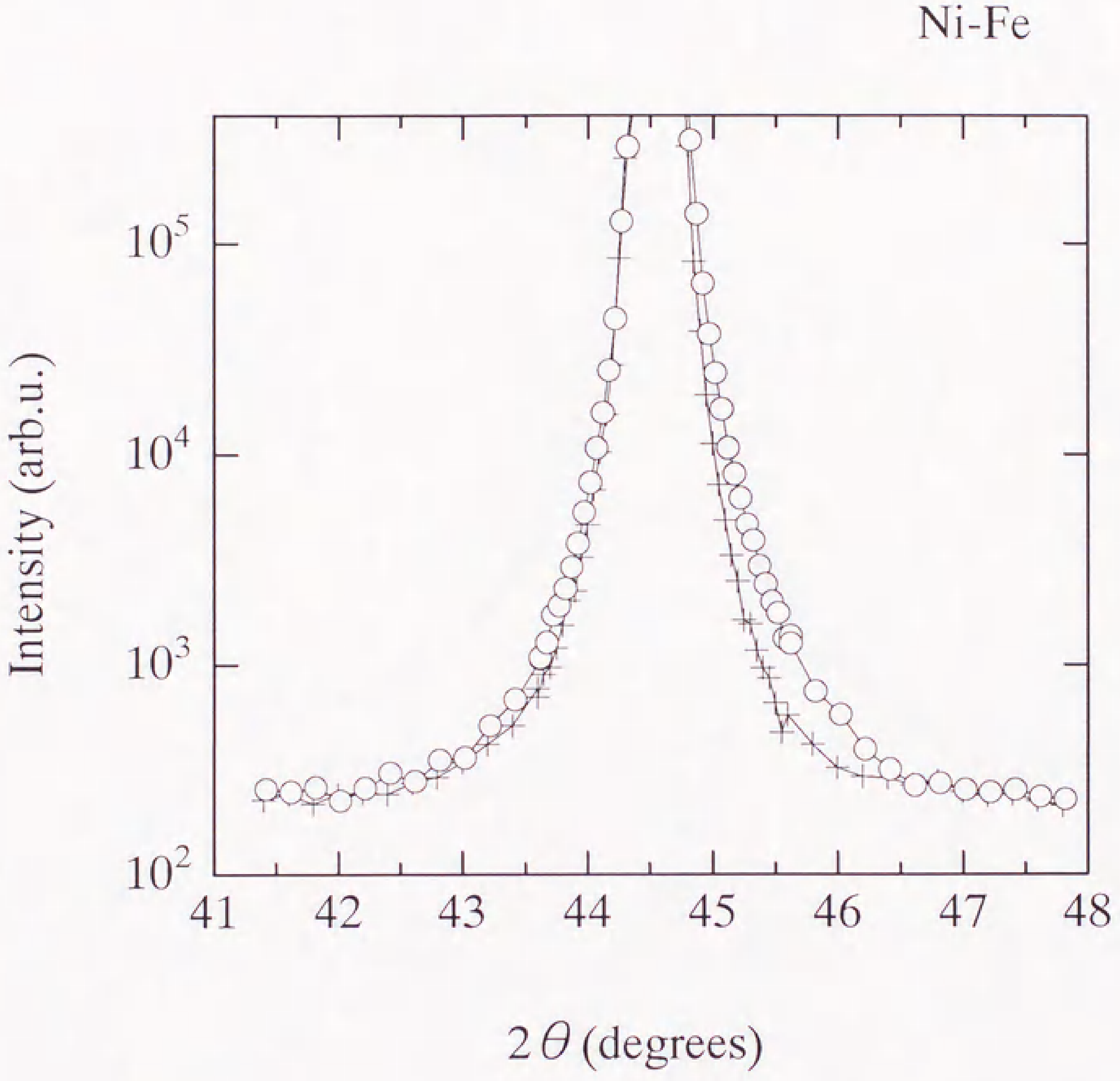

Fig.5-3 Intensity of X-ray scattering from Ni-Fe close to the (111) reflection in the [$\bar{1}$11] direction measured at room temperature.

○ : after irradiation (dose : 1.6×10^{14}ions/cm^2)
+ : before irradiation

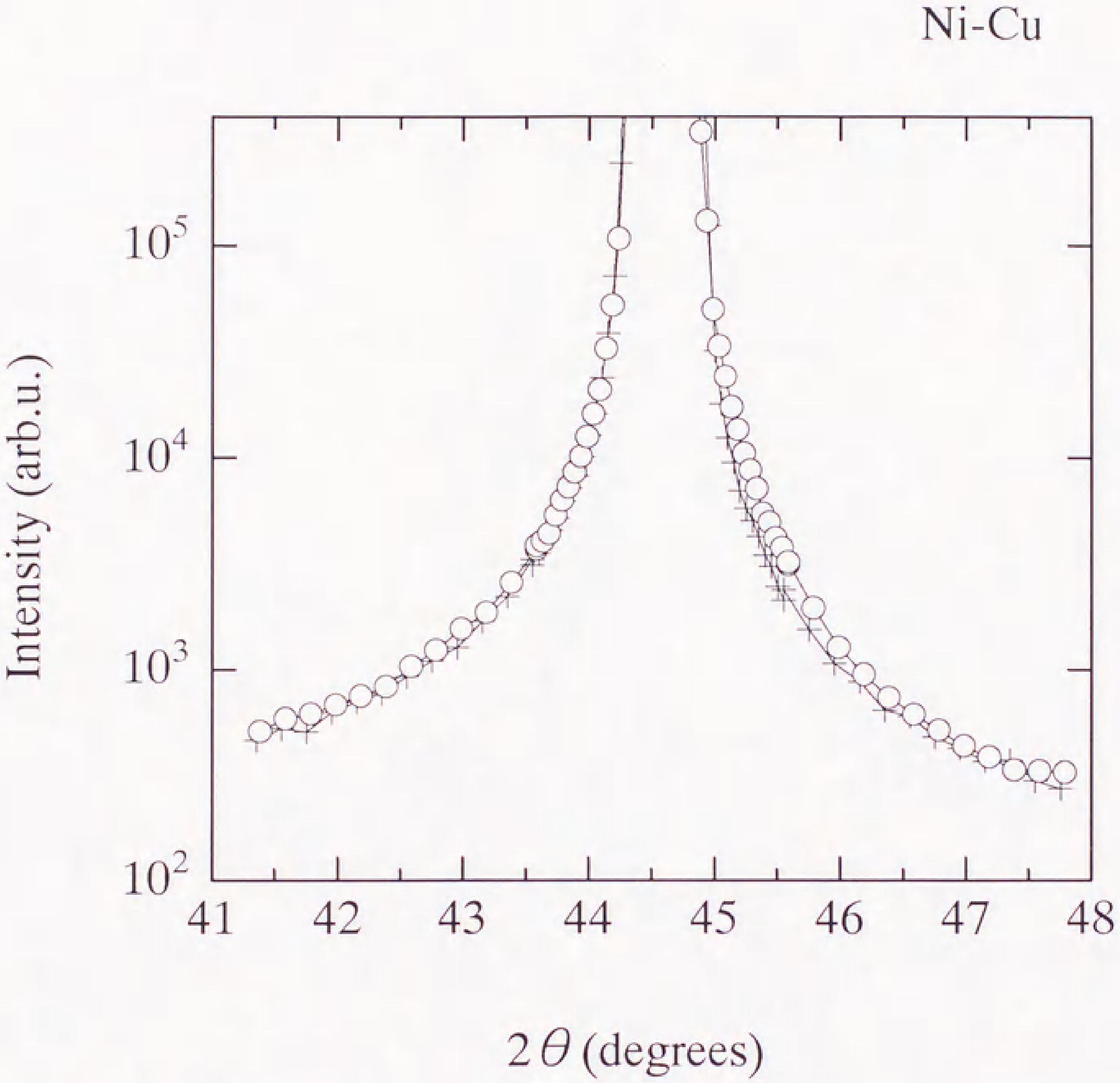

Fig.5-4 Intensity of X-ray scattering from Ni-Cu close to the (111) reflection in the [111] direction measured at room temperature.

○ : after irradiation (dose : 4.1×10^{14}ions/cm^2)
+ : before irradiation

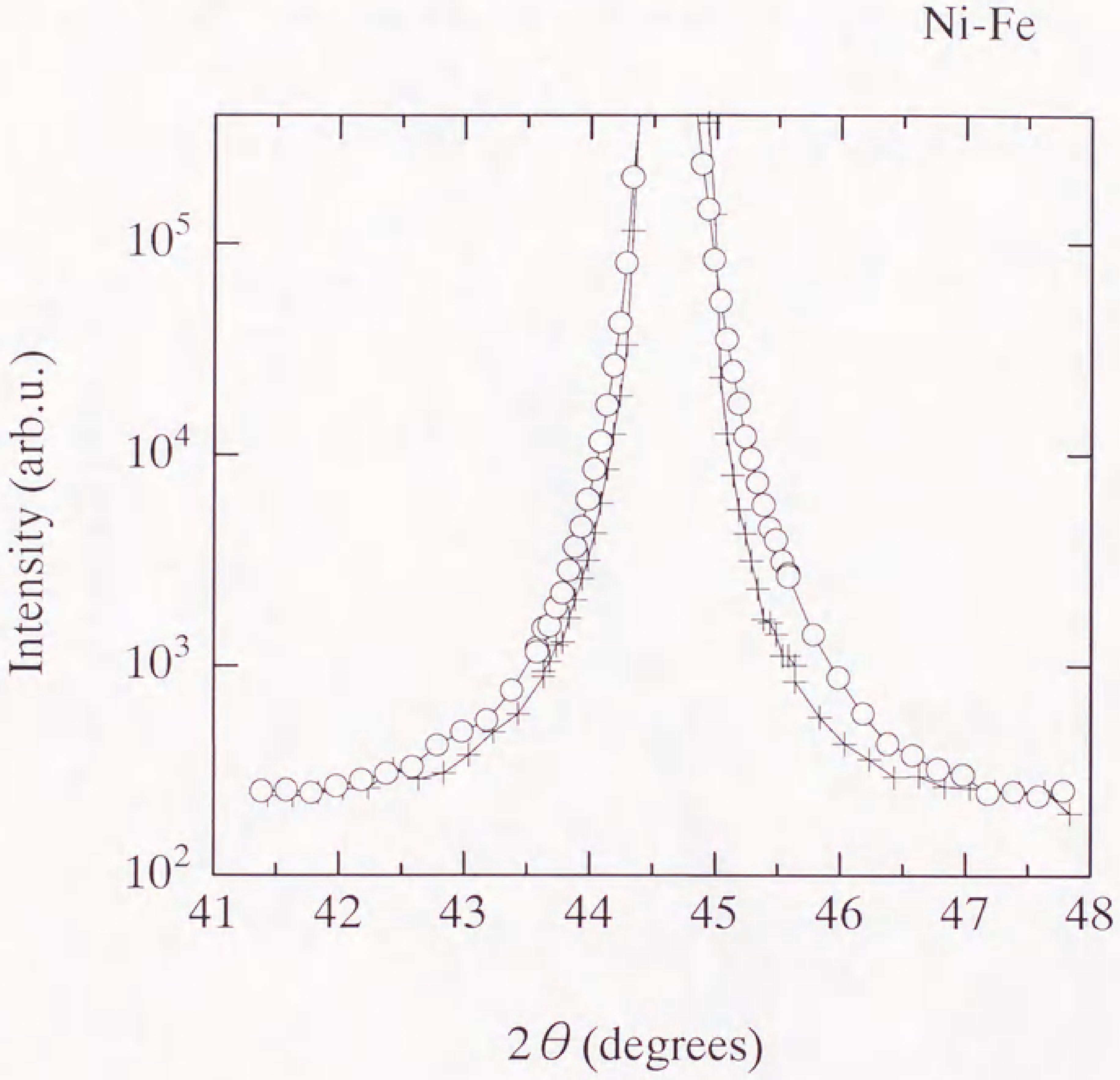

Fig.5-5 Intensity of X-ray scattering from Ni-Fe close to the (111) reflection in the [111] direction measured at room temperature.

○ : after irradiation (dose :4.1×10^{14}ions/cm^2)
+ : before irradiation

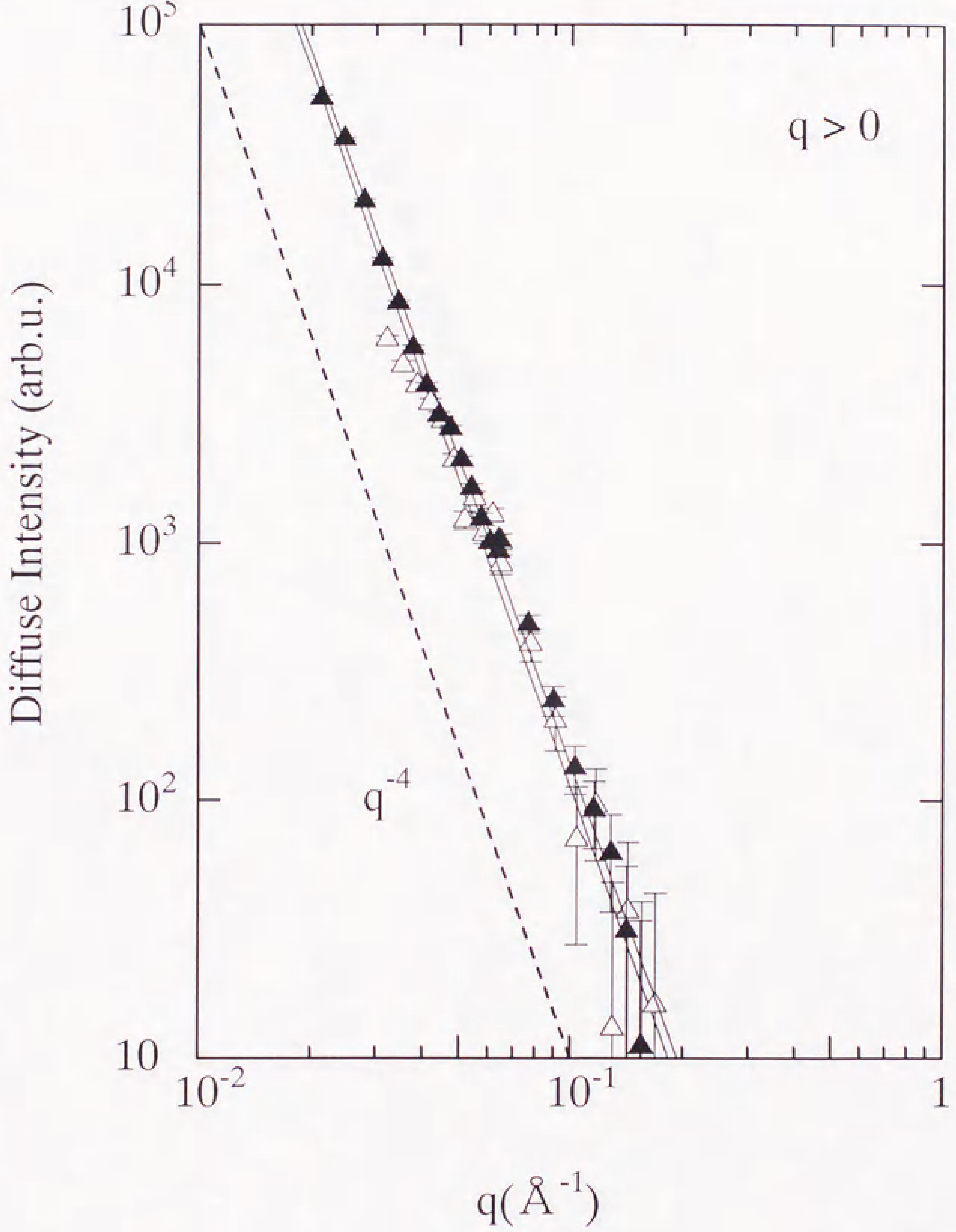

Fig.5-6 The q-dependence of diffuse scattering intensity in Ni-Cu alloy (q > 0)

△ : irradiation dose 1.6×10^{14} ions / cm^2
▲ : irradiation dose 4.1×10^{14} ions / cm^2

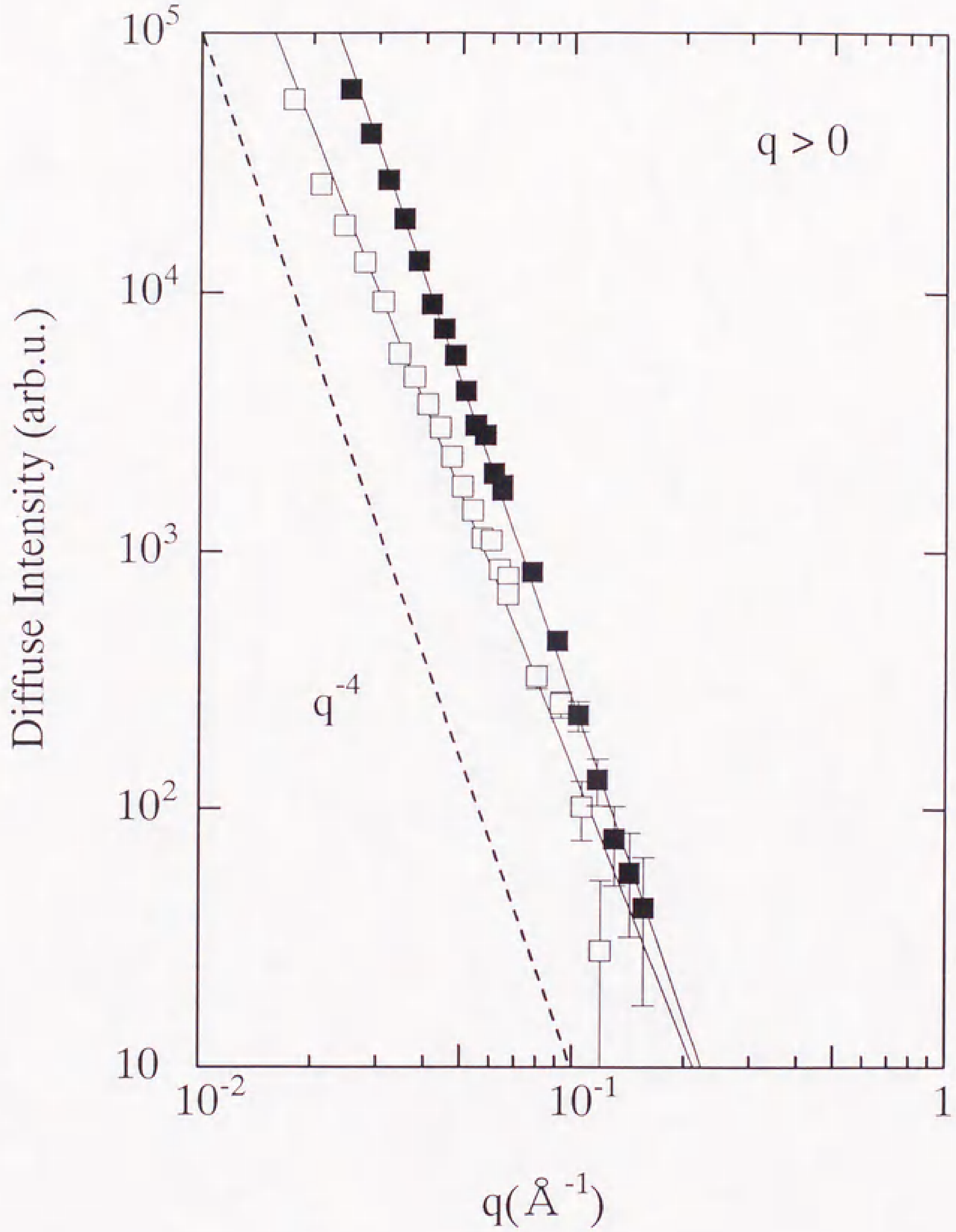

Fig.5-7 The q-dependence of diffuse scattering intensity in Ni-Fe alloy ($q > 0$)

☐ : irradiation dose 1.6×10^{14} ions / cm^2
■ : irradiation dose 4.1×10^{14} ions / cm^2

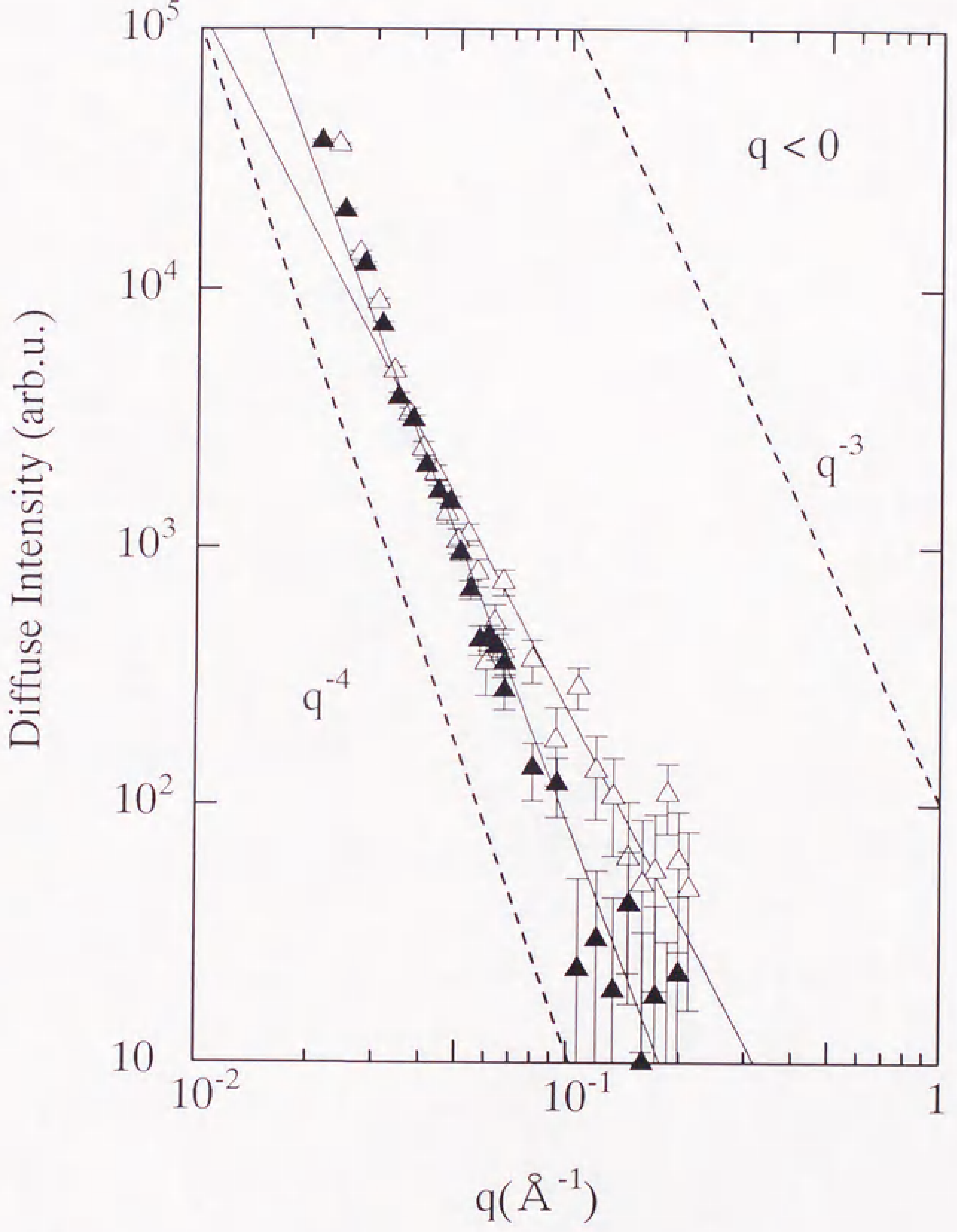

Fig.5-8 The q-dependence of diffuse scattering intensity in Ni-Cu alloy ($q < 0$)

△ : irradiation dose 1.6×10^{14} ions / cm^2
▲ : irradiation dose 4.1×10^{14} ions / cm^2

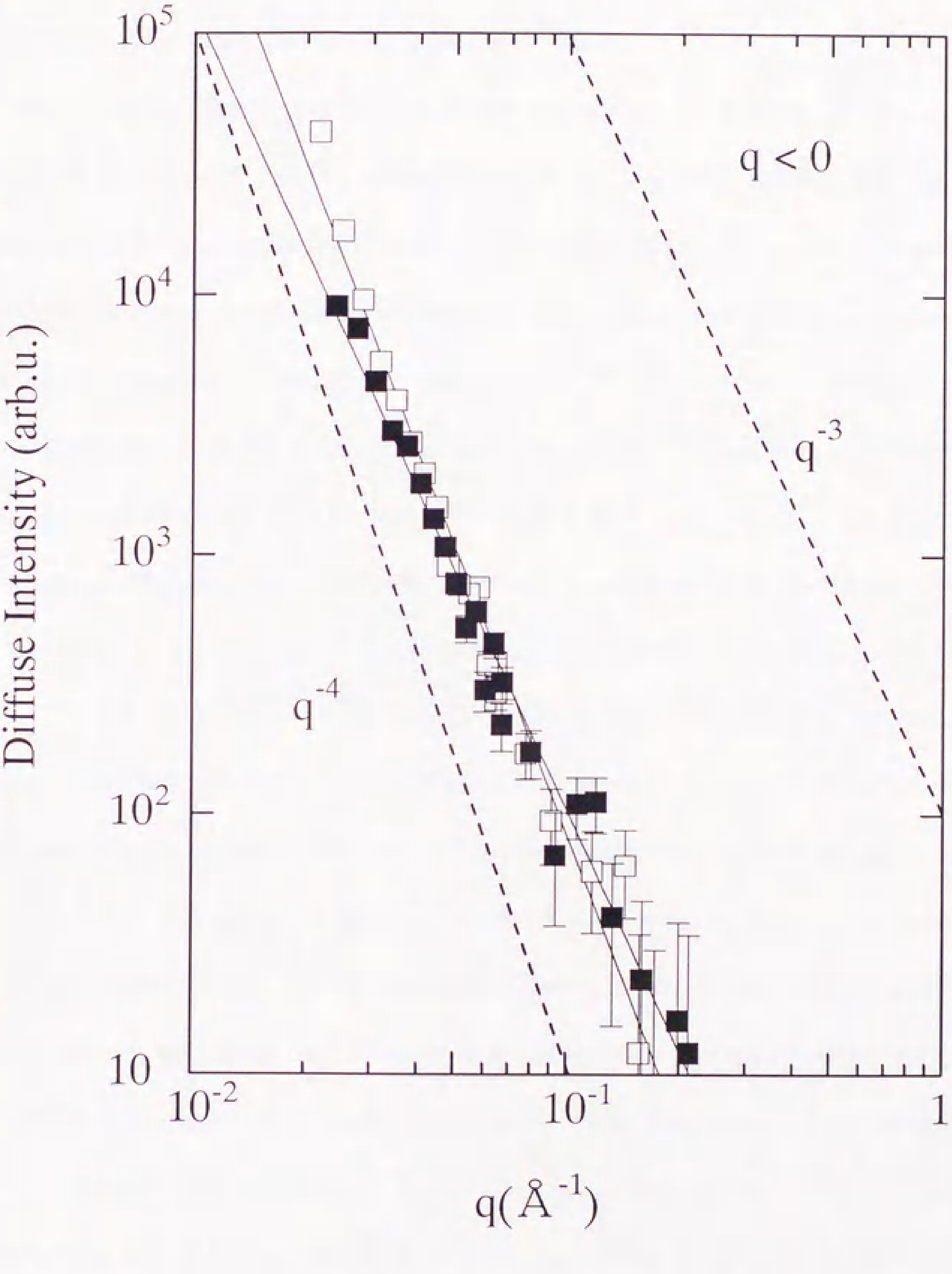

Fig.5-9 The q-dependence of diffuse scattering intensity in Ni-Fe alloy (q < 0)

□ : irradiation dose 1.6 × 10^{14} ions / cm^2
■ : irradiation dose 4.1 × 10^{14} ions / cm^2

irradiation doses with dilute alloys as a function of irradiation dose are shown in Figs.5-10 to 5-12. The asymmetry about $q = 0$ indicates the presence of the difference in loop size distribution between interstitial- and vacancy-loops.

More detailed information on the defect structures (i.e. number density and size distribution of loops) can be obtained by fitting the theoretically calculated q-dependence of diffuse scattering intensity to the experimental data. For this purpose, the q-dependencies of scattering amplitudes from vacancy and interstitial dislocation loops were calculated as a function of loop radius. The dilute alloys form single phase solid solution and have the same structure as Ni (*FCC*). Therefore, the theoretical calculation performed for pure Ni was used for this case. For the fit of the data in the present study, the theoretical diffuse scattering intensities from vacancy-loops and interstitial-loops were calculated as a function of loop radii of 5, 10, 20, 30, 40, 50 and 60Å. The size distribution of the dislocation loops can be obtained by assuming the coexistence of the several dislocation loops with different radii and fitting the calculated q-dependence to the experimental data. The results of the fitting, that are given by the dashed lines, are also shown in Figs.5-10 to 5-12 in comparison with the experimental data points. Tables 5-1 and 5-2 summarize the total number density of interstitial loops N_L^I and vacancy loops N_L^V, average loop radius $<R_L>$ and total number density of interstitial atoms N_I and vacancies N_V in the loops. The size distribution of the number density of loops for dilute Ni alloys, and also for pure Ni, is shown in Figs.5-13 and 5-14. The size distribution of vacancy loops is also relatively narrow for dilute alloys compared with that of interstitial loops, which is thought to be due to the small mobility of vacancies compared with interstitials.

The size distributions for the number of interstitials or vacancies contained in

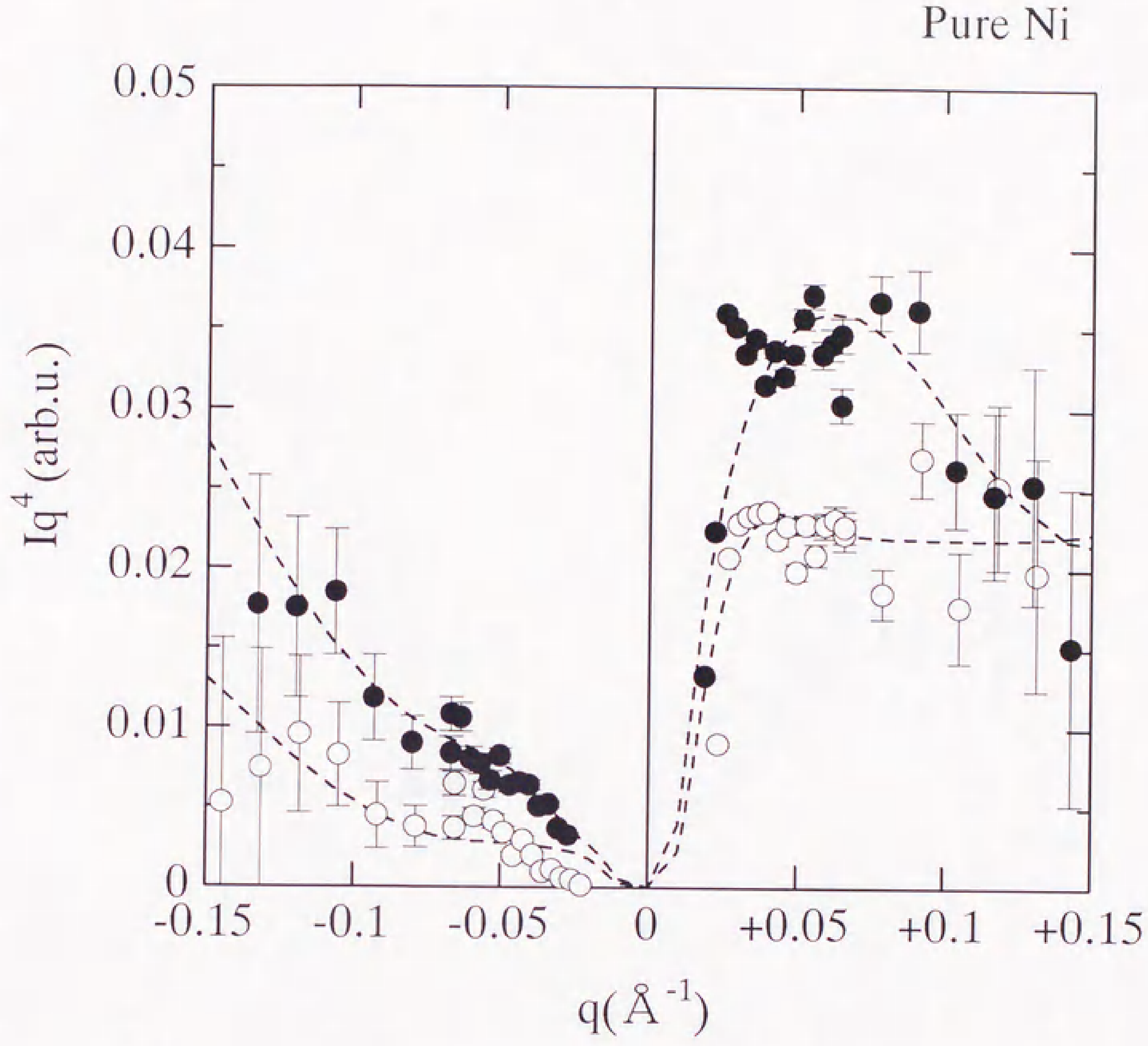

Fig.5-10 Diffuse scattering intensity scaled by q^4 obtained from pure Ni with dashed line fitted to the data.

○ : 1.6×10^{14} ions / cm^2
● : 4.1×10^{14} ions / cm^2
---- : fitted curve

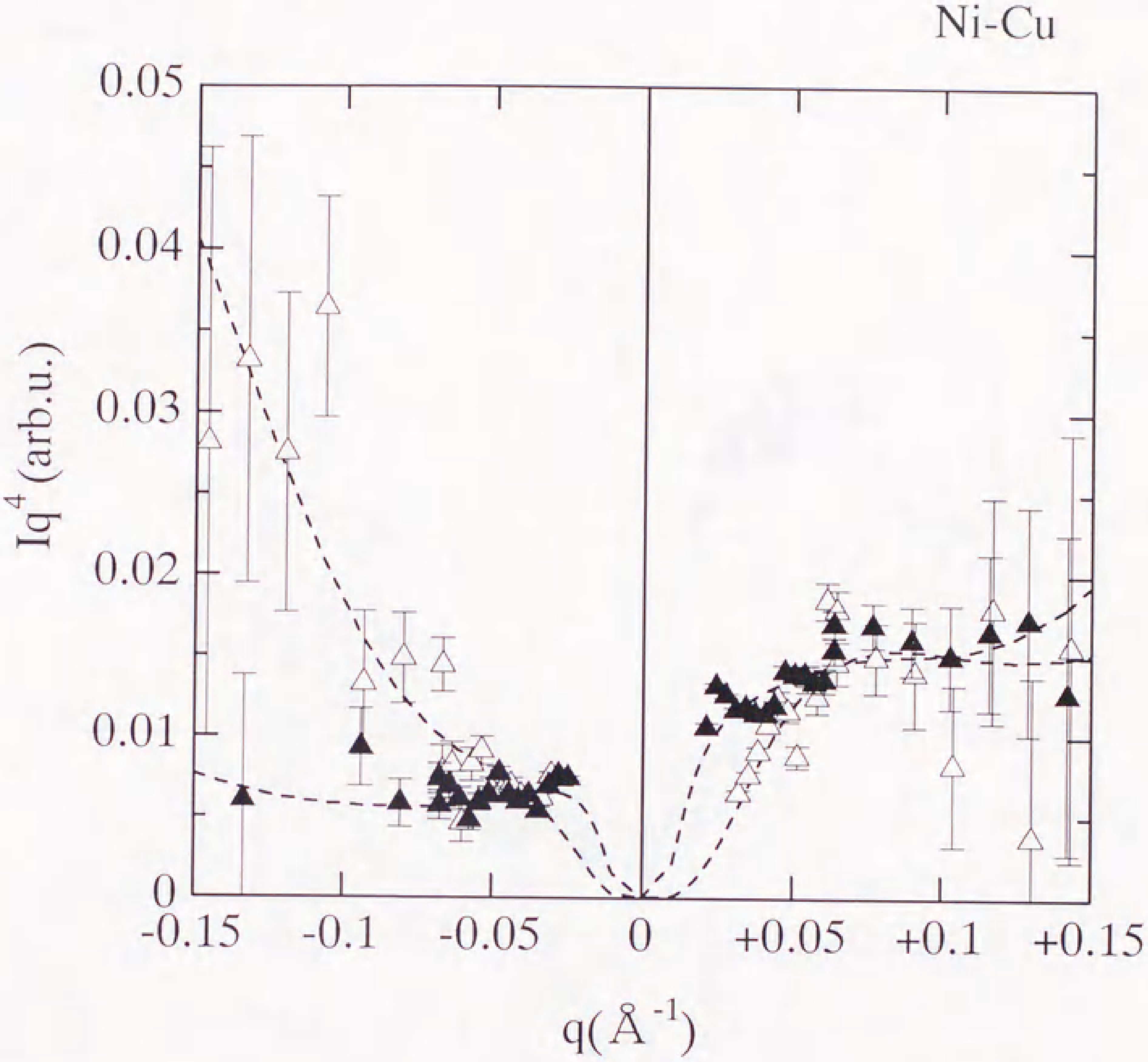

Fig.5-11 Diffuse scattering intensity scaled by q^4 obtained from Ni-Cu with dashed line fitted to the data.

△ : 1.6×10^{14} ions / cm^2
▲ : 4.1×10^{14} ions / cm^2
---- : fitted curve

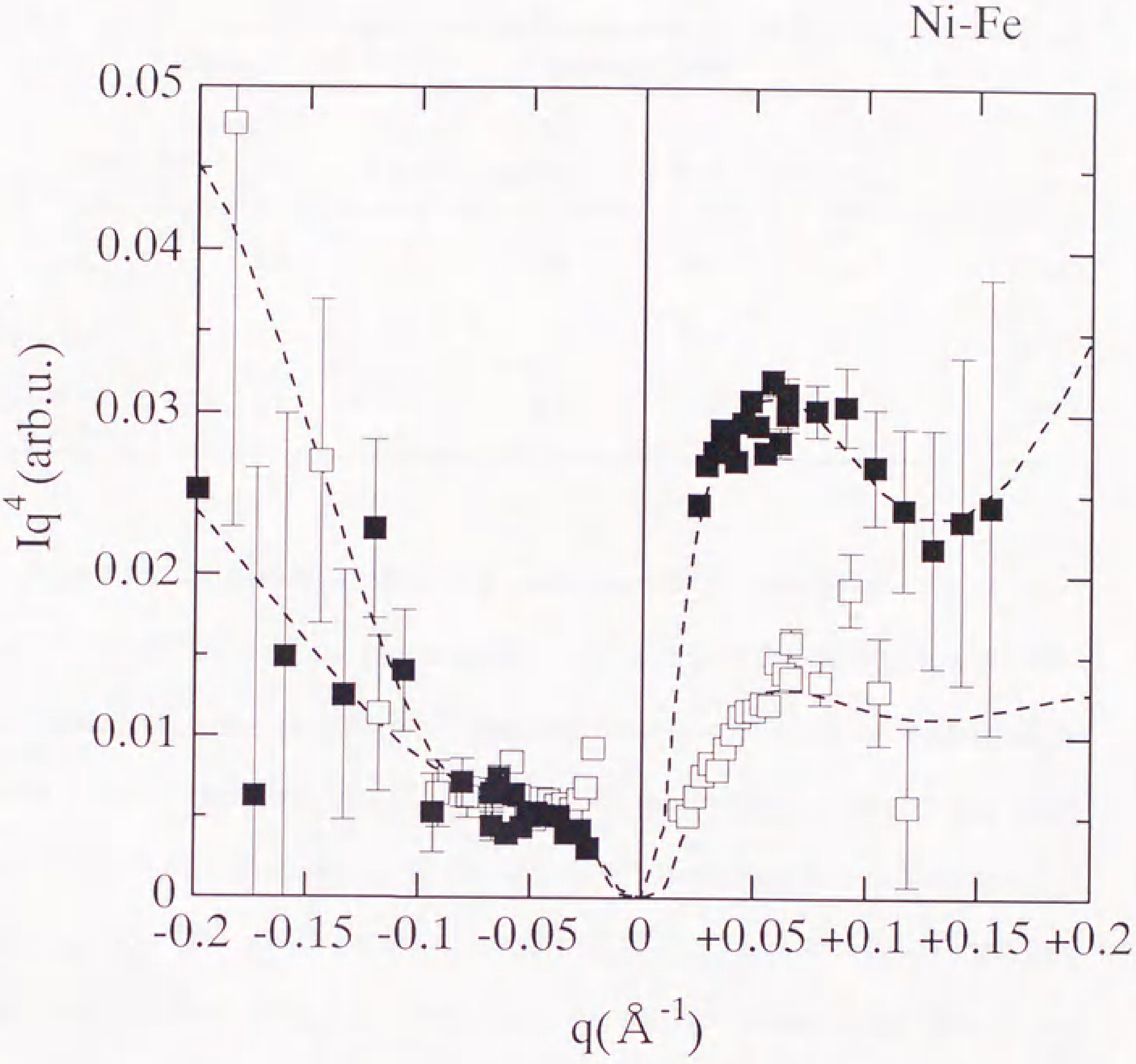

Fig.5-12 Diffuse scattering intensity scaled by q^4 obtained from Ni-Fe with dashed line fitted to the data.

□ : 1.6×10^{14} ions / cm^2
■ : 4.1×10^{14} ions / cm^2
---- : fitted curve

Table 5-1 The summary of the results for the irradiation dose of 1.6 × 10^{14}ions/cm^2

	Vacancies			*Interstitial atoms*			
	N_V ($10^{18}cm^{-3}$)	$<R_L^V>$ (Å)	N_L^V ($10^{17}cm^{-3}$)	N_I ($10^{18}cm^{-3}$)	$<R_L^I>$ (Å)	N_L^I ($10^{17}cm^{-3}$)	N_I/N_V
Ni	0.2	5.0	0.1	0.4	7.5	0.07	67/33
Ni-Cu	0.6	5.1	0.4	0.1	13.9	<0.01	14/86
Ni-Fe	0.5	5.0	0.3	0.1	15.4	<0.01	17/83

loops with size R obtained from the fitting to the data for the irradiation dose of 1.6 × 10^{14} and 4.1 × 10^{14} ions/cm^2 are shown in Figs.5-15 and 5-16 for Ni, Ni-Cu and Ni-Fe alloys, respectively. For pure Ni, it is seen that the number density of interstitials or vacancies in loops increases with the increment of the irradiation dose. The small number densities of interstitials in Ni-Cu and Ni-Fe alloys compared with pure Ni is seen in Fig.5-15. The small interstitial loops ($\leqq$10Å) become to be formed with the increment of dose (Fig.5-16) and the mean radius become small due to this formation of small loops (Tables 5-1 and 5-2). From these figures, it is concluded that the formation of interstitial loops in Ni-Cu and Ni-Fe alloys is suppressed compared with pure Ni. This smaller average radius of interstitial loops in Ni-Cu and Ni-Fe alloys than pure Ni is seen in Table 5-2, indicating the presence of the stronger binding force between solute atoms and interstitials. The previous results of DXS [10-13] revealed that Si (under-sized), Ge, Fe and Cu (over-sized) solute in Ni interacted strongly with interstitials. The solute atoms in Ni could also be considered to trap the interstitials and suppress the formation of interstitial loops. The effects of solute atoms on the growth of interstitial-loops showing the same trend in dilute Ni-Cu and Ni-Fe

Table 5-2 The summary of the results for the irradiation dose of 4.1 × 10^{14}ions/cm^2

	Vacancies			*Interstitial atoms*			
	N_V ($10^{18}cm^{-3}$)	$<R_L{}^V>$ (Å)	$N_L{}^V$ ($10^{17}cm^{-3}$)	N_I ($10^{18}cm^{-3}$)	$<R_L{}^I>$ (Å)	$N_L{}^I$ ($10^{17}cm^{-3}$)	N_I/N_V
Ni	0.4	5.1	0.3	0.4	9.7	0.04	50/50
Ni-Cu	0.1	6.5	0.02	0.3	5.8	0.1	75/25
Ni-Fe	0.2	5.3	0.1	0.5	6.7	0.1	71/29

alloys can be explained from the fact that the volume size factors of both Cu (+7.18%) and Fe (+10.57%) are positive in Ni.

It is generally assumed that the defect distribution consists of a vacancy rich core surrounded by a shell of interstitials. Furthermore, it is assumed that interstitials are much mobile than vacancies so that interstitials migrate away rapidly and escape from the recombination with vacancies. If the mobility of interstitials is reduced by solute atoms, these kinetic process may be altered and the solute atoms prevent interstitials from clustering into large loops due to enhanced recombination between interstitials and vacancies [12]. In addition, if the radiation annealing extends to stage I_D or I_E interstitials that should be trapped by solute atoms, these interstitials escape from solute atoms and reduce the number density of vacancy loops through the recombination with vacancy loops. This model may explain the smaller number densities of vacancies in both Ni-Cu and Ni-Fe alloys compared with pure Ni for the irradiation dose of 4.1 × 10^{14} ions/cm^2 where the extensive radiation annealing occurred, as discussed in the previous chapter.

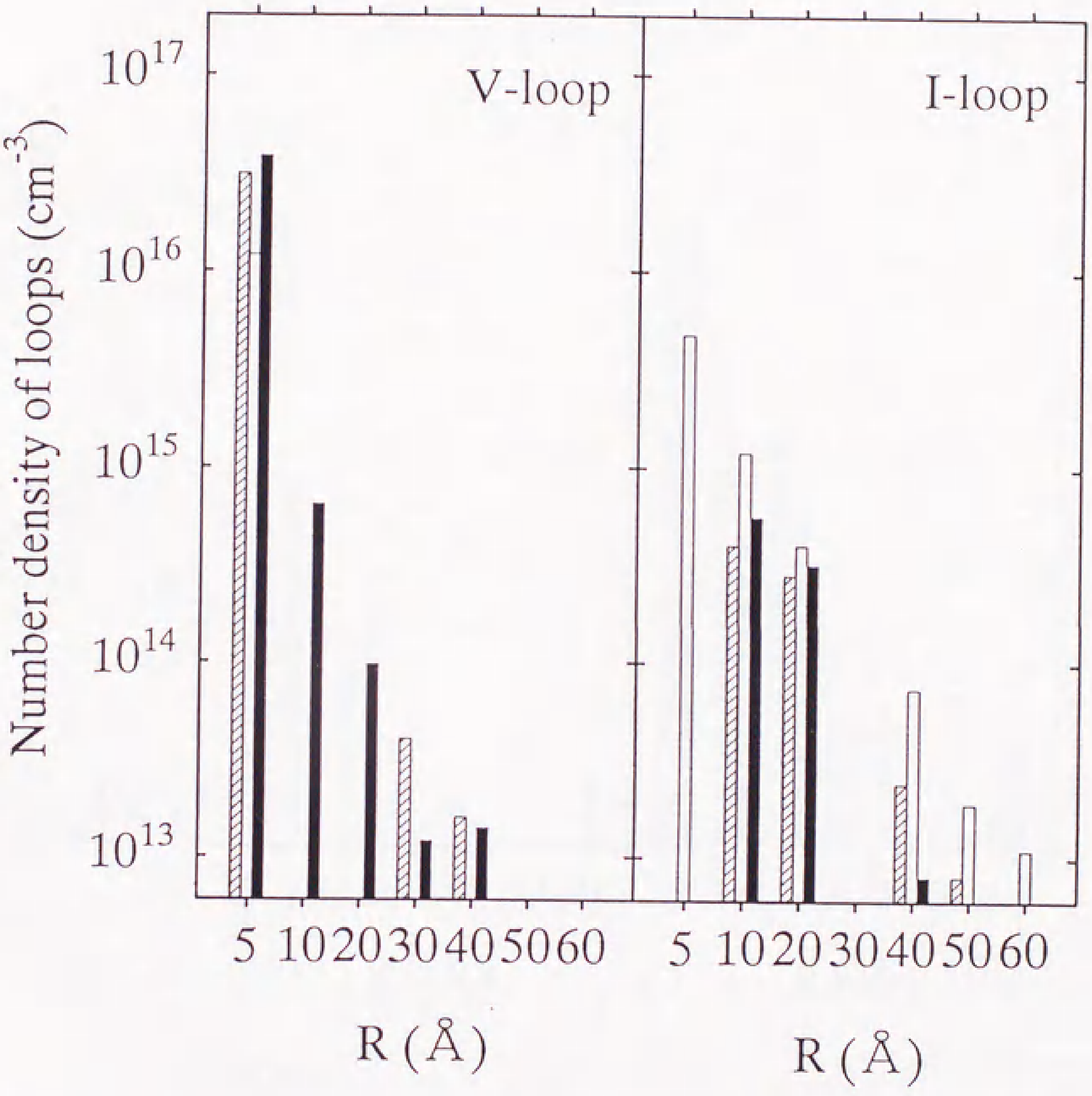

Fig.5-13 Distribution of the number density of loops with radius R for the irradiation dose of 1.6×10^{14} ions / cm^2.

□ Ni
▨ Ni-Fe
■ Ni-Cu

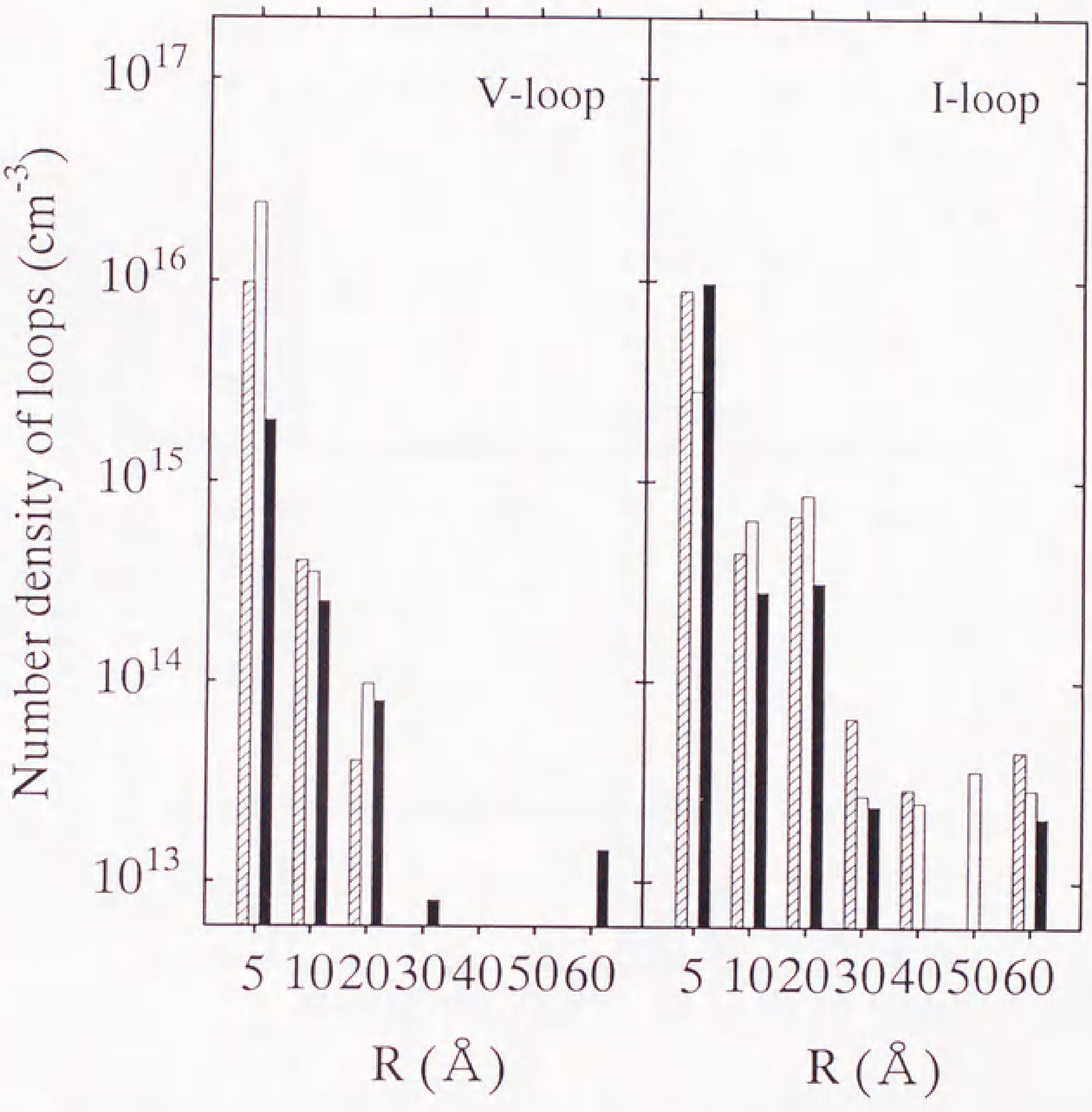

Fig.5-14 Distribution of the number density of loops with radius R for the irradiation dose of 4.1×10^{14} ions / cm^2.

□ Ni
▨ Ni-Fe
■ Ni-Cu

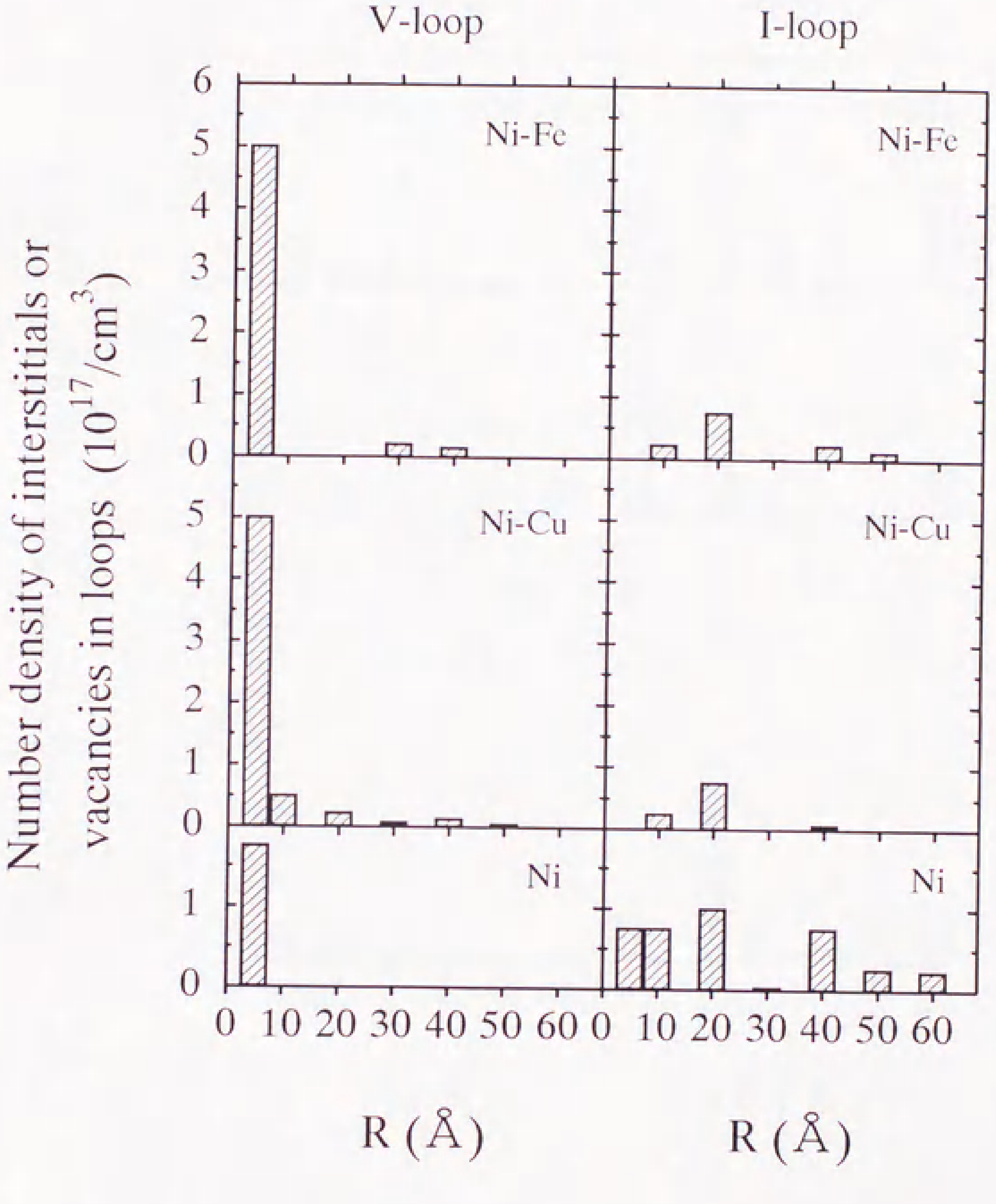

Fig.5-15 The size distribution og interstitials or vacancies in loop with a radius R for the irradiation dose of 1.4 × 10^{14} ions/cm^2

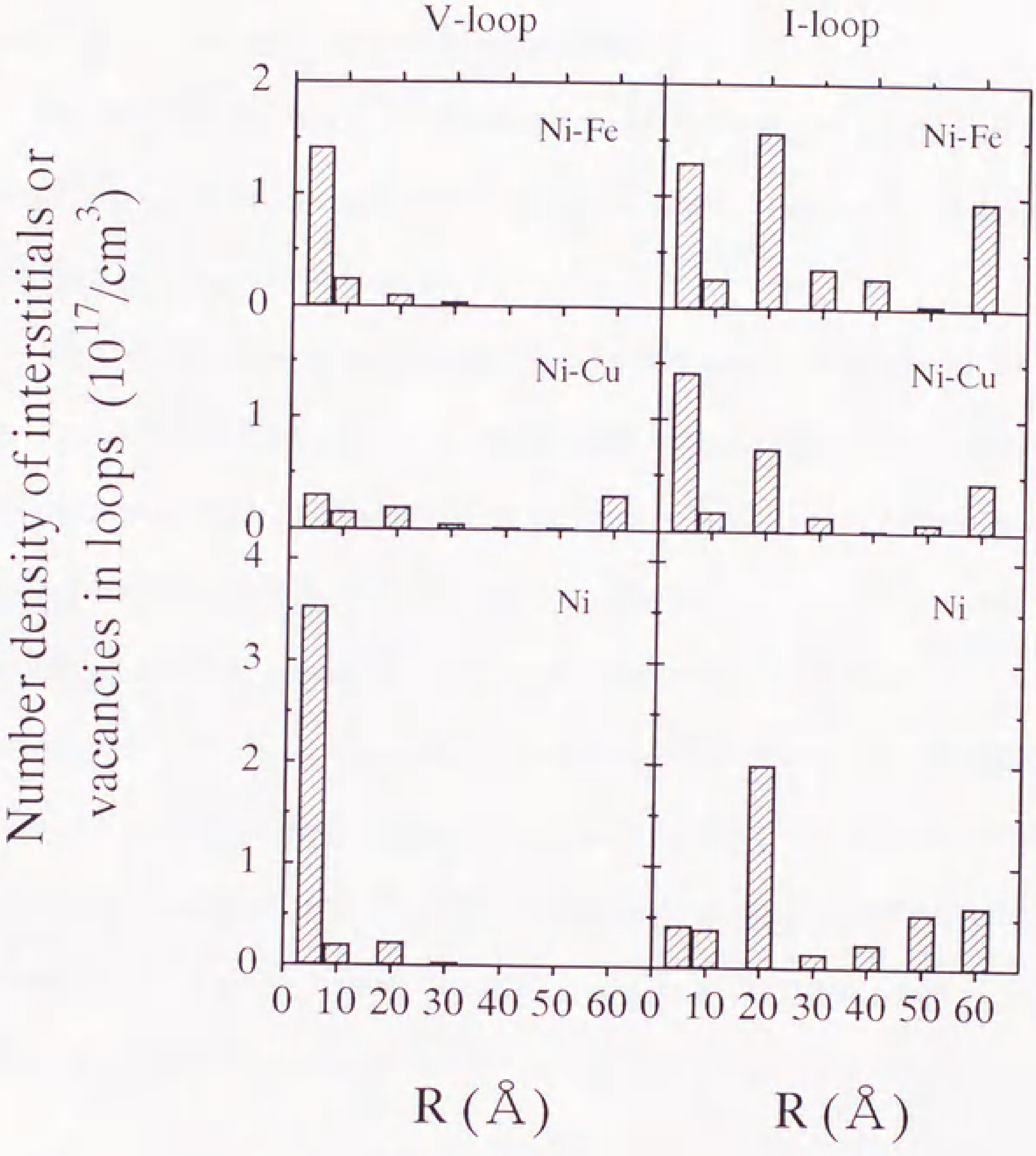

Fig.5-16 The size distribution og interstitials or vacancies in loop with a radius R for the irradiation dose of 4.1 × 10^{14} ions/cm^2

5.4 Conclusions

The defect structures of pure Ni and dilute Ni-Cu and Ni-Fe alloys irradiated with 150MeV phosphorus ions at about 30 K were studied by diffuse X-ray scattering (DXS), and the following results were obtained.

(1) For pure Ni, it was seen that the number density of interstitials or vacancies in loops formed in the surface region of the specimen less than 5μm increases with the increment of the irradiation dose.

(2) The formation of interstitial loops in Ni-Cu and Ni-Fe alloys for the irradiation dose of 1.6×10^{14} ions/cm^2 was suppressed compared with pure Ni, indicating the presence of the stronger binding force between solute atoms and interstitials.

(3) The number density of vacancy-loops in dilute Ni-Cu and Ni-Fe alloys decreased with the increment of the irradiation dose. This result may be explained by the kinetics that the radiation annealing extend to interstitials should be trapped by solute atoms. This result could be explained from the fact that the enhanced radiation annealing occurred in pure Ni. That is, the dose dependence of the number density of interstitials in pure Ni became negligibly small for the same range of irradiation dose (1.6×10^{14} ～ 4.1×10^{14} ions/cm^2).

References

[1] M. A. Kirk, I. M. Robertson, M. L. Jenkins, C. A. English, T. J. Black and J. S. Vetrano, *J. Nucl. Mater.* **149**(1987)21.

[2] C. A. English and M. L. Jenkins, *Material Science Forum* **15**(1987)1003.

[3] I. M. Robertson, J. S. Vetrano, M. A. Kirk and M. J. Jenkins, *Phil. Mag.* A**63**(1991)299.

[4] J. S. Vetrano, I. M. Robertson and M. A. Kirk, *J. Nucl. Mater.*, **205**(1993)68.

[5] J. S. Vetrano, I. M. Robertson and M. A. Kirk, *Phil. Mag.* **68**(1993)381.

[6] I. M. Robertson and M. J. Jenkins, *Phil. Mag.* A**43**(1981)999.

[7] R. S. Averback, T. Diaz de la Rubia and R. Benedek, *Nucl. Instr. and Meth.*, B**33**(1988)693.

[8] T. Diaz de la Rubia, R. S. Averback, R. Benedek and W. E. King, *Phys. Rev. Lett.* **59**(1987)579.

[9] T. Diaz de la Rubia, R. S. Averback, H. Hsieh and R. Benedek, *J. Mater. Res.* **4**(1989)579.

[10] P. Ehrhart and R. S. Averback, *J. Phys. F : Met. Phys.* **14**(1984)1365.

[11] R. S. Averback and P. Ehrhart, *J. Phys. F : Met. Phys.* **14**(1984)1347.

[12] P. Ehrhart and R. S. Averback, *Phil. Mag.* **A60**(1989)283.

[13] O. Bender and P. Ehrhart, *Point Defects and Defect Interactions in Metals* (1982)639.

6. Conclusions

In this thesis the defect structure in pure Ni and dilute Ni alloys irradiated with high-energy ions were investigated by Diffuse X-ray Scattering (DXS) methods to consider the effect of the radiation annealing phenomena on the resulting defect structure. For this purpose, the high-energy ion-irradiation experiments and the DXS experiments with use of a synchrotron radiation source were performed. To analyze the defect structure from obtained diffuse-scattering intensity distributions, the theoretical diffuse scattering amplitudes was calculated by a unique method.

In chapter 3, the improved unique calculation method to obtain the theoretical diffuse-scattering and the examples of the calculation results were shown. In this study, the theoretical calculation was performed directly from the basic equations without replacing the lattice sum with some approximated equations by the aid of the recent high-performance computer. The size distributions of loops became to be obtained by this calculations.

In chapter 4, the defect structures in pure Ni irradiated high-energy phosphorus- and iodine-ions were investigated. The dose dependence of the number density of interstitials in loops on dose for the case of 150MeV P-ion irradiation became negligible small around 10^{14} ions/cm^2. This result was explained by the presence of the radiation annihilation on interstitials under irradiation. The ratio of interstitials annihilated in cascades to the calculated number of created interstitials for P- and I-ion irradiation was large (about 93 - 97%) compared with that for neutron irradiation (33 - 50%). The damage efficiencies of both P- and I-ion irradiations were about 1/5 ～ 1/10 of that for low-energy ion-irradiations. The annihilation cross-sections for each interstitial types in Ni under 150MeV P-ion irradiation were obtained using the data for 85MeV I-ions irradiation. The radiation annealing cross-sections obtained were σ_1^P of 2.0×10^{-13}cm^2 (stage I_{B+C} interstitials), σ_2^P of 1.5×10^{-14}cm^2 (stage I_{D+E}) and σ_3^P of 3.4×10^{-15}cm^2 (stage II interstitials).

In chapter 5, the DXS experiments for dilute Ni-Cu and dilute Ni-Fe alloys irradiated with high-energy phosphorus-ions were performed to make clear the effect of motion of the interstitials on radiation annealing through the interstitials-solute interactions. The formation of interstitial-loops in dilute alloys was suppressed compared with pure Ni, indicating the presence of the stronger binding force between solute atoms and interstitials for a irradiation dose of 1.4×10^{14} ions/cm^2. However, the number density of vacancy-loops in dilute Ni-Cu and Ni-Fe alloys decreased with the increment of the irradiation dose. This result may be explained by the kinetics that the radiation annealing extend to interstitials should be trapped by solute atoms. The experimental results for pure Ni (chapter 4) support this model. That is, the dose dependence of the number density of interstitials in interstitial loops in pure Ni became negligibly small for the irradiation dose of 1.6×10^{14} ～ 4.1×10^{14} ions/cm^2.

Consequently, the enhanced radiation annealing phenomena found in electrical resistivity measurements was concluded to extend to free interstitial contributing to the formation of interstitial loop.

Acknowledgment

The present thesis is the collection of studies which have been carried out under the direction of Prof. Tsuneo MATSUI of Department of Quantum Engineering, Graduate School of Engineering, Nagoya University. The author expresses grateful acknowledgment to Prof. Tsuneo MATSUI, Assoc. Prof. Takanori NAGASAKI, Dr. Hirotake SHIGEMATSU and Dr. Yuji ARITA for their valuable suggestion, discussion and continuous encouragement throughout this work.

The thesis was completed through the discussions and suggestions by Prof. Tsuneo MATSUI, Prof. Hiroyasu SAKA and Assoc. Prof. Takanori NAGASAKI. I would like to express my thanks to them.

The author is deeply indebted to Dr. Hiroshi MAETA, Dr. Kiichi HOJOU, Dr. Akihiro IWASE, Dr. Hideo OHTSUKA and Dr. Hiroyuki SUGAI of Department of Materials Science and Engineering, Japan Atomic Energy Research Institute (JAERI) for the kind support for irradiation experiments at JAERI Tokai and at JAERI Takasaki and Prof. Katsumi KOBAYASHI of Photon Factory, Institute of Materials Structure Science, High Energy Accelerator Research Organization at Tsukuba for the kind support for DXS experiments.

Grateful acknowledgement is made to the operating members of JAERI Tokai and JAERI Takasaki.

Finally the author express his gratitude heartily to his wife, Mrs. Miwa YUYA.

Jan, 1999

Hideki Yuya

List of published papers

(1) Hideki Yuya, Hiroshi Maeta, Hideo Ohtsuka, Norimasa Matsumoto, Hiroyuki Sugai, Akihiro Iwase, Tsuneo Matsui, Tetsuya Suzuki, Morio Jinchoh and Kohji Yamakawa.: "Diffuse X-ray scattering studies of radiation defects in Ni and dilute Ni alloys", *J. Nucl. Mater.* **271&272**(1999) in print

(2) Hideki Yuya, Tsuneo Matsui, Hiroshi Maeta, Hideo Ohtsuka and Hiroyuki Sugai,: "Defect clusters in high-energy ion-irradiated Ni and dilute Ni alloys investigated by diffuse X-ray scattering", *Nucl. Inst. and Meth. in Physics Research. B* **148**(1999) 891-895.

(3) Hideki Yuya, Tsuneo Matsui, Hirotake Shigematsu, Hiroshi Maeta, Hideo Ohtsuka, Hiroyuki Sugai and Akihiro Iwase,:
"Diffuse X-ray scattering studies on defect clusters in Ni irradiated by high-energy ions and electrons", *Jpn. J. Appl. Phys.* **38**(1999) in print

(4) Hideki Yuya, Tsuneo Matsui, Hirotake Shigematsu, Hideo Ohtsuka, Hiroyuki Sugai and Akihiro Iwase,:
"Effect of high-energy ion-irradiation on defect formation in pure Ni and dilute Ni alloys", *J. Phys.: Condens. Matter* (1998) submitted

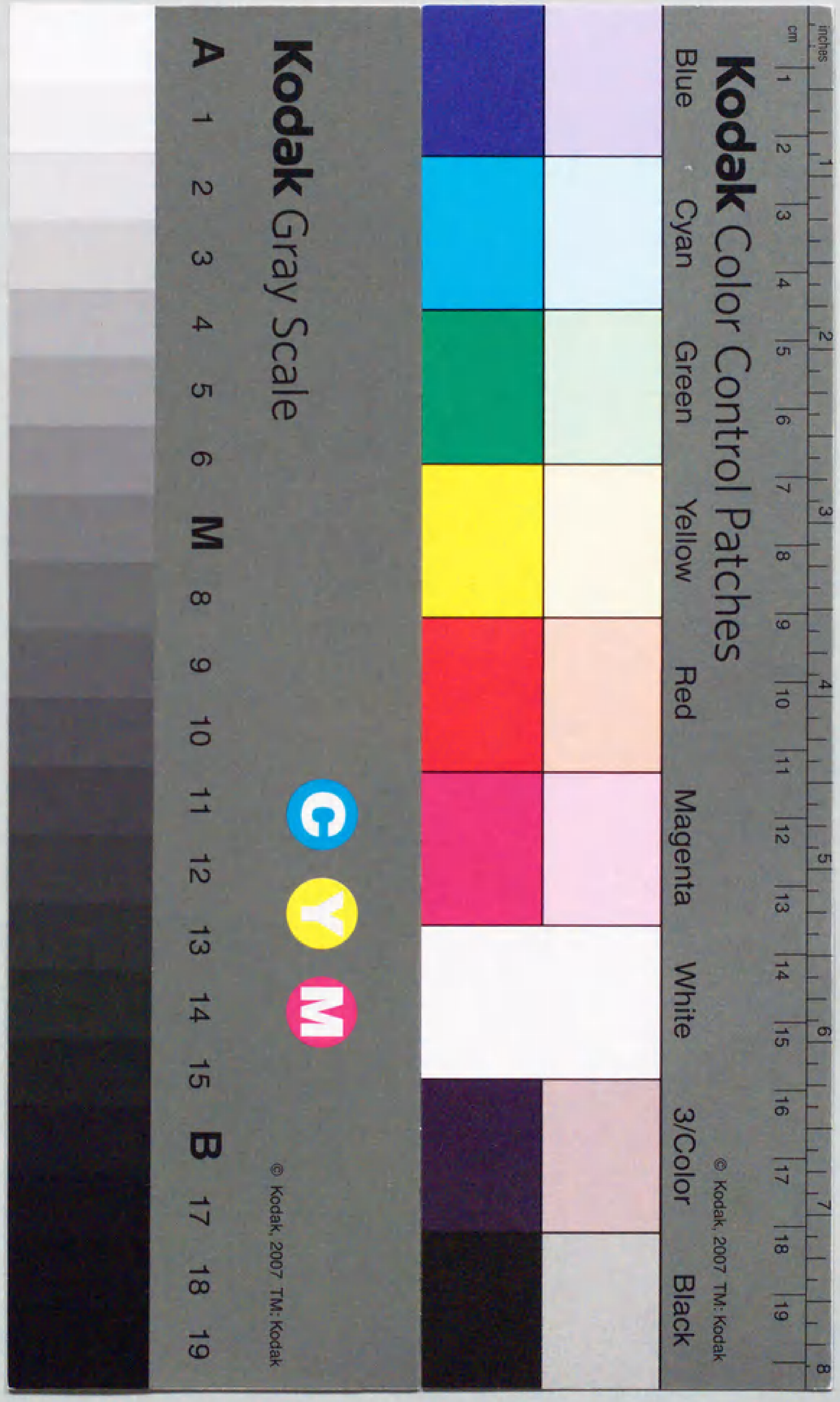

inches
cm
Kodak Color Control Patches
Blue
Cyan
Green
Yellow
Red
Magenta
White
3/Color
Black
© Kodak, 2007 TM: Kodak
Kodak Gray Scale
A
1
2
3
4
5
6
M
8
9
10
11
12
13
14
15
B
17
18
19
C
Y
M
© Kodak, 2007 TM: Kodak